Dissertation
submitted to the
Combined Faculties for the Natural Sciences and for Mathematics
of the Ruperto-Carola University of Heidelberg, Germany
for the degree of
Doctor of Natural Sciences

presented by
Christine Selhuber, M. Sc.
born in Landshut

Oral examination: December 4th, 2006

Biological Adhesion on Nanopatterned Substrates Studied with Force Spectroscopy and Microinterferometry

Referees:
Prof. Dr. Joachim Spatz
Prof. Dr. Heinz Horner

Untersuchung biologischer Adhäsionsprozesse auf nanostrukturierten Substraten mittels Kraftspektroskopie und Mikro-Interferometrie

Für ein physikalisches Verständnis von Adhäsionsprozessen sind Oberflächenstrukturen mit definierten Adhäsionseigenschaften vonnöten. In dieser Arbeit wurden biofunktionalisierte Nanostrukturen verwendet, welche eine quasi-hexagonale Anordnung von Molekülen ermöglichen. Die Oberflächenenergie einer solchen Anordnung von Streptavidinmolekülen wurde interferometrisch analysiert. Desweiteren wurden Nanostrukturen verwendet, um die integrinvermittelte Adhäsion von Zellen zu untersuchen. Diese Art der Adhäsion stellt einen hochkomplexen biologischen Prozess dar und ist essenziell für zahlreiche Zellfunktionen. Mit Hilfe von Nanostrukturen lässt sich der Abstand einzelner Integrinbindungsstellen präzise definieren. In Zellkulturexperimenten zeigte sich, dass dieser Abstand die Zelladhäsion nachhaltig beeinflusst, insbesondere die Bildung von Adhäsionsclustern, den sogenannten Fokalkontakten. Um die Adhäsionsclusterbildung bei verschiedenen Abständen von Integrinbindungsstellen zu erfassen, wurde im Rahmen dieser Arbeit die Zelladhäsion kraftspektroskopisch mit Hilfe einer magnetischen Pinzette und eines Rasterkraftmikroskops (AFM) für verschiedene Adhäsionszeiträume untersucht. Die Experimente zeigten, dass ein Abstand der Integrinbindungsstellen von 70 nm und mehr die kooperative Ausbildung von Adhäsionsclustern bereits in Kurzzeitadhäsionsprozessen erheblich einschränkt. In Langzeitadhäsionsstudien nach mehrstündiger Zelladhäsion stellte sich heraus, dass die Fokalkontaktbildung zu einer kooperativen Verstärkung der lokalen Adhäsionsstärke führt. Die gewonnen Resultate wurden mit theoretischen Modellen in Beziehung gesetzt und leisten einen wesentlichen Beitrag zum physikalischen Verständnis der Zelladhäsion.

Biological Adhesion on Nanopatterned Substrates Studied with Force Spectroscopy and Microinterferometry

For a physical understanding of adhesion, surfaces of defined adhesion properties are required. In this work, biofunctional nanopatterns were employed, which allow molecules to be positioned in a quasi-hexagonal lattice. For such an arrangement of streptavidin molecules the surface energy was analysed microinterferometrically. Furthermore, nanopatterns were used to investigate integrin-mediated cell adhesion, which is a highly complex biological process and essential for numerous cell functions. With nanopatterns the distance between adjacent single integrin binding sites is precisely defined. Recent cell culture experiments have revealed that this distance strongly affects cell adhesion, especially the formation of adhesion clusters, known as focal contacts. To quantify the adhesion cluster formation for different integrin binding site spacings, cell adhesion was studied at different timescales using magnetic tweezers and atomic force microscopy (AFM). The experiments demonstrated that an integrin binding site spacing of 70 nm and more prevents the cooperative formation of early adhesion clusters in initial adhesion. In long-term adhesion studies, after several hours of cell adhesion, it turned out that focal contact formation cooperatively increases the local adhesion strength. The obtained results could be related to theoretical models and make an important contribution to the physical understanding of cell adhesion.

Contents

Introduction and Objective

Many phenomena of the intra- and extracellular organisation of an organism are regulated by cell adhesion. Cell adhesion is, for example, an important prerequisite for many cell activities such as cell motility, differentiation and apoptosis (Blau and Baltimore, 1991). In cells of the connective tissue, hierarchically, regularly organised adhesion structures have been identified, the so-called focal contacts. Focal contacts consist of a large variety of different proteins. The interaction between the proteins inside the focal contact is essential for its adhesive and mechanosensory function (Zamir and Geiger, 2001a; Zamir and Geiger, 2001b). Due to the complex internal structure of a focal contact it would be a logical consequence that the whole adhesion structure can be destroyed by changing the configuration of parts of the adhesion contact. One focal contact component which is easily influenced from the cellular outside is the integrin, a transmembrane protein which is responsible for the linkage between the cell interior and the surrounding matrix. By employing functionalised nanopatterned substrates, it is possible to provide a pattern of adhesion ligands on substrates with nanometre precision. These substrates also allow to define the position of integrin binding sites. As a consequence, the pattern of integrins in the cell membrane corresponds to the pattern of its binding sites on the substrate. Recent studies using this approach have shown, that a variation of the distance of integrin binding sites indeed strongly affects the formation of focal contacts and even influences the fate of the whole cell (Arnold et al., 2004; Cavalcanti-Adam et al., 2006). So far, the detailed biological mechanisms that regulate this process are still unknown. However, the results indicate that focal contact formation requires a certain supermolecular arrangement of integrin binding sites. This arrangement must be fulfilled to induce the biological function, similar to opening a lock with a multi-molecular key. A well known example for such a "cellular adhesion key" is the adenovirus. On its surface five ligands are arranged in a pentagonal crown structure with a side length of about 6 nm (Stewart et al., 1997). This pentameric ligand arrangement promotes the penetration of the adenovirus into lymphocytes by binding to receptor proteins in the cell membrane. Only the ligand pentamer is able to stimulate the adhesion of the adenovirus, in contrast to the ligand monomer (Stupack et al., 1999).

A way to shed light on the effect of variations in integrin binding site spacing on cell adhesion is by measuring the cell adhesion strength. This should give a first insight into the physical properties of adhesive cell contacts. In order to measure cell adhesion strength, force spectroscopical methods had to be established, which are suitable for performing live cell experiments. With such devices, the following questions are addressed in this thesis:

(i) Does the binding site spacing of single integrins influence cell adhesion strength? (ii) At what timescale are adhesion processes affected by the pattern of integrin binding sites? (iii) Is there any evidence for a cooperative interaction of integrins, which can be deduced from the cell adhesion strength? (iv) Is it possible to measure the forces needed to detach focal contacts and how does focal contact formation affect cell adhesion strength? Studies on adhesion strength are substantially connected with information on surface energy. The enormous relevance of the biotin-streptavidin system for many biotechnological applications was the reason for choosing this system for an approach to tune the surface energy with biofunctionalised nanopatterns. A basic microinterferometric investigation of surface energy on streptavidin functionalised nanopatterns is presented in this thesis.

The novel approach of investigating adhesion properties and adhesion strength as a function of protein binding site spacing is intended to provide a contribution for a deeper understanding of *in vivo* and *in vitro* adhesion processes and their physical properties.

This thesis is divided into four parts. In the first part, an introduction to the biological and physical background of cell adhesion is given. In the second part, the most important methods, such as surface structuring and functionalisation techniques are presented. In addition, the microinterferometric and force spectroscopical techniques are introduced. The third part shows results for the adhesion of cells and a biomimetic model system on nanopatterns. The last and largest part of this thesis presents a characterisation of cell adhesion forces for initial and long-term adhesion processes.

Part I

Principles of Adhesion

1 Cell-Surface Interactions

Cells are the essential building blocks of all living creatures. Their ability to reproduce lets them assemble into tissues and form entire organisms. A crucial process in the life of a cell is cell adhesion, which affects cell motility, cell shape and regulates the activation of diverse signaling networks.

In this chapter, the cell and its components are introduced first. Then, the biological events during the adhesion process are described, including the formation of molecular adhesion clusters. Finally, an overview of several recent biophysical studies of cell adhesion is given.

1.1 The Connective Tissue

The majority of cells in the body are cooperatively organised in the form of tissues. Tissues are composed both of large cell assemblies that fulfil a certain common purpose and of the extracellular matrix (ECM), a material of fibrous proteins and polysaccharides that provides the cells with a scaffold to live in. In vertebrates there exist several types of tissue, for example nervous, muscle, epithelial and connective tissue. The cells in the connective tissue, for example in the skin and in tendon, are called fibroblasts. Fibroblasts play an important role in producing and rearranging the ECM, since they secrete the ECM-forming proteins and define the ECM structure by mechanically rearranging it. This is important, because the strength of the connective tissue is mainly provided by the ECM. Understanding the interactions of fibroblasts with the ECM and with ECM-derived proteins is an essential step towards the understanding of the mechanical cohesion of tissue.

All such interactions of the cells with their surroundings are maintained by several cell compartments in order to regulate the contact and communication with the cell exterior, to adapt the cellular behaviour and at the same time to retain the cell as elemental unity of life.

A cell can roughly be divided into the following parts: The cell envelope, the cytoskeleton, the nucleus and the cytosol with its embedded organelles (figure 1.1).

The cell envelope separates the cell interior from the extracellular space. It consists of an approximately 5 nm thick lipid membrane and of the glycocalix, a several nm to µm thick layer of polysaccharide molecules, which act as repellers but can in certain cases even regulate cell attachment (Alberts et al., 1997; Cohen et al., 2003). In the cell membrane many transmembrane proteins are embedded, some of them providing channels for intermembrane transport, others are functioning as handles to fasten the cell contact with the ECM.

The cytoskeleton provides the cell with mechanical stability and organises some part of

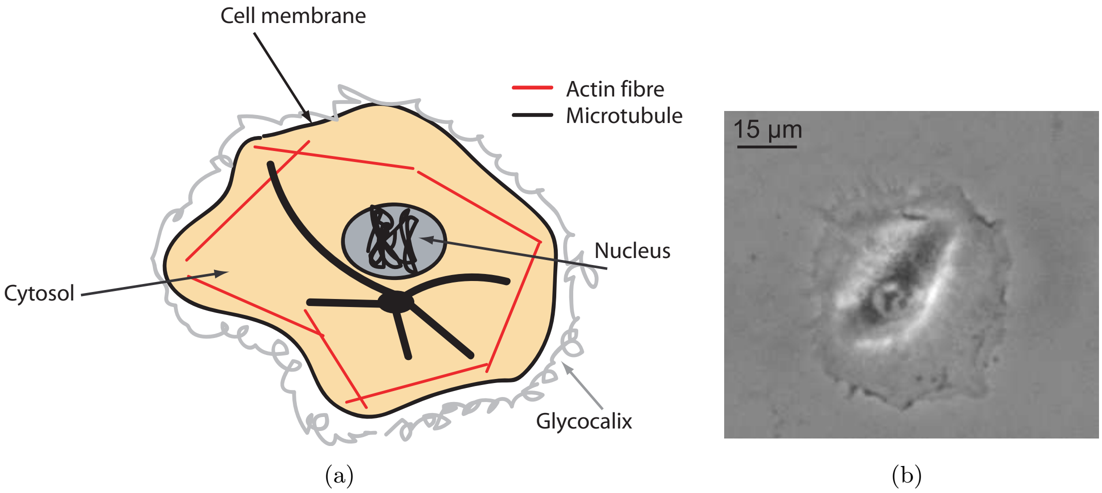

Figure 1.1: (a) Sketch of the structural elements of a cell. (b) Phase-contrast image of a fibroblast cell.

the intracellular transport. It consists of three basic elements: The intermediate filaments (diameter ≈ 10 nm), the actin fibres (diameter ≈ 5-9 nm) and the microtubuli (diameter ≈ 25 nm). Intermediate filaments are rope-like fibres with high tensile strength, therefore resisting mechanical stress during force application. Actin filaments are essential for executing cell movements, phagocytosis[1] and cell division. Particularly in muscle cells the actin filaments are indispensable, since they provide the main part of the muscle's contractile apparatus. The main task of the microtubuli is to fix the position of intracellular organelles and to support the cell during division with a mechanical framework, the mitotic spindle. In contrast to the actin filaments, which are analogous to thin and flexible ropes, microtubuli are relatively stiff rods. Whereas intermediate filaments are distributed over the whole cell, actin filaments form a cortex at the inside of the cell membrane and microtubuli grow out from the so-called centrosome, a small structure close to the cell centre.

The cell nucleus is the centre of information storage, where the genetic code is preserved. It is embedded into the cytosol, an aqueous gel holding several cellular organs and serving as a pantry for many proteins. This composition of elastic and fluid-like components results in the strong viscoelastic behaviour observed for cells and their constituents.

In a higher organism, each cell type is specialised for the function it has to execute. Thus, the detailed cell composition and structure varies significantly between different cell types. For example, red blood cells are responsible for oxygen transport and should not adhere to or coagulate in blood vessels. In contrast to this, white blood cells need to adhere and even penetrate through vessels to fulfill their responsibilities in preventing inflammation. The cells used in this thesis, fibroblasts, are derived from mammalian connective tissue. They are supposed to equip the tissue with mechanical stability and to form higher-order functional units, such as organs. (Alberts et al., 1997)

---

[1] Phagocytosis is the internalisation of particles by a cell.

1.2 The Cell Adhesion Machinery

Cell-cell and cell-matrix adhesion, are complex, highly organised processes that are important for many cell functions including cell movement, cell differentiation and programmed cell death (Blau and Baltimore, 1991). Decisive in the regulation of cell adhesion is the interplay between nonspecific repulsion and the specific binding of adhesion receptors embedded in the cell membrane (Sackmann and Bruinsma, 2002).

The basic mechanism of many cell adhesion events proceeds in two steps. Firstly, single cell adhesion receptors bind to their respective ligands at the cell exterior. This step is followed by the recruitment of a variety of proteins to distinct binding sites in order to induce the formation of adhesion clusters.

1.2.1 Cell Adhesion Proteins

There exist five superfamilies of cell adhesion molecules (CAMs) mediating cell adhesion: Immunoglobulins, cadherins, selectins, mucins and integrins. Each of them is responsible for a certain type of interaction. Immunoglobulins and cadherins mediate homophilic cell-cell adhesion, with the difference that only cadherin binding implies a linkage of the adhesion site with the cytoskeleton. Selectins also mediate cell-cell adhesion but in contrast to the homophilic interaction of cadherins they bind to the carbohydrate chains of mucin-like CAMs in adjacent cells. Such relatively weak transient interactions are important between leukocytes and endothelial cells and allow leukocytes to leave the blood stream in order to reach inflammation sites. The CAM superfamily that plays a key role in mediating cell-matrix adhesion is the integrin family. (Lodish et al., 1999)

Integrins are transmembrane glycoproteins and manifest their importance by providing a physical linkage between the extracellular environment and the cytoskeleton. This linkage is essential for the stability of cell architecture, adhesion and migration (Beckerle, 2002) and it enables integrins to directly transmit stress from the ECM to the cytoskeleton.

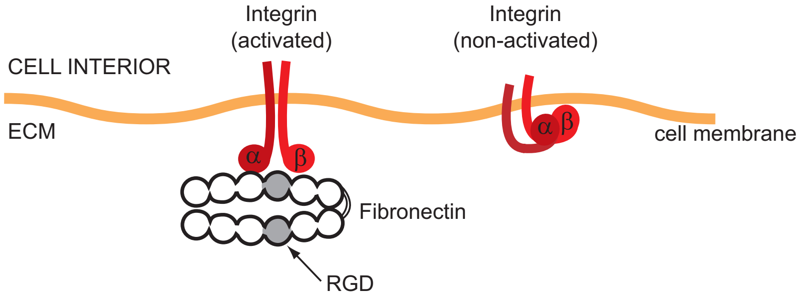

Figure 1.2: Sketch of integrin binding to the RGD sequence in fibronectin. A conformational change of the integrin arises due to its activation by binding to the RGD sequence.

Integrins have a heterodimeric structure, consisting of the so-called α- and β-subunits which are associated by non-covalent interactions. There exist 24 types of integrins which are composed of a combination of eighteen different α- and eight different β- subunits. Each integrin type prefers a certain adhesion receptor in the extracellular matrix and binds to it with a particular affinity (Hynes, 2002). One prominent integrin binding protein found in the extracellular matrix is fibronectin (FN). Fibronectin is a large glycoprotein, that contains the RGD (arginine-glycine-asparagine) sequence, that is a binding site for eight different integrin types (Pierschbacher and Ruoslahti, 1984). Among these is the $\alpha_V\beta_3$ integrin. The interaction of integrins with the extracellular environment occurs via their large head domains, whereas the connection to the cytoskeleton is maintained through their shorter cytoplasmic tails (see figure 1.2). Normally, a cell expresses several types of integrins leading to a mixture of integrins involved in cell-substrate interactions. The fibroblast cell line[2] used in the studies presented here is the rat embryonic fibroblast line (REF 52 wt), which is stably transfected with YFP paxillin, a cytoplasmic molecule present in focal contacts. REF 52 wt cells are expressing the integrin $\alpha_V\beta_3$.

1.2.2 Cell Adhesion Clusters

In order to achieve stable adhesion, cells form multiprotein assemblies known as cell adhesion clusters. Such a cluster formation is important because the strength of most specific biological bonds is relatively weak compared to covalent bonds. If cell adhesion was only mediated by single bonds, the stability of adhesion would be severely limited. One way out of this difficulty is the formation of adhesion clusters. By clustering many adhesion bonds in one region, adhesion is significantly strengthened through two mechanisms: Firstly, when a cluster is loaded by a force, this force can be distributed over the cluster constituents, so that the load acting on a single bond decreases and thus its unbinding probability is lowered. Secondly, when a bond inside the cluster breaks, the probability for a rebinding of molecules is high since the region of possible receptor diffusion is spatially confined by the other bonds in the cluster.

In cells of the connective tissue there are prominent structures, which form during the time-course of integrin-mediated adhesion. The first minutes of adhesion are dominated by single molecule binding. With increasing adhesion time, more and more integrins cluster and induce an intracellular signalling cascade. This leads to the formation of large, hierarchically assembled protein clusters in the form of focal complexes, which later mature into focal contacts, also called focal adhesions (Zamir et al., 2000; Vogel and Sheetz, 2006).

For the formation of such big adhesion contacts, a random occupation of integrin binding sites is not sufficient. Instead, the cooperative clustering of integrins is essential for the promotion of adhesion (Miyamoto et al., 1995). For this clustering, an activation of integrins is necessary, which is dependent on the presence of soluble ions such as Mg^{2+} and Ca^{2+} (Cluzel et al., 2005). In the non-activated state, integrins have a three-dimensional structure reminiscent of a golf club, with the integrin head directing into the extracellular space. After ligand binding, integrins have been reported to elongate and open up (see figure 1.2). Since integrin activation has turned out to promote integrin clustering, this is possibly mediated by a direct interaction of the integrin tails (Li et al., 2003b). Other models propose that the binding of secondary proteins, such as talin, are responsible for integrin clustering (Cluzel et al., 2005).

After the first steps of integrin clustering, a variety of adaptor proteins binds to the intracellular parts of the initial adhesion patch in order to form a focal contact. Examples of such proteins are talin, vinculin, paxillin and focal adhesion kinase, which provide strong linkages between the adhesion patch and the actin cytoskeleton of the cell, as illustrated in figure 1.3 (Zamir and Geiger, 2001a; Critchley, 2000; Wehrle-Haller and Imhof, 2002).

Focal contacts do not only play an important role for cell mechanics and adhesion

---

[2] These cells were a kind gift from Benjamin Geiger (The Weizmann Institute of Science, Rehovot, Israel).

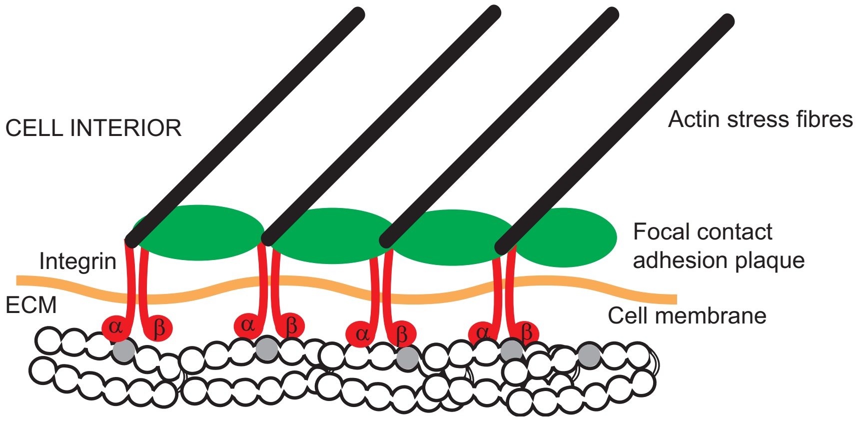

Figure 1.3: Schematic representation of a focal contact. The integrins in the cell membrane bind to their ligands in the ECM and are linked to actin stress fibres via proteins in the focal contact adhesion plaque (see Zamir et al. (2000)).

stability, but are also involved in signal transduction. Therefore integrin binding and focal contact formation critically influence the ability of cells to differentiate and proliferate; these processes modulate cell shape, polarity, gene expression and cell survival as well as apoptosis (Hynes, 2002).

1.3 A Closer Look at Adhesion

Due to the importance of integrin mediated adhesion, a multitude of studies are ongoing to elucidate the mechanical and biological properties of integrin-rich adhesion structures. Some of these studies are reviewed in this section.

1.3.1 Dynamics of Adhesion Structures

Cell adhesion structures can be transient or rather stable. Transient adhesion structures include microspikes, filopodia and focal complexes. Microspikes are membrane-enclosed structures that contain actin fibers and fascein; they are 2-10 µm long and 0.2-0.5 µm in diameter. Filopodia are larger counterparts of microspikes with a length of 20-200 µm and they contain additionally to actin also integrins and syndecans. Both microspikes and filopodia are used by the cell to explore the substrate in order to direct cell adhesion and migration (Adams, 2001; Albrecht-Buehler and Goldman, 1976; Albrecht-Buehler, 1976). Focal complexes are the predecessors of mature focal contacts. Due to a mechanical stimulus they can transform into focal contacts (Riveline et al., 2001). The protein content of focal complexes is similar to that of focal contacts, although focal complexes lack proteins such as zyxin and tensin as well as a coupling to actin stress fibres (Zaidel-Bar et al., 2003).

Focal contacts, although being rather stable in shape, show a rapid turnover of their constituent proteins, as has been shown by photobleaching fluorescently labelled integrins and studying the recovery of the fluorescence signal (fluorescence recovery after photobleaching, FRAP). These experiments demonstrated that the integrin content of a high-density focal contact was completely exchanged within 5 to 10 minutes. This proved that the integrin binding dynamics play an important role also for stable adhesion clusters and that binding and rebinding inside the cluster indeed occurs. (Ballestrem et al., 2001)

1.3.2 Mechanical Properties of Adhesion

A variety of techniques for force-application measurements have been used to study the interaction between cells and substrates. In early adhesion strength measurements, cells were allowed to adhere to substrates and were subsequently placed into a specially designed centrifuge, so that the centrifugal force was exerted normal or tangential to the surface (Thoumine et al., 1996; Chu et al., 1994). Although this setup appears very primitive at first glance, it has allowed the reinforcement of adhesion by the centrifugal force to be studied (Koo et al., 2002). The disadvantage of centrifugation assays is that no information on adhesion at the single-cell level can be received.

In recent years many new devices have been developed, allowing measurements to be performed even at the subcellular level. An overview of some of those techniques is given in figure 1.4. An important technique, which allows a high throughput for cell-surface adhesion measurements, is the application of a laminar flow, as shown in figure 1.4 a. With flow chambers shear stresses up to several tens of $\mu N/cm^2$ can be exerted on cells. Flow chambers have proven to be applicable for answering a variety of biological questions. They are particularly useful for studying so-called *catch bonds*, that are bonds reacting by strengthening their adhesion upon force application. An example for a catch bond has been found in rolling leukocytes, allowing them to stick to the surface of blood vessels in spite of being pushed forward through the blood stream (Dwir et al., 2003; Forero et al., 2004).

Optical tweezers, which trap nano- or micrometre sized particles in the center of a laser focus (figure 1.4 b), have been employed to measure the interaction of cells with adhesive substrates (Thoumine et al., 2000). Optical tweezers also allowed to prove the reinforcement of cytoskeletal linkages at integrin binding sites upon force application, showing that integrin contacts play a role in cellular mechanosensing (Choquet et al., 1997).

Magnetic tweezers (figure 1.4 c) have been widely used to perform microrheological or local deformation studies on cells (Feneberg et al., 2004), but also to investigate the substrate interaction of membrane systems, such as vesicles (Boulbitch et al., 2001; Smith et al., 2006a), and to study single molecule properties (Strick et al., 2000).

Although optical and magnetic tweezers can in principle be employed to study cell-substrate interactions, their application is restricted due to their limits in achieving higher forces than 100 to 200 pN. Therefore other techniques, especially atomic force microscopy (AFM), are a good choice when large forces in the nN regime are to be measured. With the AFM, forces are exerted through an elastic lever arm, the cantilever. Its deflections are measured by the signal of a reflected laser beam (figure 1.4 d). Depending on the force constant of the cantilever, very large and very small forces can in principle be measured. The lower limit of resolution is set by the thermal noise and the force constant of the cantilever and it is typically in the piconewton regime. AFM has successfully been used to quantify single molecule interactions both for live cells and artificial adhesion templates (Benoit et al., 2000; Touhami et al., 2003).

Another widely used, although quite complex technique is the application of forces by micropipettes (Chu et al., 2004). Ideally such experiments are carried out in combina-

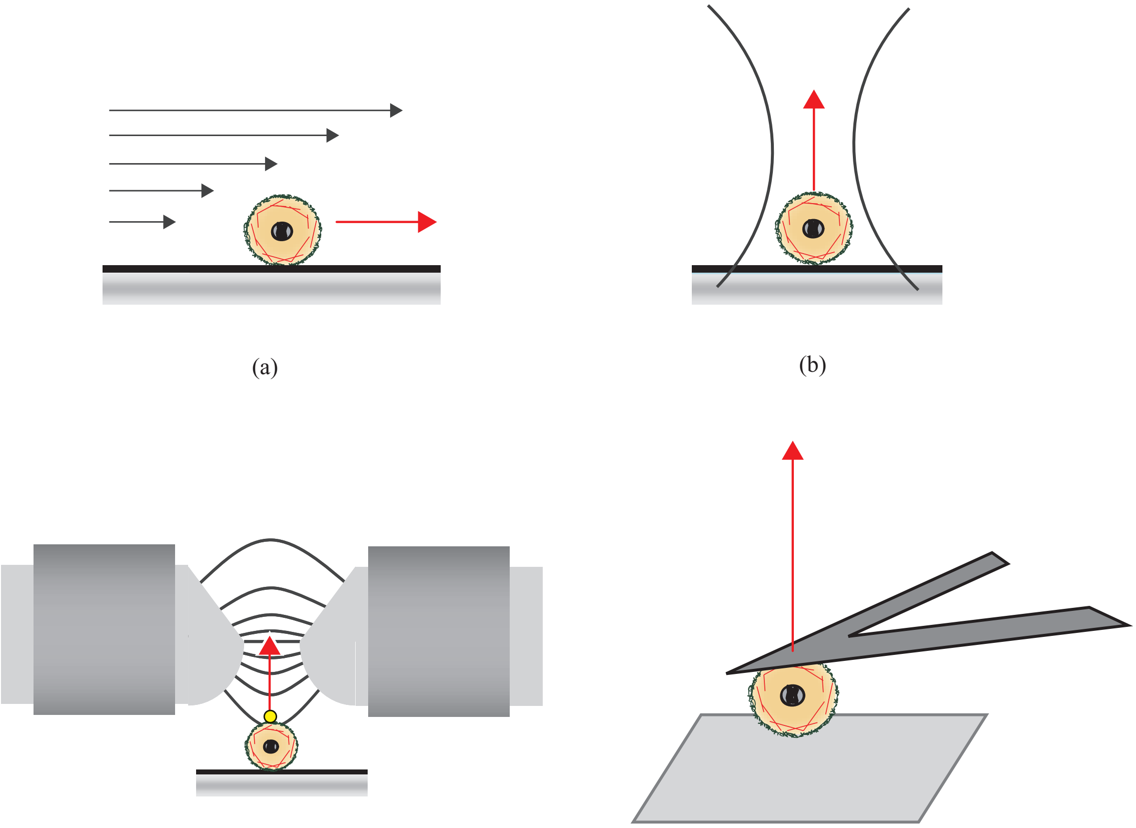

(a) (b) (c) (d)

Figure 1.4: Methods for measuring the adhesion strength of single cells: (a) laminar flow chamber, (b) optical tweezers, (c) magnetic tweezers, (d) atomic force microscopy (AFM).

tion with a vesicle to act as a spring, where the deformation of the vesicle gives precise information on the forces acting at the rim of the vesicle contact area (Prechtel et al., 2002).

Other setups, for example the permanent magnetic microneedle technique, have been used to probe the viscoelastic properties of focal contacts. In such a setup, a focal contact is formed at the position of a magnetic bead and this bead is subject to the force which is applied by a retracting microneedle, as sketched in figure 1.5 b (Matthews et al., 2004).

Instead of applying forces externally to cells, it is also possible to monitor the forces actively exerted by the cells themselves. Such experiments, which concern the mechanical properties of focal adhesions, were performed on adhesive soft polymer gels. Micrometre-sized fluorescent markers were introduced into the elastic polymer matrix so that the forces exerted by single focal contacts could be followed by monitoring the position of the markers (Balaban et al., 2001). Balaban et al. (2001) obtained a linear relationship between exerted force and focal contact area and determined a mean stress of 1.5 kPa which is applied to the surface by focal contacts.

Similar results were obtained by employing elastic polymer microneedles. In such experiments, the forces applied by single focal contacts were determined from the deformation

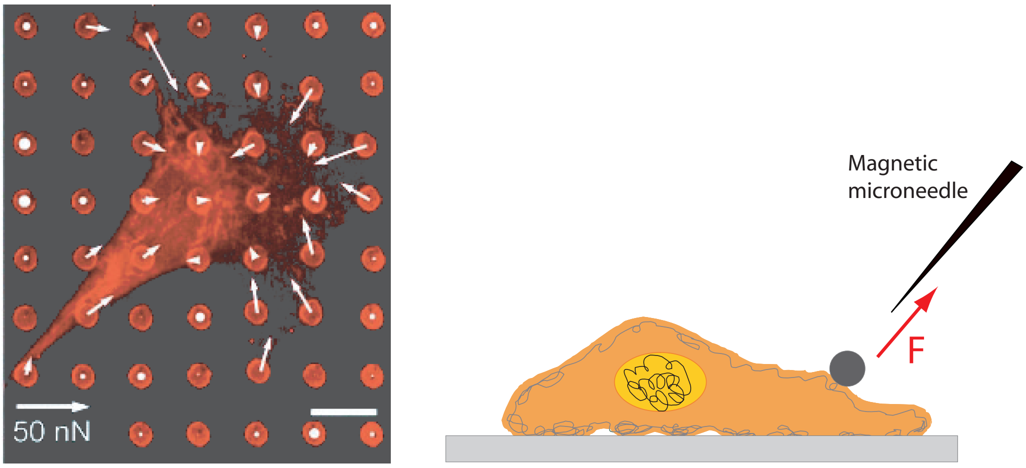

(a) (b)

Figure 1.5: (a) Deformations of elastic microneedles (red circles) caused by a cell spreading onto this "nailbed". The direction of the bending of microneedles is marked with arrows (from Tan et al., 2003). (b) Permanent magnetic microneedle for studying the viscoelastic properties of a focal contact. A focal contact is formed at an RGD functionalised magnetic bead and the magnetic microneedle is moved while the position of the bead is monitored (Matthews et al., 2004).

of the microneedles. An image showing the deformation of microneedles by a cell is given in figure 1.5 a (Tan et al., 2003).

1.3.3 Manipulation of Adhesion by Surface Engineering

In order to investigate and mimic the ideal adhesion conditions provided by the ECM, artificial adhesive surfaces have been designed and their effects on cell adhesion have been studied. Substrate stiffness, for example, has been shown to alter adhesion structure and dynamics as well as cytoskeleton assembly and cell spreading (Discher et al., 2005). If cell adhesion sites were provided in the form of a three-dimensional matrix instead of a two-dimensional substrate, cell attachment, motility, proliferation and morphology were strongly affected (Cukierman et al., 2002).

An early study that investigated the effect of different spacings between extracellular ligands indicated that an RGD ligand spacing of less than 440 nm is necessary to induce focal contact formation (Massia and Hubbell, 1991). A more sophisticated approach used self-assembling polymers to define the surface density of RGD and has allowed the necessity of local integrin clusters for cell adhesion to be studied (Maheshwari et al., 2000; Koo et al., 2002). The disadvantage of this method is that it lacks the possibility of precisely defining integrin binding sites. However, in recent years an elegant technique allowing such a predefinition of binding sites has emerged by using nanopatterned substrates.

Studies using nanopatterns to provide RGD-based, quasi-hexagonally arranged integrin binding sites have indicated the existence of a critical distance of integrin binding sites for cell spreading and focal contact formation (Arnold et al., 2004). In particular, it was shown that cells spread well when the integrin binding site spacing is 28 or 58 nm, whereas cell spreading is strongly restricted for spacings of 73 and 85 nm (see figure 1.6 a). The effect of different integrin binding site spacings on focal contact formation is shown in figure 1.6 b. Focal contacts are in these images identified by clusters of the focal contact protein vinculin. For an integrin binding site spacing of 58 nm focal contacts are large and colocalised with actin stress fibres. A distance of integrin binding sites above 73 nm restricts focal contact and actin stress fibre formation. These results suggest the existence of a critical distance for integrin binding sites, above which integrin clustering is cut down (Arnold et al., 2004).

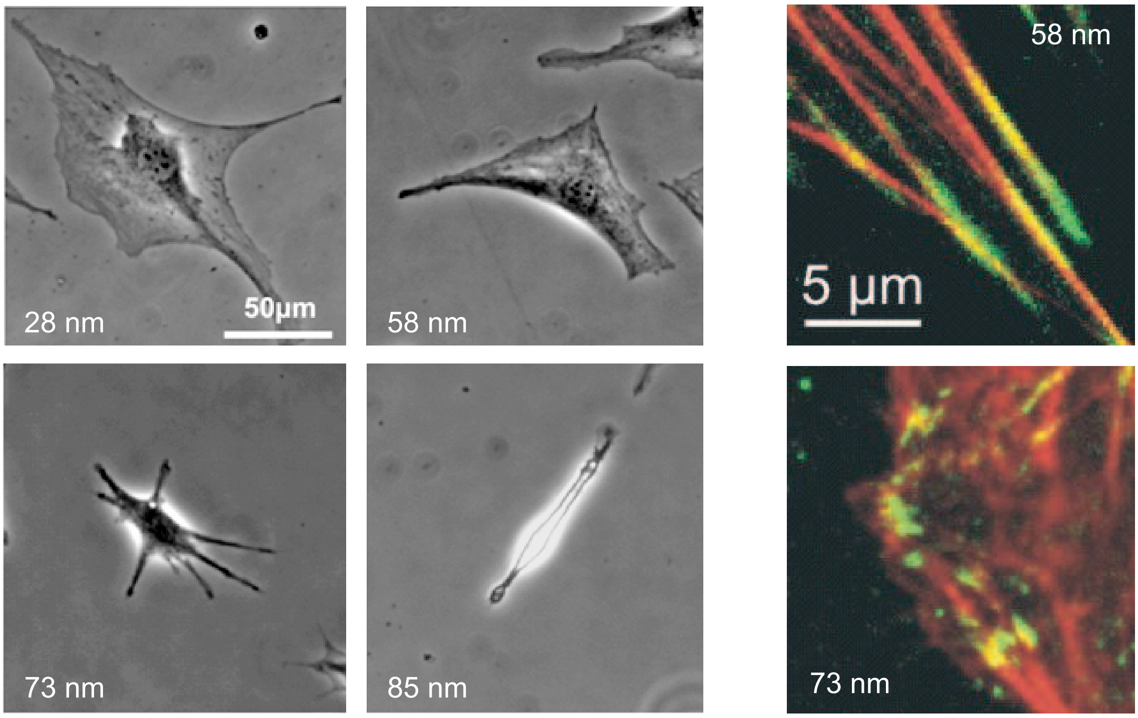

(a) (b)

Figure 1.6: (a) Cell spreading and (b) focal contact formation on substrates which offer different distances of integrin binding sites (28, 58, 73, 85 nm). (a) Phase-contrast images of cells after adhering to the substrates for one day. (b) Vinculin (green) and actin (red) staining of focal contacts and actin stress fibres of cells after 24 hours in cell culture. The images were kindly provided by M. Arnold and A. Cavalcanti-Adam (see Arnold et al. (2004)).

2 Physical Adhesion Concepts

Biological adhesion is regulated by two fundamental types of interactions: nonspecific and specific interactions (Sackmann and Bruinsma, 2002). Nonspecific polymer interactions have turned out to play a key role in the initial contact of cells and surfaces (Zimmerman et al., 2002). On the other hand, the formation of specific molecular bonds and molecular clusters during cell adhesion is essential and responsible for many cell activities (Hynes, 1999). In this chapter, an overview of some physical concepts of adhesion is given.

2.1 General Adhesion Models

The simplest possible adhesion system is a completely inert, rigid body. The contact area formed between such a body and a non-planar identical body will always be restricted to a single point, since the formation of an extended contact zone is not possible. The situation is different for elastic bodies. A first approach to describing the contact areas of non-interacting elastic bodies was provided by Heinrich Hertz (1882) with his essay *Über die Berührung fester elastischer Körper* (On the contact of rigid elastic solids). In this theoretical work, the deformation of an elastic material as a result of an external, compressive force is described. The Hertz model is frequently applied for determining the elastic moduli of materials, even for cellular systems.

Although the Hertz model is widely applicable, it is limited by the condition that the participating bodies do not have any adhesive affinity. This is of course a strong simplification and does not reflect the real properties of most materials, where adhesive interactions indeed play a leading role. An approach that includes such adhesive interactions was proposed by Johnson, Kendall and Roberts in the 1970s (JKR model). This continuum mechanical model determines the magnitude of a contact area between interacting bodies as a function of the degree of adhesion (Johnson et al., 1971). The idea of the model is that the surface energy released on adhesion is used for the elastic deformation of the interacting materials. One critical aspect for the applicability of the JKR model is the ratio of elasticity and adhesion strength (Johnson and Greenwood, 1997). Although the JKR model is mainly used for characterising passive material properties, it has also been applied for describing the interaction of cells (Chu et al., 2004).

2.2 Specific Adhesion in Biological Systems

Biological adhesion is based on the specific interaction of proteins, sugars or lipids. Already in 1978, Bell pointed out in his pioneering article on the specific nature of cell adhesion, that nonspecific electrostatic interactions between cell membranes cannot be made responsible for the strong forces acting between cells. Instead, these force were suggested to be mediated by specific biological bonds (Bell, 1978). The binding mechanism of such specific bonds is very different from that of chemical bonds: the binding partners in specific bonds match closely in shape which allows a relatively strong binding through hydrogen bonds and van der Waals interactions to be established. However, specific bonds are weaker than typical covalent bonds. For example, the free energy for the specific binding of biotin to streptavidin is 35 kT (Green, 1990). A covalent C-C bond is with 150 kT much stronger, although the biotin-avidin bond is one of the most stable specific bonds known (Boal, 2002). Examples of specific bonds in organisms are antibody-antigen binding, the binding of motor proteins to the actin transport highways, the binding of enzymes and hormones, and most importantly for this thesis: the receptor-ligand binding in cell adhesion.

Biological bonds typically have binding energies of the same order of magnitude as the thermal energies, thus the bonds can easily be released if required. This competition of binding with thermal energy leads to a finite bond lifetime and a stochastic decay of adhesion. To describe a thermodynamically induced break-out of bonds from the minimum of the potential energy landscape, Kramers' theory can be applied. This theory was originally developed in the 1940s by Kramers in order to calculate chemical reaction rates. It can also be used for describing binding events in terms of a thermally assisted escape of a particle through the transition state barrier of a potential well (Kramers, 1940; Hänggi et al., 1990; Evans, 2001).

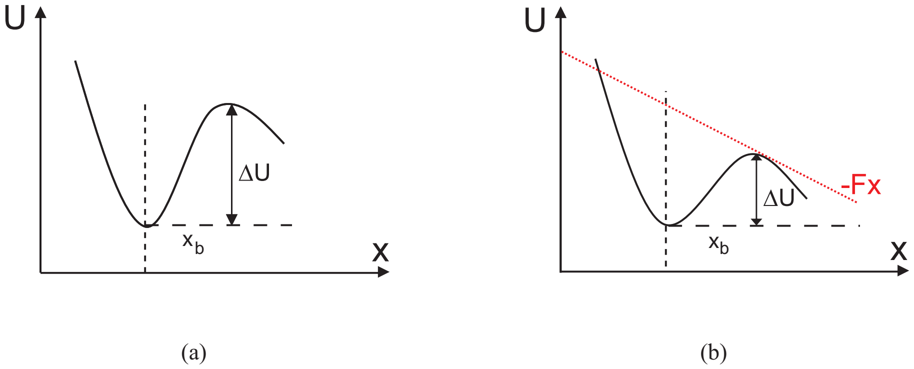

(a) (b)

Figure 2.1: Model for a one-dimensional binding potential with a single transition barrier, (a) at zero force and (b) when an external force is applied.

By applying Kramers' approach, the statistical failure of a bond can be related to a dissociation rate k_0, which is the inverse of the average transition time over the barrier and proportional to the Arrhenius factor, $\exp(-\Delta U/k_BT)$. Bell (1978) proposed in a simple analysis that the application of a force leads to a tilt in the effective potential well, which allows an easier escape of the bond over the transition state barrier (figure 2.1). This effect is accounted for by an increase in the dissociation rate from k_0 to $k = k_0 \exp F/F_0$ with $F_0 = k_BT/x_B$. F_0 is the internal force scale of the bond and defines the typical force scale of bond rupture.

The implications of a force application on the unbinding behaviour of single receptor-ligand pairs can by studied with *dynamic force spectroscopy*. In such experiments, the bonds are loaded in a time-dependent manner and the forces necessary to break the bonds are studied. Such forces are in general referred to as *unbinding forces*, which denote the most frequent rupture force in the force distribution. In the majority of experiments, the loading force increases linearly with time, as is expressed by the loading rate $r = dF/dt$. The theoretical basis for the dependence of unbinding force and mean-first-passage time on loading rate was derived in the late 1990s (Evans and Ritchie, 1997; Shillcock and Seifert, 1998). The analysis by Evans and Ritchie (1997) has revealed a linear dependence of the unbinding force on the logarithm of loading rate. This has been frequently verified experimentally, for example in the streptavidin-biotin system (Merkel et al., 1999). As shown in figure 2.2 a, the distribution of rupture forces indeed depends on the loading rate. Figure 2.2 b shows several linear regimes for the dependence of the unbinding force on the logarithm of loading rate. Each of the different slopes in the dynamic strength spectrum is associated with a particular transition state barrier. Three transition state barriers have been obtained for the avidin-biotin bond and two for the streptavidin-biotin bond.

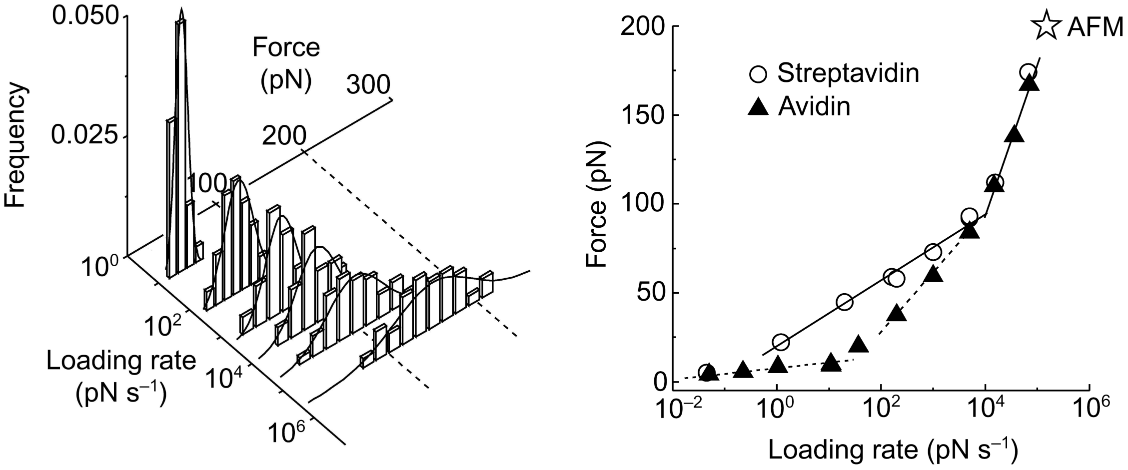

(a) (b)

Figure 2.2: Dynamic force spectroscopy determined the dependence of unbinding forces on loading rate. (a) The distribution of rupture forces for the streptavidin-biotin bond at different loading rates. (b) The most frequent rupture forces, which vary with the logarithm of loading rate. For the streptavidin-biotin bond two transition barriers were obtained, for the avidin-biotin bond three (from Merkel et al. (1999)).

With dynamic force spectroscopy it has even been possible to study the integrin $\alpha_V\beta_3$ interaction with fibronectin for live cells, revealing a two-well binding potential for this system (Li et al., 2003a). However, in nature single bonds are the exception. They can be detected experimentally by restricting the interacting areas to very small regions, but their relevance in biological systems is restricted to very short adhesion timescales. The regulation of many biological interactions occurs via the formation of molecular adhesion clusters, whose physical properties are the subject of the next section.

2.3 Multiple-Bond Adhesion

An adhesion cluster is defined as a combined system of multiple bonds. The distribution of applied forces among the participating bonds can take place in different configurations, as sketched in figure 2.3.

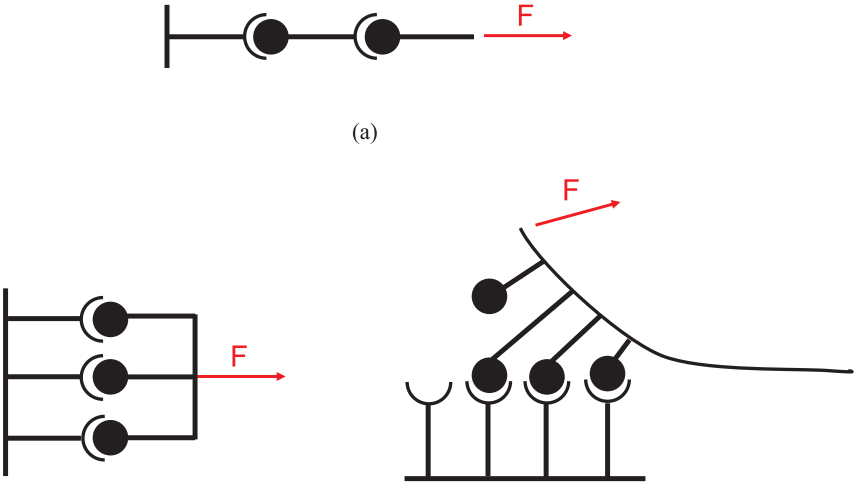

(a)

(b)

(c)

Figure 2.3: Different configurations of molecular bonds in an adhesion cluster. (a) In *serial loading*, all bonds are subject to the same force. (b) In *parallel loading*, the force is equally shared among the bonds in the cluster. (c) In the *zipper* system, one bond is loaded after the other.

In the *serial loading* (figure 2.3 (a)), each bond has to resist the same force. In *parallel loading* (figure 2.3 (b)) the force is shared between the bonds, therefore this situation is also referred to as *shared loading*. The situation is quite different in the case of a *zipper* configuration (figure 2.3 (c)). There, the force is shared unequally over several bonds and the bonds rupture one after the other, as when a piece of sticky tape is pulled off a surface.

Bonds in focal contacts are in physical models assumed to be arranged in a parallel configuration, since force transmitting actin stress fibres anchor in the contacts and are expected to distribute the force over the whole adhesion patch (Besser and Safran, 2006; Erdmann and Schwarz, 2006).

Molecular clusters react on applied forces in a similar way as isolated bonds, except for one difference: The number of bound molecules in the cluster can change and rebinding events are possible. This introduces a new variable into the system, the rebinding rate k_{on}. Rebinding occurs when the probability of bond renewal inside the cluster is nonzero. This can result from a restricted diffusion of binding partners inside the cluster and because the adhesive surfaces are kept in close proximity by the remaining bonds.

When a linear loading is applied to break a cluster, the behaviour of rupture time and rupture force depends on the magnitude of loading rate r and rebinding rate k_{on}. A detailed analysis reveals that in the regime of fast loading (large r), large forces are necessary to break the cluster and that rebinding events are negligible. For slow loading (small r), smaller forces break the cluster and a large rebinding rate can strongly amplify the cluster strength. On the other hand, if the rebinding rate is small, the cluster can even break spontaneously before it is affected by the external force (Schwarz, 2006). In addition to such deterministic analyses, also stochastic approaches to describe the cluster decay have succeeded. These models not only allow to draw conclusions on the mean-field effects of cluster decay, but instead precisely predict the course of cluster decay as a result of externally applied forces (Erdmann and Schwarz, 2004b; Erdmann and Schwarz, 2004a).

Experimentally there have been several approaches to study cluster properties, so far with relatively little success. However, a recent experiment that allowed to relate the binding strength of multiple bonds to loading rate has been performed by studying the adhesion of RGD-containing vesicles to the integrins of endothelial cells (Prechtel et al., 2002). In this study by Prechtel et al. (2002), a vesicle was tensed by micropipette aspiration, brought into contact with an endothelial cell and the adhesion zone was loaded with a defined force by retracting the micropipette (see figure 2.4 a). The force density at the rim of the vesicle-cell adhesion zone and the rate of the force density were deduced from the vesicle deformation during the experiment. In this experiment, a power law dependence of rupture forces on loading rate was observed (figure 2.4 b), in agreement with the theory proposed by Seifert (2002).

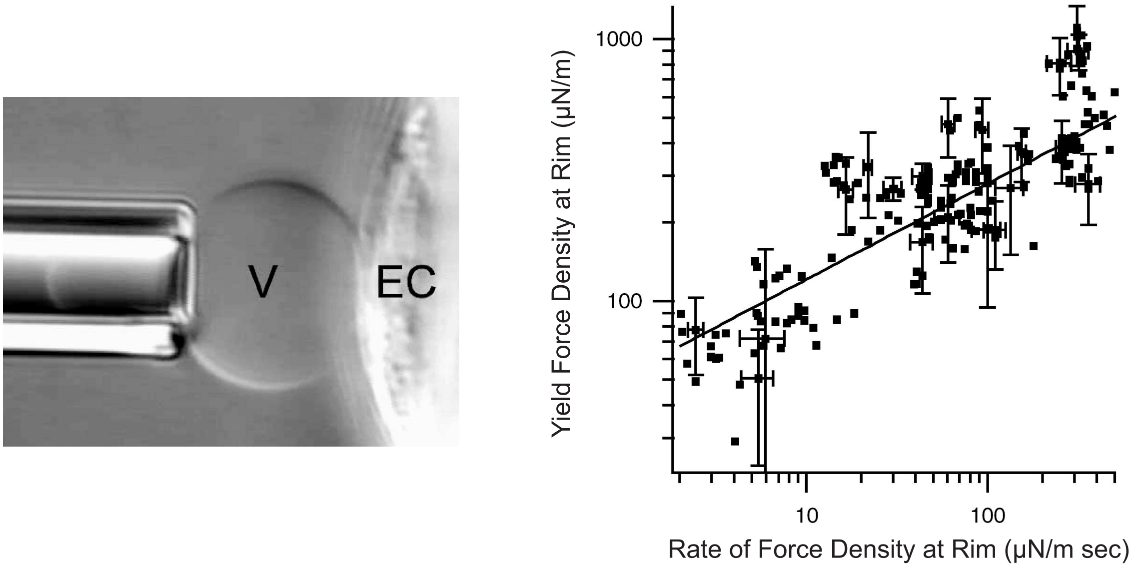

(a)

(b)

Figure 2.4: (a) Experiment, where an RGD containing vesicle (V) is brought into contact with an endothelial cell (EC). (b) Forces necessary to break the adhesion between cell and vesicle as a function of the rate of force application. The forces were normalised to the rim of the contact area between vesicle and cell, where the major part of the stress is applied (from Prechtel et al. (2002)).

Part II

Experimental Design and Measurement Techniques

3 Nano- and Microadhesive Templates

“There is plenty of room at the bottom” were Richard Feynman’s words 1959, and his statement should in the following decades be identified with the kickoff for the rapid developments in micro- and nanotechnology. Right now, micro- and nanoparticles are employed in many fields from computer chip devices to biosensors and even for everyday products, such as detergents.

In this chapter, the basic concepts of a bottom-up-approach to prepare biofunctionalised nanostructures is presented, which is essential for the studies of this thesis. Additionally, a conventional photolithographical approach for fabricating microstructures is touched on, since such substrates were employed for the studies presented in section 8.5. The precise protocols of these techniques are given in the appendix, including all necessary concentrations and conditions.

3.1 Gold Nanostructures

Controlling the arrangement of receptors in the cell membrane during cell adhesion requires a device, which defines a pattern of adhesion ligands on a substrate with nanometre precision. For achieving nanometre precision, conventional techniques, such as photolithography, fail. Using electron beam lithography, it is in principle possible to generate structures of a size between 5 and 200 nm (Kassing et al., 2000). However, this technique is rather expensive and time-consuming as well as restricted to conductive substrates. Both aspects hinder electron beam lithography from becoming a breakthrough technique for the preparation of bio-adhesive substrates: for biological studies, a large number of substrates must be available and additionally, these substrates must be suitable for optical microscopy. An alternative nanolithographical approach is to utilise the self-organisation of diblock copolymer micelles, which assemble into quasi-hexagonal patterns on many kinds of substrates, including conventional glass slides (Spatz et al., 1996; Spatz et al., 2000).

The most crucial step for the preparation of nanostructures with micellar nanolithography is the preparation of the micelle solution from amphiphilic diblock copolymers. Such polymers consist of two blocks of different polarity. When they are dissolved in solvents, micelles form above a certain polymer concentration, the so-called *critical micelle concentration* (cmc). The shape of the micelles (spherical, cylindrical) can be controlled by adapting the ratio of the two polymer blocks. For the preparation of quasi-hexagonal nanopatterns, the diblock copolymer polystyrene-block-poly-2-vinylpyridine is used. Its constituent polymers, polystyrene (PS) and poly-2-vinylpyridine (P2VP), are shown in figure 3.1. The PS block of the polymer is hydrophobic, whereas the P2VP block is hydrophilic. When these polymers are dissolved in the apolar solvent toluene in a concentration above the cmc, spherical micelles form. In such micelles, the PS arm of the polymer stays in contact with the toluene and the P2VP is hidden in the core of the micelle without being in contact with the solvent. When hydrogen tetrachloroaurate(III) trihydrate is added to this solution, it enriches in the core of the micelles (see the last step in figure 3.1). This is a result of its interaction with the P2VP and its low solubility in the toluene.

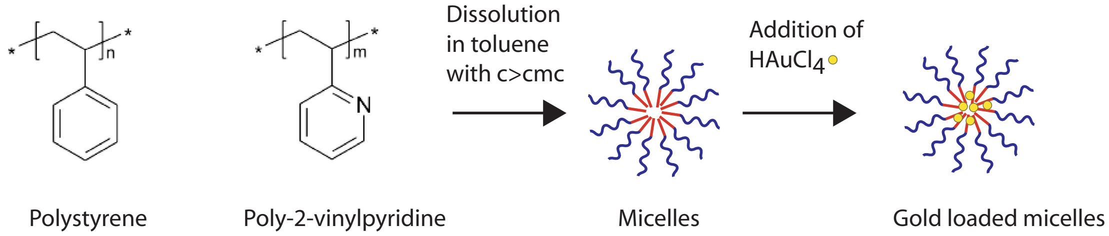

Figure 3.1: Left: Constituent polymers of the diblock copolymer, PS and P2VP. Middle: Micelle formation after dissolving the diblock-copolymer into toluene. Right: Final situation when the micelles are loaded with tetrachloroaurate.

By the dip coating of hydrophilic glass slides, silicon wafers or mica, the gold containing micelles self-assemble into a quasi-hexagonal arrangement. This dip coating is performed by dipping a clean substrate into the micelle solution and retracting it with a defined velocity. The depth of immersion defines the position of the *dipping edge* between the nanopatterned and the non-nanopatterned part of the substrate. To remove the micelle polymer, which is still surrounding the gold ions ($HAuCl_4$) at this stage, the surfaces are exposed to a hydrogen plasma. This treatment also leads to the reduction of the gold ions to elemental gold. A sketch of the preparation of quasi-hexagonally arranged gold dots from a micelle solution is given in figure 3.2.

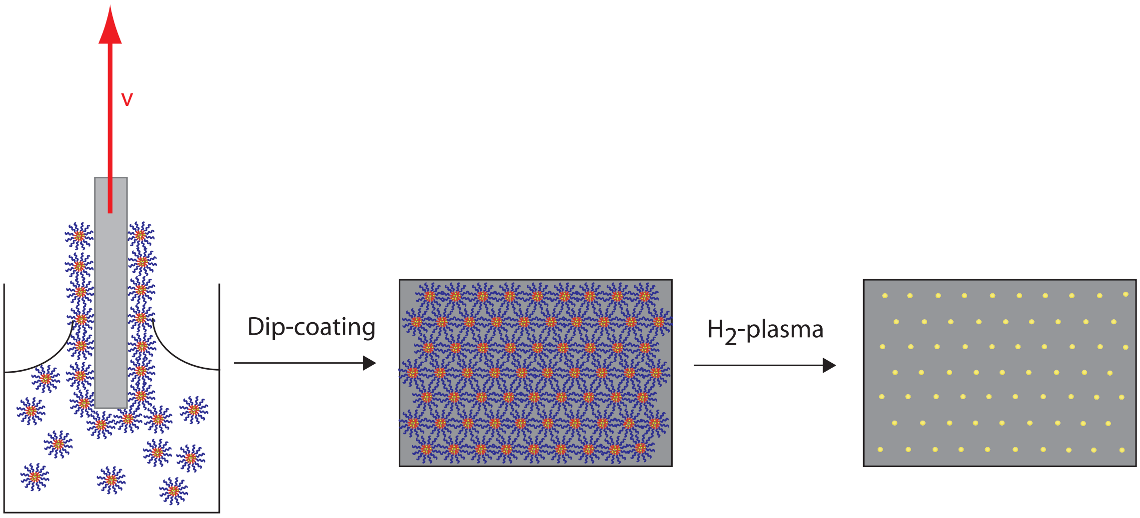

Figure 3.2: Sketch of the dip-coating procedure. A clean sample is dipped into the micelle solution. The micelle arrange on the sample in a quasi-hexagonal lattice and after a plasma treatment only the gold dots remain on the glass.

The inter-dot spacing of the quasi-hexagonal pattern is defined by the size of the micelle forming diblock copolymers (Spatz et al., 2000; Glass et al., 2003) and can up to now be varied between 18 and 300 nm. An additional variation of the gold dot spacings can be achieved by different dipping speeds (Arnold, 2005; Jakubick, 2005). The size of the gold dots is defined by the concentration of the tetrachloroaurate added to the micelle solution, but it is restricted by the size of the hydrophilic part of the block copolymer, where the gold ions are located. Therefore, smaller copolymers generally lead to smaller gold dots, a restriction which can be overcome by using electroless deposition of gold (Brown and Natan, 1998).

Nanopatterns can be visualised with scanning electron microscopy (see figure 3.3 b). Optical microscopy can only show contrast variations caused by the gold dots of the nanopattern (see figure 3.3 a). A characterisation of the average distance and orientational order of the gold dots in the quasi-hexagonal pattern was performed by analysing scanning electron images. The gold dot position was determined with sub-pixel resolution and their distance and orientation compared to that of a perfect hexagonal pattern[1]. The errors given for nanopattern spacings in this thesis denote the standard deviation of single gold dot spacings.

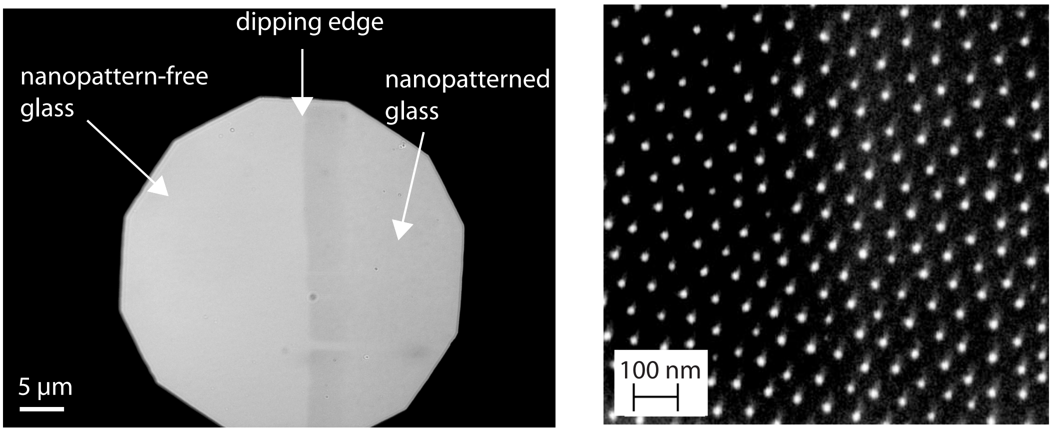

(a)

(b)

Figure 3.3: (a) Dipping edge of a nanopattern in reflection interference contrast microscopy (see section 4.3), showing a variation in contrast that is induced by the nanopattern. (b) Scanning electron micrograph of a nanopatterned glass slide.

3.2 Methods to Prevent Non-specific Protein Adsorption

In order to prevent nonspecific adhesion of proteins or the cell membrane to the free surface between the gold dots, this area was covered with a thin, protein-repellent polymer layer. A widely used polymer system to achieve such a passivation is polyethylene glycol (PEG). In the experiments of this thesis, PEG was either covalently bound to the substrates or adsorbed due to electrostatic interactions. Both methods are introduced in the following.

---

[1] The programs used for the analysis of nanopatterns were provided by Jennifer Curtis and Philippe Girard and written in IDL (IDL Research Systems) and for ImageJ, respectively.

3.2.1 Covalent coupling of mPEG2000-Urea to the surface

A first possibility to passivate the region between the gold dots is to bind a thin protein resistant layer of the linear molecule methoxy-polyethylene glycol-triethoxysilane (see figure 3.4). The PEG in this molecule has a chain length of $n = 43$ and a molecular weight of 2000 Da, thus it is commonly called PEG2000. This mPEG2000-urea molecule reacts with the OH^- groups of hydrophilic glass or silicon substrates via its triethoxysilane group and forms a monolayer on the substrate[2]. The thickness of the PEG layer in its dry state was determined by photoelectron spectroscopy to 2 nm, the thickness of the hydrated PEG layer is estimated to approximately 5 nm (Blümmel, 2005).

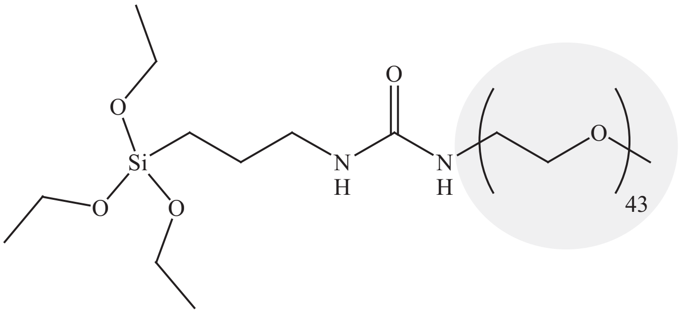

Figure 3.4: Chemical structure of the mPEG2000-urea. The PEG part of the molecule is shaded light grey.

3.2.2 Electrostatic Passivation with PLL-g-PEG

Besides a PEG immobilisation through covalent binding, PEG molecules can be grafted onto a polymer backbone, which in turn acts as a linker to the substrate. An example for such a backbone is poly-L-lysine (PLL), a highly positively charged polymer. Due to its large positive charge, PLL can interact electrostatically with negatively charged substrates, such as activated glass surfaces. The synthesis of PLL and PEG copolymers is well-established and a variety of PLL-g-PEG molecules[3] with different molecular weights and ratios of the PLL and PEG blocks are reported in literature (Sawhney and Hubbell, 1992). The mechanics and adsorption of PLL-g-PEG to substrates have been extensively studied by the group of Marcus Textor (ETH Zürich). This group also introduced bioreactive groups, such as RGD, into PLL-g-PEG without influencing its protein resistance (Huang et al., 2002; Ruiz-Taylor et al., 2001). The high protein resistance of PLL-g-PEG is impressive and has been proposed to be a result of both steric repulsion between the PEG molecules and hydrated protein shells and a kinetic hindrance of protein adsorption (Heuberger et al., 2005; Efremova et al., 2001). The PLL-g-PEG used in this thesis is the PLL(20)[kDa]-g[3.5]-PEG(2)[kDa], which has proven to provide an excellent non-fouling background passivation against cell adhesion (VandeVondele et al., 2003). The thickness of the hydrated PLL-g-PEG layer was determined with colloid-probe force measurements

---

[2] The mPEG2000-urea used in this thesis was synthesised by Jacques Blümmel.

[3] The full name of the polymer is (Poly(L lysine)-grafted-poly(ethylene glycol). An extended notation to PLL-g-PEG is PLL(x)-g[y]-PEG(z) with x and z denoting the molecular weights of the PLL and PEG, respectively, y is the graft ratio, i.e. the number of lysin monomers per PEG side chain.

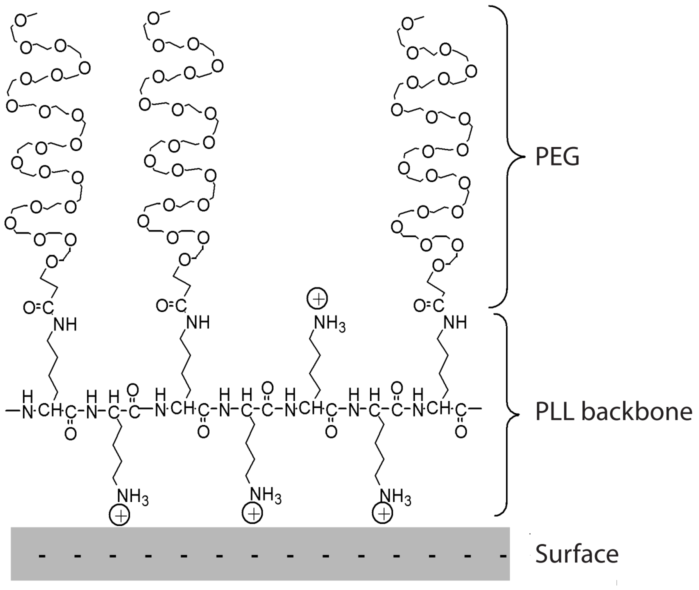

Figure 3.5: Adsorption structure of PLL-g-PEG on a glass slide. The positively charged PLL backbone binds to the negatively charged substrate and the PEG arms prevent a protein adsorption (from Pasche et al. (2005)).

to be 8.2 nm and the proposed adsorption structure onto a negatively charged surface is shown in figure 3.5 (Pasche et al., 2005).

The binding of PLL-g-PEG to the surface includes two steps. First, the substrates have to be activated by an oxygen plasma treatment to form OH^--groups on the surface[4]. After this activation, the incubation of the surface with an aqueous PLL-g-PEG solution immobilises the positively charged PLL backbone of the PLL-g-PEG electrostatically on the substrate.

3.3 Functionalisation of Gold Nanopatterns

To use gold nanopatterns as templates for studying specific adhesion, the gold dots have to be functionalised. An attractive mechanism is by covalently binding thiolated molecules to the gold dots. In this thesis, two systems of adhesion ligands are important: ligands for specific integrin binding and streptavidin as a ligand for biotinylated probes. The methods to bind these ligands to the gold nanopattern are the subject of this section.

3.3.1 Integrin Specific Functionalisation

As discussed in chapter 1.2, the integrin receptor in the cell membrane binds with high affinity to the RGD[5] motif of fibronectin molecules. The desired situation for our cell

---

[4] The plasma processes of oxygen and hydrogen are quite different and it was found that PLL-g-PEG sticks not as good to hydrogen plasma treated glass compared to oxygen plasma treated glass (personal information from J. Vörös, ETH Zürich).

[5] Shortcuts of the amino acids: R=arginine (arg), G=glycine (gly), D=asparagine (asp).

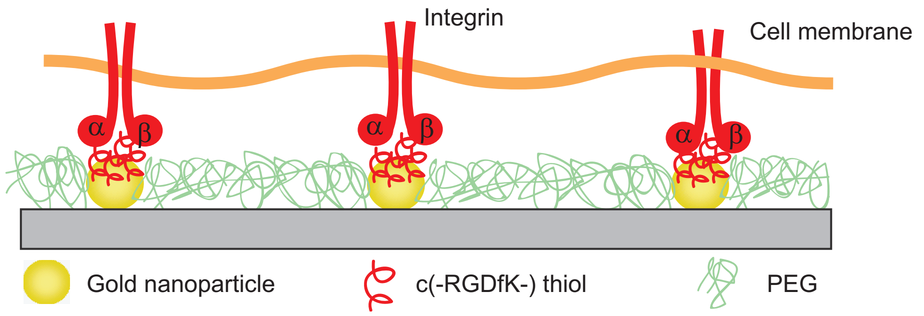

Figure 3.6: Substrate configuration desired for cell adhesion studies. The gold dots are functionalised with the c(-RGDfK-) thiol so that each gold dot serves as a binding site for an integrin. The region between the gold dots is covered with PEG.

adhesion studies is to expose the integrins in the cell membrane to a certain pattern of precisely defined RGD spots on the substrate, as shown in figure 3.6.

Compared to linear RGD peptides, the selectivity and affinity of RGD for certain types of integrins can be enhanced by changing its conformation. The group of Horst Kessler (TU München) has synthesised cyclic pentapeptides which contain the RGD sequence and strongly promote integrin binding (Haubner et al., 1997). In this thesis, the c(-RGDfK-) peptide is used, which binds with high affinity to the $\alpha_V\beta_3$ integrin (Pfaff et al., 1994; Kantlehner et al., 2000). To bind the c(-RGDfK-) peptide to the gold dots, it was modified by adding a thiolated alkane linker of approximately 2 nm length. Such a long linker is necessary to make a contact between the RGD and the integrin binding pocket possible (Hu et al., 2000). The chemical structure of the c(-RGDfK-) thiol is shown in figure 3.7.

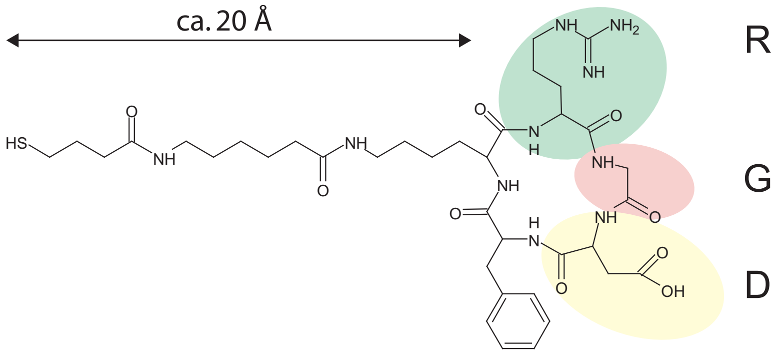

Figure 3.7: Chemical structure of the c(-RGDfK-) peptide. The functional RGD sequence is shown in colour.

When cells are brought into contact with passivated, RGD functionalised substrates, they immediately recognise the biofunctionalised nanopattern. As shown for a flow experiment in figure 3.8, the cells only bind to the biofunctionalised, nanopatterned part of the substrate and do not stick to the passivated surface.

For simplicity, the c(-RGDfK-) peptide is referred to as RGD peptide in the following.

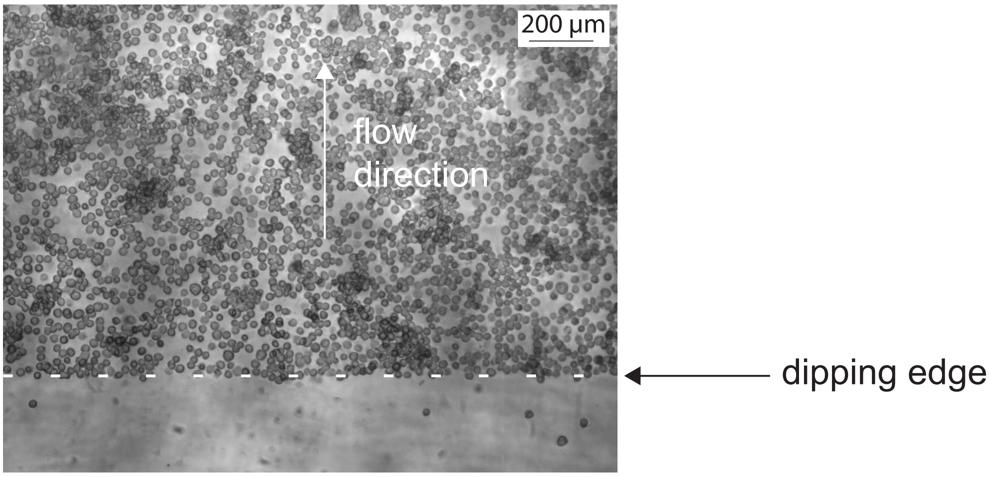

Figure 3.8: Phase-contrast image of cells adhering to a nanopatterned, RGD functionalised substrate under laminar flow. The dipping edge and the direction of flow are marked with arrows.

3.3.2 General Coupling of Proteins to Nanodots

The ability of functionalising nanopatterned substrates with arbitrary proteins is an important step towards studying manifold adhesion processes on such substrates. With a generic protocol it would be possible to characterise the dependence of many biological and biomimetic adhesion processes on ligand distance and density. In contrast to the very simple procedure of binding thiolated peptides or thiol-carrying proteins to gold dots, a general protocol for binding arbitrary proteins to the gold nanopattern includes several steps. Within the scope of this thesis, we attempted to covalently bind streptavidin to the gold dots, which opens new avenues for coupling biotinylated molecules in a second reaction step. Since many proteins have been biochemically modified to carry a biotin group, a successful coupling of streptavidin to the nanopattern implies a large variety of possible nanopattern functionalisations.

The procedure of functionalising gold dots with streptavidin used in this thesis is based on standard carbodiimide coupling chemistry. Firstly, a thiolated linker molecule, which carries a carboxy group at its second end, is bound to the gold dots via its thiol group. Secondly, the carboxy group is activated by a carbodiimide derivative (EDC) and transferred into an active ester (by NHS). The active ester in turn can bind to the protein via an amide bond under release of NHS. A detailed description of the coupling chemistry is found in the diploma thesis of Irina Sliszkaia (Slizskaia, 2005).

The successful streptavidin immobilisation was verified by employing a fluorescently labelled streptavidin (FITC-streptavidin, Sigma, Germany) and fluorescence microscopy revealed an enhanced fluorescence signal from the nanopatterned part of the substrate. In order to prove the binding activity of surface-coupled streptavidin, fluorescent Atto532-Biotin (Attotec, Germany) was applied to a streptavidin functionalised nanopattern. Fluorescence microscopy images clearly showed an enhanced fluorescence signal for the streptavidin functionalised, nanopatterned part of the substrates compared to the nanopattern-free part (see figure 3.9). This indicates that the streptavidin is only bound to the nanopatterned part of the sample and most importantly, that the streptavidin remains in a functional state after coupling it to the gold dots.

This strategy of protein coupling can be used to bind any other protein to the gold dots, either by direct carbodiimde coupling or alternatively, by binding the protein onto a streptavidin functionalised substrate via a biotin group.

In the course of the experiments it turned out, that this kind of surface functionalisation probably changes the passivation properties of the PEG layer. Especially the addition of the alkane thiol linker is a critical point. Results studying the adhesion of vesicles on mPEG2000-urea passivated nanopatterns indicated that either structural rearrangements of the PEG layer are induced by the linker or that the linker molecule is directly incorporated into the passivation layer. For sensitive adhesion systems, such as giant vesicles, these changes in the passivation layer completely destroyed its ability to prevent nonspecific adhesion (Slizskaia, 2005).

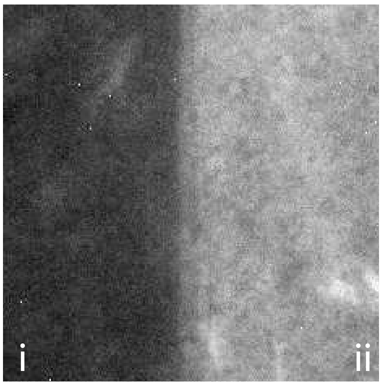

Figure 3.9: Fluorescence image of the dipping edge. (i) Non-nanopatterned, passivated region of the sample. (ii) Streptavidin functionalised, nanopatterned region after binding fluorescently labelled biotin.

3.4 Gold Microstructures

Micropatterns of proteins on glass nowadays attract lots of interest and are predominantly prepared by either of two common methods: direct microcontact printing or the indirect binding of proteins to a secondary material, which coats the substrate in the desired pattern. In the study presented here we have chosen the second approach because in our lab gold micropatterns can easily be produced and the thiolated RGD sequence can be used to functionalise the gold structure for cell adhesion.

The preparation of gold microstructures involves two major steps: The fabrication of a chromium mask and the transfer of the mask structure onto a glass slide.

For the preparation of the chromium mask, a clean glass slide is first coated with a thin chromium layer. On top, a layer of photoresist is applied. This photoresist is chemically modified by UV light, using a special photo-mask writer which applies the digital structure information to the coated substrate. After photoresist development, a chromium etch solution excavates the micropattern structure, serving as the negative of the later gold structure.

In a second step, the gold structures are prepared on a glass slide. Hence, clean, photoresist coated glass slides are coupled together with the chromium mask before they are exposed to UV light. After UV irradiation the resist is developed and the chemical contrast of the microstructure is imprinted into the photoresist layer. Subsequently, the samples are sputtered with titanium and gold, where a titanium layer of approx. 5 nm is necessary to mediate the attachment of the gold layer to the glass. A subsequent lift-off procedure, for example sonication of the samples in acetone, removes the surplus gold, titanium and photoresist between the desired gold pattern. Interestingly, the gold patterns, in our case small discs, have an elevated rim and are shaped like flat bowls, as shown in figure 3.10. The height of the bowl rim is approximately 80 nm[6].

---

[6] For detailed specifications on the whole preparation see Abel, 2005.

The resolution limit of photolithography is determined by the wavelength used to irradiate the photoresist. Therefore the structures cannot be prepared with a resolution better than a few hundred nanometres. The substrates used in this thesis consist of 50 nm thick gold discs with a diameter of 9 µm and an edge-to-edge distance of 20 µm. The functionalisation of the gold micropattern for cell adhesion follows the same procedures as described in the previous sections.

The microstructured samples used for the experiments presented in section 8.5 of this thesis were kindly provided by Marcus Abel (Uni Heidelberg).

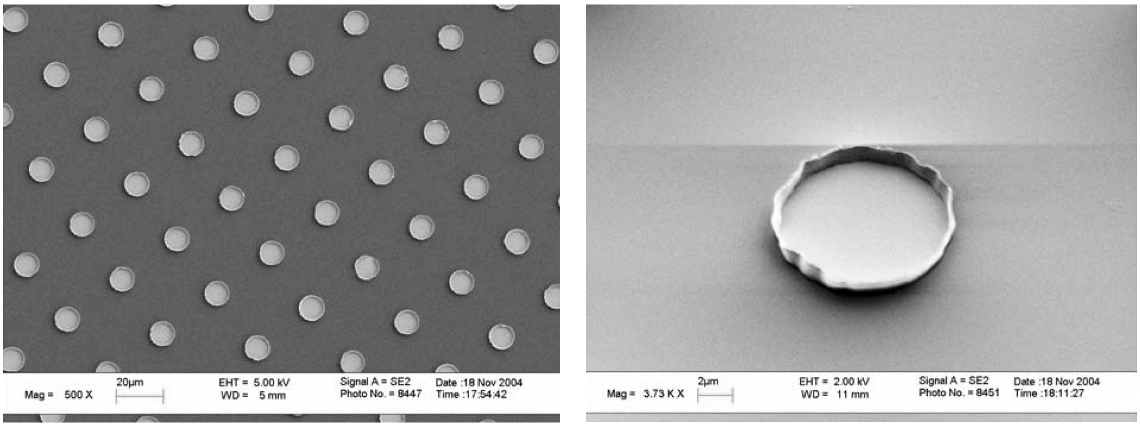

(a) (b)

Figure 3.10: SEM images of gold discs on glass substrates. (a) Top view. (b) Enlarged side view of a single "micro-bowl" (from Abel, 2005).

3.5 Discussion of the Surface Preparation Strategies

The possibility to prepare micro- and nanopatterned, biofunctionalised surfaces allows to study a large variety of biological processes, which were not within reach before. In particular, cell adhesive nanopatterns allow to grab single cellular adhesion receptors, to fix their position in the cell membrane and to study the effects of such a "receptor patterning" on cellular processes.

The nanopatterning of substrates by means of micelle nanolithography is a successful method which allows large surface areas to be covered with a quasi-hexagonal pattern of gold dots. Due to the small gold dot diameter of around 8 nm or less, it is taken for granted that only one integrin molecule can bind per functionalised gold dot, because the diameter of the integrin head domain is approximately 9 nm (Xiong et al., 2001). Thus, with RGD functionalised nanopatterns a precise length scale for the minimal distance between integrins in the cell membrane can be predefined.

A critical step towards the usage of nanopatterns for biological purposes is its functionalisation. This includes on the one hand a passivation of the inter-particle region against nonspecific adhesion, on the other hand a specific functionalisation of the gold dots. In this thesis, RGD peptides and streptavidin were used to functionalise the gold dots for integrin and biotin binding, respectively.

For passivating glass substrates, two strategies have been followed. The commonly used passivation in our group is the covalent coupling of mPEG2000-urea to glass slides. This is a rather time-consuming method and it includes several difficult preparation steps. In contrast, a PLL-g-PEG passivation is an easy-to-handle process and the properties of the passivation layer have been characterised very well in recent works by the Textor group (ETH Zürich). The passivation of nanopatterns with PLL-g-PEG has been established in the scope of this thesis.

When gold nanopatterns are passivated with PLL-g-PEG, it was first expected that also the gold dots would be fully covered. PLL-g-PEG is known to adsorb nonspecifically to the gold, though with relatively small affinity compared to glass (personal information from J. Vörös, ETH Zürich). However, the RGD peptide, as used for gold dot functionalisation, is very small and expected to penetrate the PLL-g-PEG layer to bind to the gold dots. Our cell experiments indeed show that cells can adhere to such PLL-g-PEG passivated, RGD functionalised substrates (see section 6.3).

4 Methods to Characterise Adhesion

Adhesion can be addressed from very different perspectives. On the one hand, optical, interferometric setups give information on the gap between adhering materials and the substrate. Such experiments, for example, allow to draw conclusions on the adhesion dynamics of soft matter systems such as vesicles or cells. On the other hand, adhesion can be quantified by measuring adhesion forces.

In the first part of this chapter, an introduction to an optical interferometric technique, RICM, is given. The subsequent sections describe the two approaches which were used to characterise the cell adhesion strength in this thesis: magnetic tweezers and atomic force microscopy.

4.1 Reflection Interference Contrast Microscopy (RICM)

Adhesion studies based on optical methods require a high sensitivity of the particular technique for processes happening close-by the surface. Commonly used techniques fulfilling these requirements are reflection interference contrast microscopy (RICM) and total internal reflection fluorescence microscopy (TIRF). Whereas TIRF can only study fluorescently labelled objects, the image contrast of RICM results from the interference of light which is reflected at several refractive index boundaries. Thus, RICM allows to study adhesion without any necessity for modifications such as the incorporation of fluorescent probes.

4.1.1 Setup and Image Formation

Interference reflection microscopy had its prime time in the 1970s, when it was extensively used by biologists before the fluorescent labelling of cellular proteins became a standard technique in biology (Gingell and Todd, 1979). With the development of genetic modification techniques and increased output from fluorescence microscopy, interference microscopy was buried in oblivion for some time until it aroused interest again in the 1990s for physical studies of soft matter. The application of interference microscopy for quantitative experiments was made possible by some modifications in the optical setup by Rädler and Sackmann (1992), which they introduced in *reflection interference contrast microscopy* (RICM). In contrast to previous setups, they used monochromatic, polarised light which not only enhanced the image contrast, but also allowed a quantitative interpretation of the acquired interferograms (Rädler and Sackmann, 1992). A prominent example for the power of RICM is the possibility to determine the vertical position of micrometre sized colloidal beads above a substrate with an accuracy of ±3 nm (Schilling et al., 2004).

In our lab we installed the optical setup for RICM on a standard inverted microscope (Axiovert 200, Zeiss). A monochromatic illumination is achieved by a mercury lamp

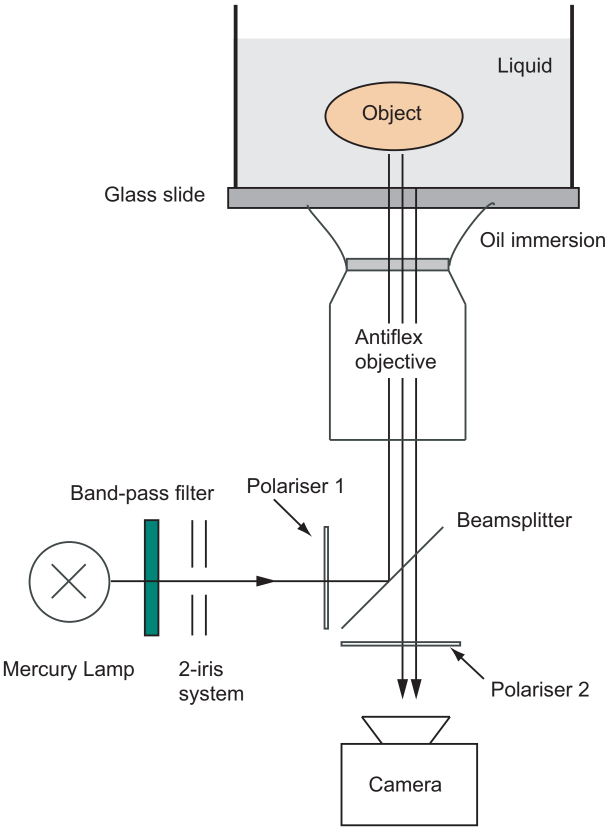

Figure 4.1: Sketch of the RICM setup.

(HBO 103, Osram) in combination with two band-pass filters ($\lambda_1 = 546.1$ nm, $\lambda_2 = 436$ nm). With a two-iris system, a small region of the emission sphere is cut out to approximate a parallel illumination. The Antiflex technique (Ploem, 1975) enhances the contrast of the interference pattern by using cross-polarisers and a so-called "Antiflex objective", an oil immersion objective with a $\lambda/4$ plate in front of its final lens (Plan Neofluar, 63×, NA=1.25, Zeiss). This trick ensures that only the light that has passed the objective twice reaches the camera. Since the objective is an oil immersion objective and the refractive index of the immersion oil is comparable to that of the glass sample and the objective lens, the glass-buffer interface is the first reflective interface that the light encounters above the objective. The second reflective plane is the interface between object and buffer. The interference between the reflected light of these two (or sometimes several more) interfaces leads to an intensity pattern, which ideally allows to draw conclusions on the contour of the studied object. The interferograms were recorded with a 12 bit CCD camera (Camera: ORCA-ER, Hamamatsu, Japan; Software: SimplePCI, Compix Imaging Systems, PA.). An overview of the complete RICM setup is given in figure 4.1.

In the simplest case, reflection takes place exclusively at the two interfaces glass/liquid and liquid/object. The interference pattern for objects in the (x,y) plane is then described by

$$I(x,y) = I_1 + I_2 + 2\sqrt{I_1 I_2}\cos(\frac{4\pi n}{\lambda}h(x,y) + \Delta), \tag{4.1}$$

where I_1 and I_2 are the intensities of the two interfering light beams, n is the refractive index of the liquid ($n \approx 1.33$), λ is the wavelength of the illuminating light and $h(x, y)$ is the vertical position of the object's contour above the glass slide. For an object with $n_{\text{object}} > n_{\text{buffer}}$ the phase difference Δ equals π. If then $h = 0$, the cosine in (4.1) becomes -1 and thus areas of small h appear as dark zones in the interference pattern. From the cosine in the interference function (4.1) it is obvious, that uncertainties remain when $h(x, y)$ is to be derived from an interference pattern, since the pattern is repeated periodically every $\Delta h = \lambda/2n$. To a certain extent, one can evade such ambiguities by introducing a second wavelength (Schilling et al., 2004). In figure 4.2 the calculated intensities for an object's contour between 0 and 900 nm above the substrate for $\lambda_1 = 546.1$ nm (green) and $\lambda_2 = 436$ nm (blue) are plotted. For measurements in water, the two-wavelength system exhibits a common periodicity of 816 nm, compared to 205 nm if only green light was used. The situation presented in figure 4.2 shows, that by comparing the intensity signals of the two wavelengths it is indeed possible to identify an intensity pattern in one colour with an unambiguous height information by comparing it with the intensity of the second colour. The periodicity of the system can in principle be increased even more by using a third wavelength, for example the yellow emission line of mercury.

In contrast to the double-wavelength RICM introduced by Schilling et al. (2004), where it was possible to simultaneously follow the RICM signal of two wavelengths, in our setup a manual wavelength switch was introduced. Therefore, with our two-wavelength system only stable processes with a lifetime larger than 10 seconds can be investigated.

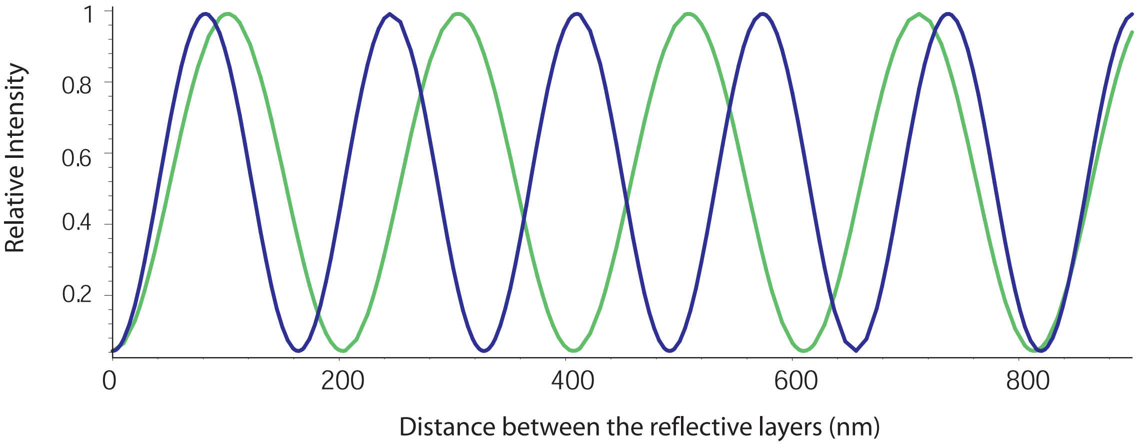

Figure 4.2: Plot of the intensities obtained with RICM for different distances between the glass surface and a reflective object, calculated from equation 4.1. Green line: λ_1=546 nm. Blue line: λ_2=436 nm.

4.1.2 Applications of RICM

Some applications of RICM in soft matter studies are shown in figure 4.3. On the one hand, RICM is, as already mentioned, known for its precision in detecting distances between colloidal objects and substrates. This can be used for measuring the thickness of polymer layers by placing colloidal beads on their top. In this way, a characterisation of the swelling behaviour and the viscoelastic properties of polymer layers is possible (Albersdörfer and

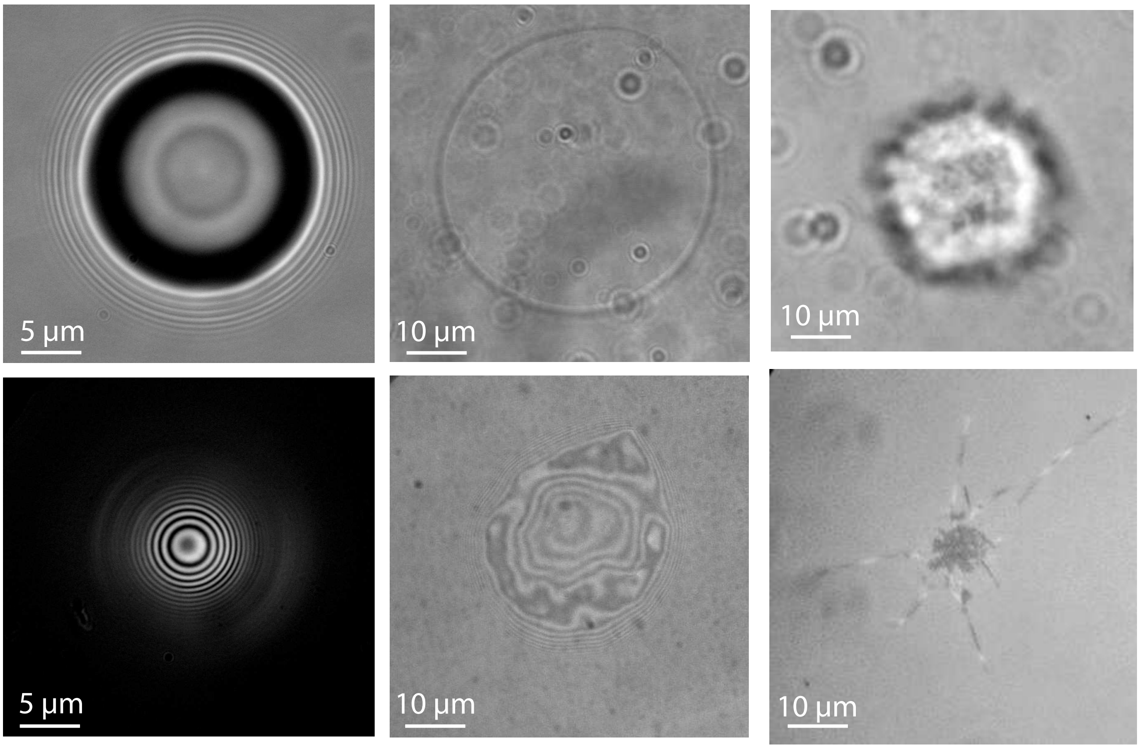

(a) (b) (c)

Figure 4.3: Examples of RICM images (bottom) in comparison with bright-field images (top). (a) A polystyrene bead. Bright-field microscopy reveals the typical diffraction pattern, RICM shows Newton's rings. (b) A vesicle hovering above a substrate. The leopard texture in the RICM image reflects the inhomogeneous distance between surface and membrane. (c) A cell in its initial adhesion processes, where RICM monitors the cell adhesion area and some microspikes.

Sackmann, 1999; Picart et al., 2004). An example showing the appearance of a colloidal bead in bright-field microscopy and RICM is given in figure 4.3 a.

Figure 4.3 b shows a giant vesicle, both in bright-field microscopy and RICM. The leopard textured RICM image is due to the strong fluctuations of the vesicle membrane and can be analysed in terms of adhesion kinetics and strength. With such a setup, specific interactions between a vesicle membrane and a functionalised substrate could be investigated and have lead to a first insight into the adhesion properties of this biomimetic cell model (Smith et al., 2006a; Smith et al., 2006b; Gönnenwein et al., 2003).

For cell adhesion studies, RICM is nowadays rarely used. However, there are studies showing that RICM can efficiently lead to quantitative information in cell studies, for example by following the shear flow induced deformations of the cell cortex (Simson et al., 1998). RICM has similarly turned out to be a useful tool for initial cell adhesion studies. As shown in figure 4.3 c, RICM reveals small microspikes and a tiny adhesion area below the cell body, an effect which is completely obscured in bright-field microscopy. A further analysis of such microspikes is given in chapter 6.

4.2 Magnetic Tweezers

A first usage of magnetic particles for the detection of intracellular processes was described in the 1980s, where cell-internalised Fe_2O_3 particles were manipulated by external magnetic fields and provided first rheological data of the cell interior (Valberg and Albertini, 1985). The principle of magnetic tweezers experiments remained the same over the years: magnetic particles are bound to or incorporated into the system of interest and manipulated by external fields, while following their motion. Most magnetic tweezers studies have been performed to characterise viscoelastic material properties (Bausch et al., 1998) and single molecules (Gosse and Croquette, 2002). In contrast to these studies, the setup presented here allows to characterise cell adhesion forces. It was built in cooperation with Nadine Walter during her diploma thesis (Walter, 2005).

4.2.1 Experimental Setup

The magnetic tweezers device used for cell adhesion experiments exerts a vertical force on a paramagnetic bead which is bound to a cell. The basic idea of our setup is derived from a system used for adhesion studies on vesicles by the group of Erich Sackmann at the TU München (Smith et al., 2006a; Gönnenwein, 2003). We modified several aspects of this setup to meet the requirements of our cell adhesion studies.

The most important part of the magnetic tweezers are two identical electromagnets which are facing each other with opposite magnetic poles. The electromagnets are made of transformer cores of 100x27x27 mm^3 and the shape of the pole tips was modified to produce large magnetic field gradients. The cores are wrapped with approximately 700 windings of 0.8 mm thick copper wire. A crucial parameter for achieving high forces is the distance between the two pole tips and the position of the magnetic particle relative to them, since the magnetic field decays strongly with increasing distance from the pole tips. To make this distance as small as possible, the position of the electromagnets and the sample holder were adjusted by micrometre screws. The shape of the sample holder and the pole tips were adapted to allow both RICM and bright-field illumination. At the position of the sample, magnetic fields of 380 mT and gradients of 90 T/m can be reached, as has been measured with a Hall sensor.

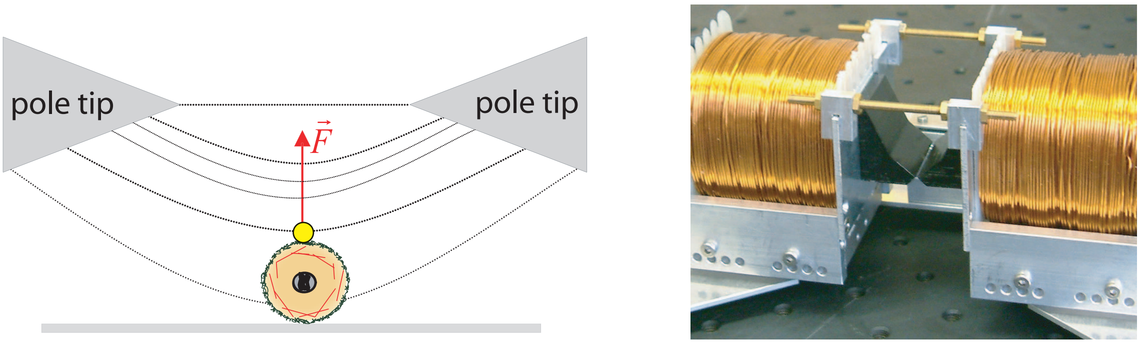

(a) (b)

Figure 4.4: (a) Sketch of the magnetic tweezers setup. (b) Photograph showing the arrangement of the electromagnets and the shape of the pole tips.

To apply forces onto cells, epoxy-terminated magnetic beads (Dynal, Norway) were bound to the cell membrane. The forces applied to the magnetic beads were modulated by the current applied to the electromagnets. The experiments were operated using a custom-written LabView program (National Instruments Corp., TX), which controls the applied force and triggers image recording with a high-resolution camera (Digital CCD Camera ORCA-ER, Hamamatsu Photonics, Germany). Both RICM and bright-field microscopy can be used to follow cell detachment. The experiments were analysed by correlating the time of cell detachment with the applied force. A sketch and a photograph of the used magnetic tweezers system are shown in figure 4.4.

4.2.2 Calibration

To calibrate the forces exerted by the magnetic tweezers, the velocity v of a magnetic bead of radius r was monitored while it was pulled through a fluid of viscosity η by a magnetic force. When the velocity of the bead is constant, the friction force, which is described by Stokes drag formula, equals the force exerted onto the bead. The calibration was performed in glycerol (99,5 % from GEBRU, Germany) both at 30 °C and 20 °C in order to vary the viscosity of the glycerol and thus to achieve a calibration over the whole force regime.

The velocity of the magnetic beads is determined by observing their vertical motion in bright-field microscopy and comparing the changing diffraction pattern to a series of reference images, as shown in figure 4.5 a (Gosse and Croquette, 2002). The reference images of a bead were taken by changing the distance between the objective and the focal plane manually in steps of 1 µm, which corresponds to the situation of a vertically moving bead and a constant objective position. The correlation of the images was performed with

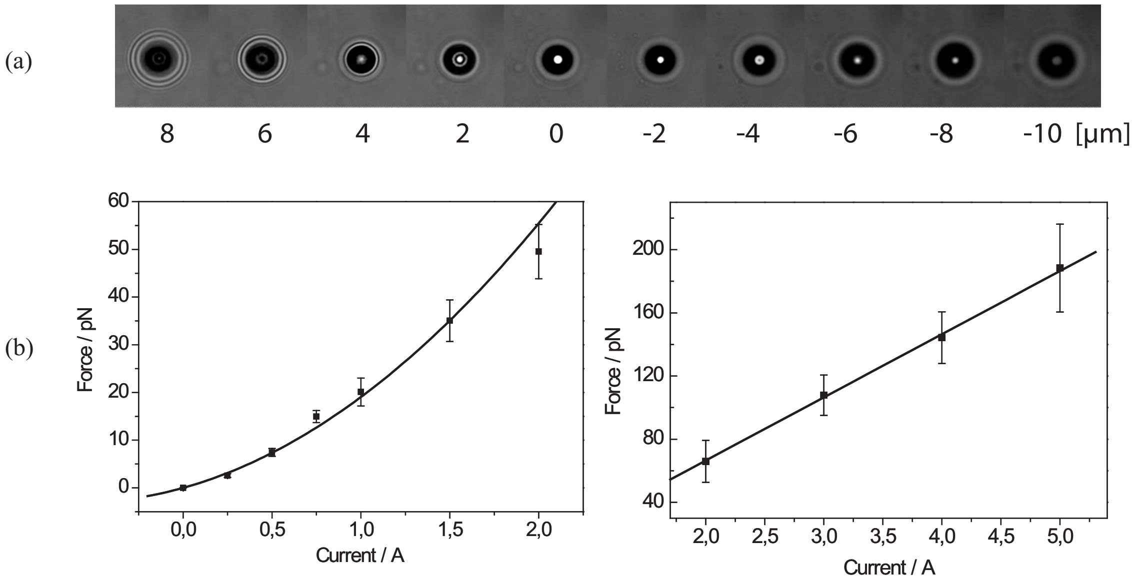

Figure 4.5: Calibration of the Magnetic Tweezers. (a) Diffraction patterns from a 4.5 µm magnetic particle. The numbers below the images denote the distance of the objective from the focal plane in µm. (b) Forces applied to the 4.5 µm magnetic particle by the magnetic tweezers for the two different calibration regimes of non-saturated ($I \leq 2$ A) and saturated ($I > 2$ A) bead magnetic moment.

a custom written IDL program (IDL Research Systems). The result of this calibration is shown in figure 4.5 b. Each data point of the calibration curve was determined from at least five experiments. The relation between the current applied at the electromagnets and the force exerted onto a bead is nonlinear for currents lower than 2 A, since the magnetic moment of the paramagnetic beads is then not saturated. For higher currents, there is a linear dependence between applied current and exerted forces, which is a sign for a saturation of the bead's magnetic moment. To avoid an overheating of the electromagnet coils, the applied currents had to be restricted. Therefore the maximum force exerted by the tweezers onto a 4.5 µm magnetic bead (Dynal, Norway) was 200 pN. The applied forces are constant over a vertical distance of at least 30 µm and laterally over the accessible sample area of about 80 µm x 60 µm.

4.3 Atomic Force Microscopy (AFM)

Recording surface topographies has attracted special interest after the invention of the topografiner, which was the first device for monitoring height profiles at the micrometre level (Young et al., 1972). The step towards studying surface profiles at the atomic level was made with the invention of the scanning tunneling microscope (STM). There, the tunneling current between a sharp metallic tip and a sample can be measured and conclusions on the atomic structure of the scanned material can be drawn (Binnig et al., 1982). Atomic force microscopy (AFM; also: scanning force microscopy, SFM) was originally invented for depicting surfaces of non-conductive materials by following the deformation of a micrometre sized cantilever while scanning it over a sample[1] (Binnig et al., 1986). However, the cantilever can likewise be employed as a force sensor. The working principle of an AFM, the necessary calibrations prior to force experiments as well as an introduction to its applications in cell experiments are presented in this chapter.

4.3.1 Design of an AFM

The basic setup of an AFM seems very simple at first glance: a micrometre sized, deformable cantilever is scanned over a surface while its bending is simultaneously recorded. This is possible by reflecting a laser beam at the cantilever rear and recording the position of the reflected signal by a position-sensitive detector (see figure 4.6 a). In the AFM used in the experiments of this thesis (Nanowizard, JPK Instruments), the high precision of the measurement is maintained by three closed-loop controlled piezo elements in the AFM head, one for each direction in space (piezo ranges: x,y: 100 µm; z: 15 µm). Additionally, this AFM has been specially designed for performing live cell experiments. Because cells can have a diameter of several tens of micrometres when they are spread onto substrates, the standard piezo z-range of 15 µm is not sufficient for detaching such cells from a substrate. Therefore, our system is equipped with three further piezo elements of 100 µm z-range, which move the sample towards or away from the cantilever, instead of moving the AFM head (CellHesion, JPK Instruments). In order to optically visualise the studied objects, the AFM system is installed onto an inverted microscope (Axiovert 200, Zeiss), allowing a simultaneous operation of AFM and standard microscopy, such as phase contrast and fluorescence microscopy. Additionally, a heated fluid cell (BioCell, JPK Instruments)

---

[1] For a detailed introduction to scanning probe microscopy see Meyer et al., 2004.

was employed, so that the cell experiments were performed unter standard cell culture conditions. This was a great advantage, especially since the binding kinetics of cells is strongly temperature dependent.

As is sketched in figure 4.6, there are two common purposes of the AFM. The first is to monitor the surface topography by laterally scanning the tip of a cantilever over the surface. For such a scanning experiment, two operation modes are possible: Contact mode and intermittent contact mode. In contact mode, the cantilever is approached to the sample and the deflection of the cantilever is maintained constant by adapting the piezo extension during the scanning process. The information on the surface profile is then stored in the vertical position variations of the piezo extension. In intermittent contact mode, the cantilever is excited to oscillate close to the cantilever resonance frequency and the amplitude of the cantilever oscillations is maintained constant by adapting the piezo extension during the scanning process. Figure 4.7 a shows a topography image from an intermittent contact scan of a nanostructured sample, where the height information is encoded in the colour distribution. The plot in figure 4.7 b shows the topographical information extracted from the black line in the scan. The resolution of AFM scans critically depends on the sharpness of the cantilever tip, since the AFM image represents the convolution of the surface geometry and the tip geometry.

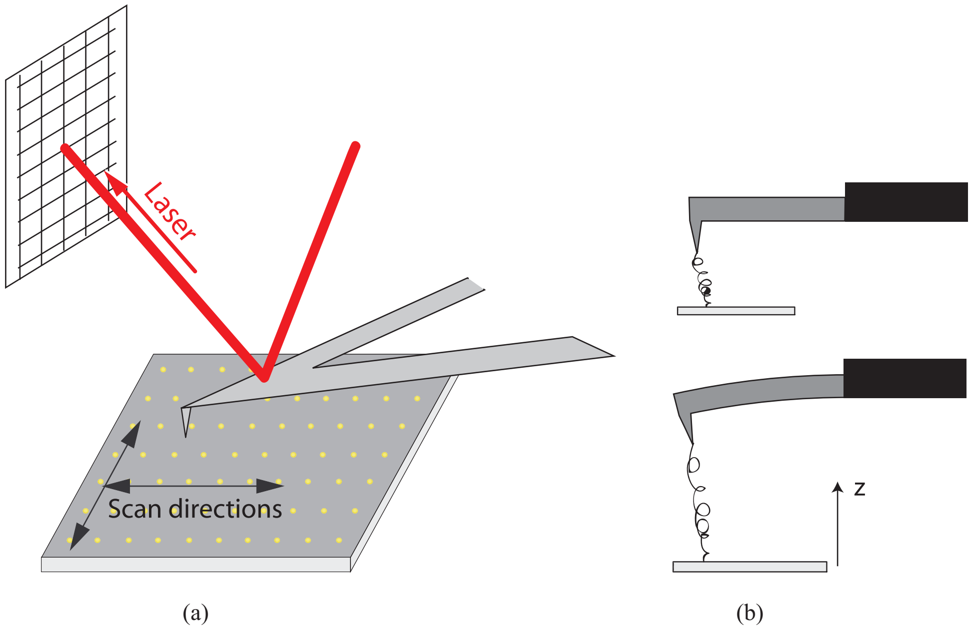

(a) (b)

Figure 4.6: Typical examples for AFM experiments. (a) Scanning experiment for monitoring surface topologies. (b) Force response of a protein or polymer upon tension, measured by the deflection of the cantilever.

The second important purpose of an AFM is the usage of the cantilever as a force sensor. This is possible, since cantilevers can be regarded as deformable, elastic beams and can be assigned a certain spring constant. A typical experiment studying the force response of a polymer under tension is sketched in figure 4.6 b, where the cantilever is deflected in -z direction due to the elastic resistance of the polymer. The force resolution of the setup depends on the spring constant of the cantilever: The softer the cantilever, the smaller are

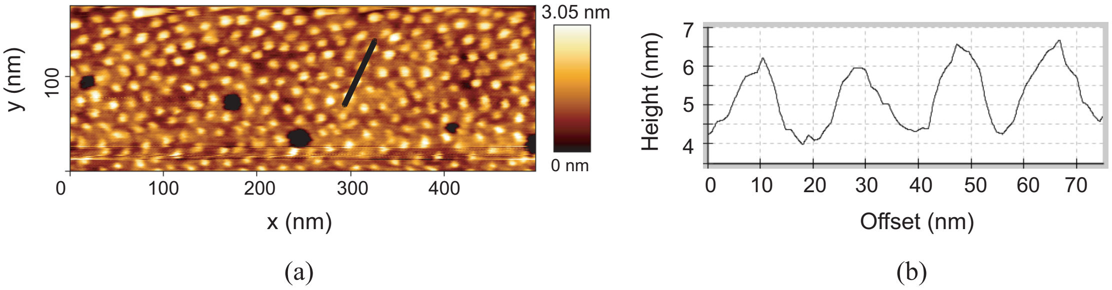

(a) (b)

Figure 4.7: (a) AFM scan of a nanopattern taken in intermittent contact mode. The circular black holes are holes in the glass surface. (b) Topographical information extracted from the black line shown in (a).

the forces which can be measured. Although very soft cantilevers can be manufactured nowadays, a softer cantilever suffers from an increased sensitivity to thermal and acoustical noise. The lower limit of resolution is set by the magnitude of thermal noise and the force constant of the cantilever. In a standard experiment, the cantilever is pressed onto the substrate to a certain force set-point before it is retracted to its original position. The deformation of the cantilever, and thus the applied force, is recorded both in the approach and retraction phase.

A typical force curve is shown in figure 4.8. The solid black curve represents the approach of a cantilever to a glass surface. As soon as the gradient of the attractive forces between

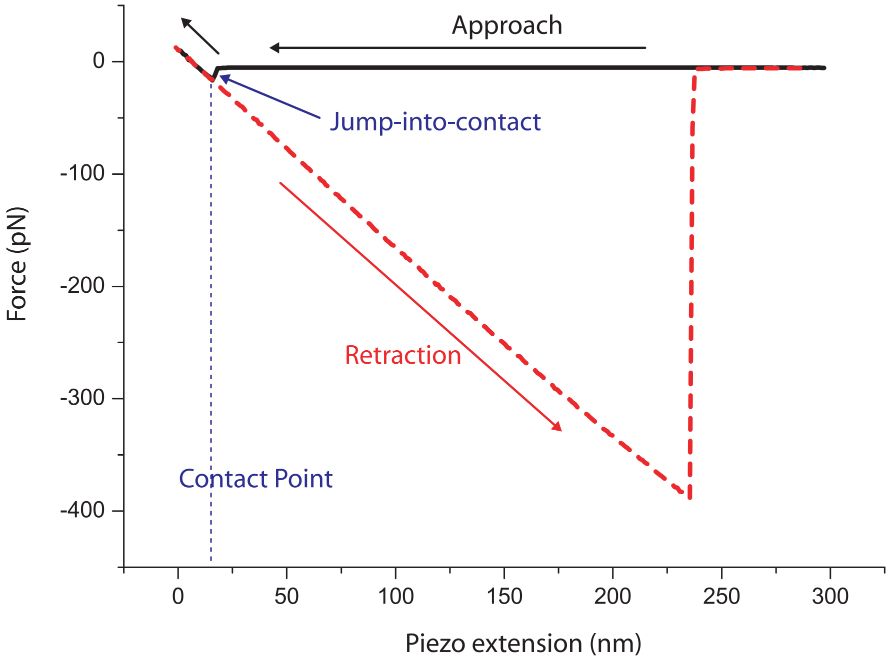

Figure 4.8: Force-extension curve for a cantilever which is strongly interacting with a glass surface. In the approach curve, the position where the cantilever jumps into contact with the surface is marked. The retraction curve shows the deflection of the adhering elastic cantilever during piezo retraction. This linear force-extension regime is followed by a force jump, which is due to the detachment of the cantilever from the surface.

cantilever and glass becomes larger than the spring constant of the cantilever, the cantilever jumps into contact. During pressing the cantilever onto the substrate, the cantilever is bent in +z direction, recorded as a positive force signal. When the cantilever is retracted from the substrate (dashed red curve), it stays trapped in the minimum of the substrate-cantilever interaction potential until the elastic energy of the cantilever deformation equals the energy which is necessary for the separation of the cantilever and the surface. As long as the piezo continuously retracts the cantilever chip, but the cantilever tip is still sticking to the substrate, the cantilever is bent in -z direction, represented by a negative sign in the force signal (see also the image at the bottom of 4.6 b). The step in the force curve at around 230 nm piezo extension shows the sudden release of the cantilever from the glass surface.

The usage of AFM for force measurements has proven to be widely applicable. Studies range from characterising the strength of covalent and biological bonds (Grandbois et al., 1999; Florin et al., 1994) to protein unfolding (Rief et al., 1997) and adhesion properties of live cells (Benoit et al., 2000).

4.3.2 Cantilever Calibration and Sensitivity Analysis

When the cantilever is deflected, the position-sensitive detector can resolve the position of the reflected laser with high precision. However, this signal alone does not give any information on the force acting at the cantilever. Instead, two parameters have to be calibrated first: The force constant and the sensitivity.

Although approximate values for cantilever force constants are given by the manufacturer, they should be recalibrated, since variations from one lot to the other of up to 50% are common. Whereas length and width of the cantilever are defined photolithographically with sub-micrometre precision, variations in the cantilever thickness t are possible. This has strong impact on the force constant k, since $k \propto t^3$ and variations in t are regarded to be the major origin of variations in the force constant (Cleveland et al., 1993).

Soft cantilevers can easily be calibrated by the thermal noise method, where the power spectrum of thermally induced fluctuations of the cantilever is analysed. This approach is legitimated because the cantilever can be regarded as a simple harmonic oscillator with one degree of freedom for oscillations at room temperature. Then, the cantilever fluctuations are very small (around 3Å) and other modes, such as torsion, are negligible due to their large force constants (Hutter and Bechhofer, 1994).

The AFM analysis tool delivered with our AFM software is only capable of analysing power spectra for frequencies up to 100 kHz and can thus not be applied to stiff cantilevers with larger resonance frequencies. To calibrate such cantilevers, the resonance frequency ω_{real} was measured with a separate tool in the AFM software. Then reference values for k and ω given by the manufacturer were used to relate ω_{real} to the true force constant k_{real} of the particular cantilever via $k_{real} \propto \omega_{real}^3$ (Cleveland et al., 1993).

Additionally, prior to each single experiment the sensitivity of a cantilever is determined. The sensitivity is a measure of how the laser detector signal changes (in V) for a certain cantilever deflection (in nm). This value strongly depends on the laser position at the cantilever and the position of support, onto which a cantilever is pressed (see next section).

With all the information on sensitivity s and force constant k at hand, the forces acting on the cantilever can be deduced from the detector signal U by

$$F[\mathrm{N}] = U[\mathrm{V}]\, s[\frac{\mathrm{nm}}{\mathrm{V}}]\, k[\frac{\mathrm{N}}{\mathrm{m}}].$$

4.3.3 Supported Cantilevers

When detaching a cell from a substrate, the cell is often not situated at the very end of the cantilever. Therefore the effectively bent part of the cantilever is decreased and both its force constant and sensitivity have to be recalculated according to the situation in the particular experiment. In the following, an equation for relating the position of support to the cantilever sensitivity and force constant is derived.

Figure 4.9 shows a sketch for such an experimental situation: The cantilever is supported at some arbitrary point between cantilever chip and its free end, thus it is only bent over the length between the point of support at z_s and the cantilever suspension at the chip. The remaining part of the cantilever stays linear and is not bent. Here, only deflections in the x-z-plane are considered, since torsion is neglected for the experiments performed. An additional condition for the following analysis is $z_{Laser} < z_s$, which was true for all our experiments performed.

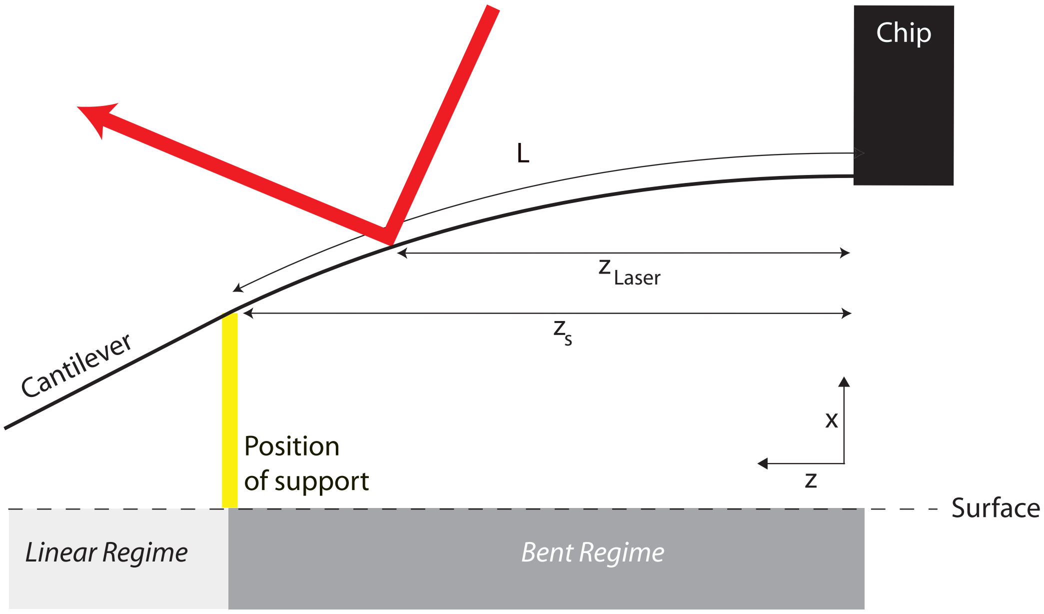

Figure 4.9: Sketch of a cantilever which adheres at z_s and bends in response to retracting the chip from the surface. The position of support, z_s, lies between the chip and the free end of the cantilever.

From elasticity theory (Landau, 1991) the shape of the cantilever in its bent regime is described as

$$x(z) = \frac{f}{6EI} z^2 (3L - z) \quad \text{for } z \leq z_s \tag{4.2}$$

with f the bending force and EI the bending resistance (E: elastic modulus, I: moment of inertia). z is a point along the cantilever calculated as distance from the suspension, and L is the effective length of the cantilever as defined by the support.

The cantilever shape for the linear regime between the position of support and the cantilever's front end is

$$\bar{x}(z) \quad = \quad x'(z_s)z + x(z_s) \ \text{ for } z > z_s, \tag{4.3}$$

where $x'(z_s) = \frac{f}{2EI} z_s(2L - z_s)$.

As shown in figure 4.9, the laser spot is reflected at z_{Laser}. The position of the laser spot at the detector critically depends on the slope of the tangent to the cantilever in z_{Laser},

$$x'(z_{Laser}) \quad = \quad 3Az_{Laser}(2L - z_{Laser}) \text{ with } A := \frac{f}{6EI}. \tag{4.4}$$

According to its definition in the previous section, the sensitivity s relates the bending of the cantilever at its support, $x(L)$, to the signal recorded by the laser detector. x at position L is according to (4.2)

$$x(L) = 2AL^3, \tag{4.5}$$

provided that the deflection is small ($z_s \approx L$).

Thus the sensitivity becomes

$$s \propto \frac{x(L)}{x'(z_{Laser})} = \frac{2}{3} L^3 \frac{1}{z_{Laser}(2L - z_{Laser})}. \tag{4.6}$$

If the sensitivity s_0 of the cantilever is experimentally determined for a position of support L_0, the sensitivity s for a different position of support L is easily calculated with

$$\frac{s_0}{s} = \frac{L_0^3}{L^3} \frac{2L - z_{Laser}}{2L_0 - z_{Laser}}. \tag{4.7}$$

The validity of this relation was experimentally verified by measuring the sensitivities at constant z_{Laser} but variable L by pressing a cantilever onto a glass sphere. This sphere was large enough to guarantee no further contact of the cantilever with the substrate, so that the center of the sphere served as single position of support. In the experiment, z_{Laser} and L were determined from an optical image, as shown in figure 4.10 a, the data obtained for the sensitivities at different positions of support are given in figure 4.10 b, which are well-approximated by (4.6).

The calculation to obtain the corrected force constant is easy and follows the argumentation in Landau (1991). For a cantilever of total length L_0, supported in L and having an intrinsic force constant k_0 the corrected force constant is

$$k = k_0 \frac{L_0^3}{L^3}. \tag{4.8}$$

In general, the force constant k_0 is determined prior to any experiments. The cantilever sensitivity s_0 is calibrated at the beginning of each experiment by pressing the cantilever onto a stiff substrate and recording the laser signal. Then, a position of support L_0 denotes the full length of the tipless cantilever, as it was used in the experiments. L is the position where the cell is attached in the experiment. ΔL is defined as distance between the

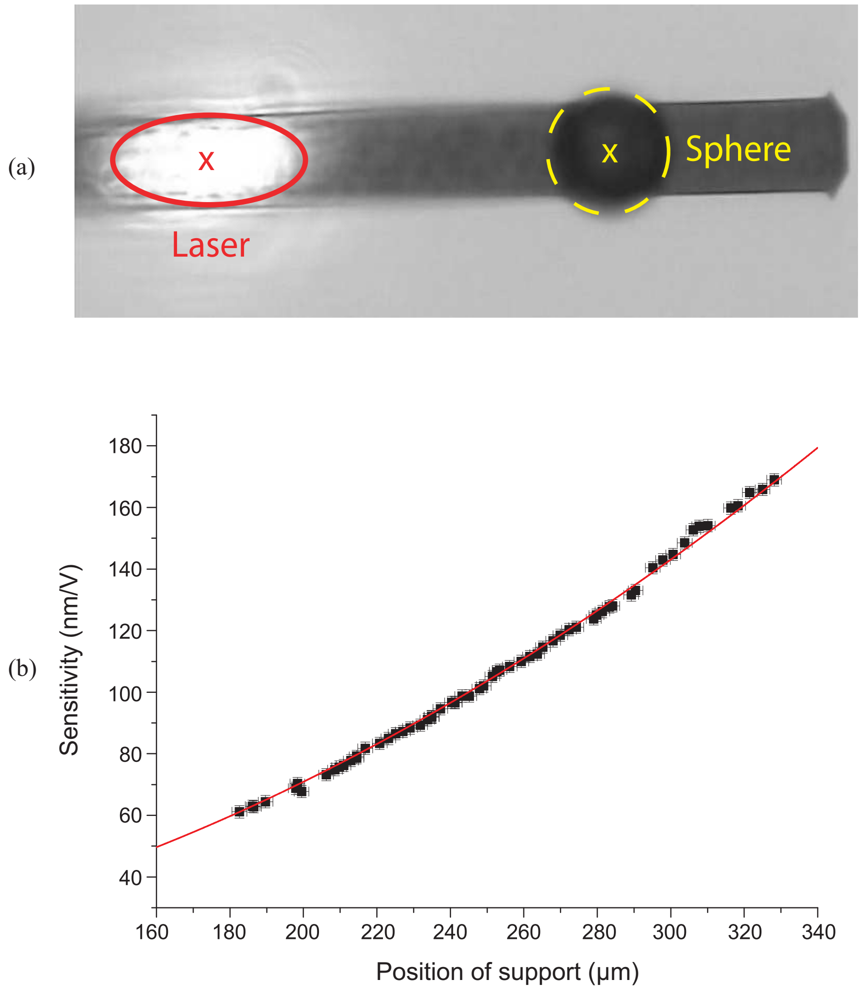

Figure 4.10: Sensitivity calibration. (a) A glass sphere (yellow circle) is used as a position of support for a cantilever. The centre of the yellow circle determines L. The red circle shows the position of the laser spot. The red cross marks the laser spot center, which gives z_{Laser}. (b) The graph shows experimental results for the sensitivity as a function of the position of support. The data are fitted with (4.6).

two positions of support, L_0 and L, so that $L := L_0 - \Delta L$. Paying attention at both the dependencies of force constant and sensitivity on the position of support according to (4.7) and (4.8), the force values F_0 originally obtained by using s_0 and k_0 can be recalculated to receive the calibrated force

$$F = F_0 \frac{s}{s_0} \frac{k}{k_0} = F_0 (1 + \frac{2\Delta L}{2L - z_{Laser}}). \tag{4.9}$$

In conclusion, forces would be strongly underestimated if they were not corrected for different support positions. The introduction of this correction is especially necessary when short cantilevers are used, since then the relative change in effective length $\Delta L / L$ is often particularly large.

4.3.4 Cell Experiments and their Interpretation

In chapters 7 and 8 of this thesis, two different types of live cell AFM experiments are presented. These two types of experiments require different types of cantilevers, different cantilever functionalisations and even the data interpretation has to be adapted to the particular experiment. A short technical overview of both experimental situations is given in the following.

Initial Adhesion

Initial adhesion experiments study the processes for cell-substrate contact times of less than 10 minutes. In such experiments, the maximum interaction force between a cell and a substrate is in the range of a few tens of piconewtons to several nanonewtons and thus relatively weak. To resolve forces down to the piconewton regime, soft, v-shaped cantilevers are used. To obtain even more compliant cantilevers, for some experiments one "leg" of the v-shaped cantilevers was removed by thin tweezers (Benoit, 2002). This modification led to a decrease of the common avalaible force constant of around 60 mN/m to less than 30 mN/m.

For an initial adhesion experiment, a cell is immobilised on a cantilever via concanavalin A (con A), which binds polysaccharides in the cellular glycocalix[2]. Compared to poly-L-lysine or fibronectin functionalisations, con A does not activate cell spreading. Instead, the cell stays in an approximately spherical shape during the whole experiment.

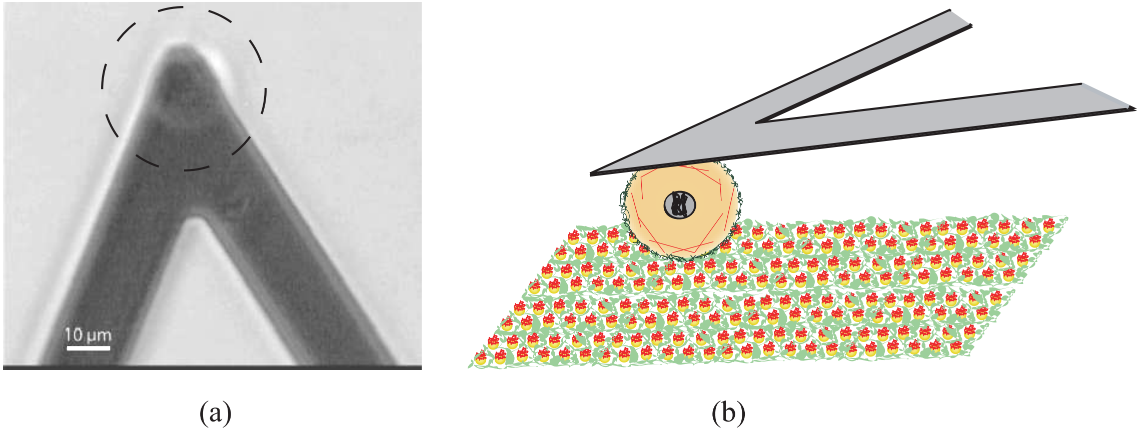

(a) (b)

Figure 4.11: Experimental setup for initial adhesion experiments. (a) Bright-field image of a cell immobilised at a cantilever. The cell is located in the centre of the dashed circle. (b) Sketch of a cell experiment, where the cell is immobilised at a cantilever and brought into contact with the RGD nanopattern.

Figure 4.11 a shows a cell immobilised at the free end of a cantilever and figure 4.11 b sketches the typical setup of a cell experiment. The binding between the cell and the cantilever was achieved by "fishing" the cell from a freshly prepared cell suspension and pushing it slightly onto the substrate with the cantilever. After the cell is immobilised at the cantilever, it is left to relax for about 15 to 30 minutes in the solution without being subject to any external stress. During this time span, proteins damaged during the

---

[2] For a detailed protocol please see the appendix.

preceding trypsin treatment, which was necessary to remove the cells from the cell culture dish, can recover. In the force experiments, the cell is pressed onto a nanopattern or any other kind of substrate for a defined time. This force is held constant during the cell-substrate contact by a feedback mechanism. When the predefined time of cell-substrate contact is over, the cantilever is retracted with a constant velocity, thus also the cell is detached from the surface. During the cantilever retraction, its deflection is continuously monitored, giving information on the forces that are necessary to induce cell detachment. A typical force curve for such an experiment is shown in figure 4.12.

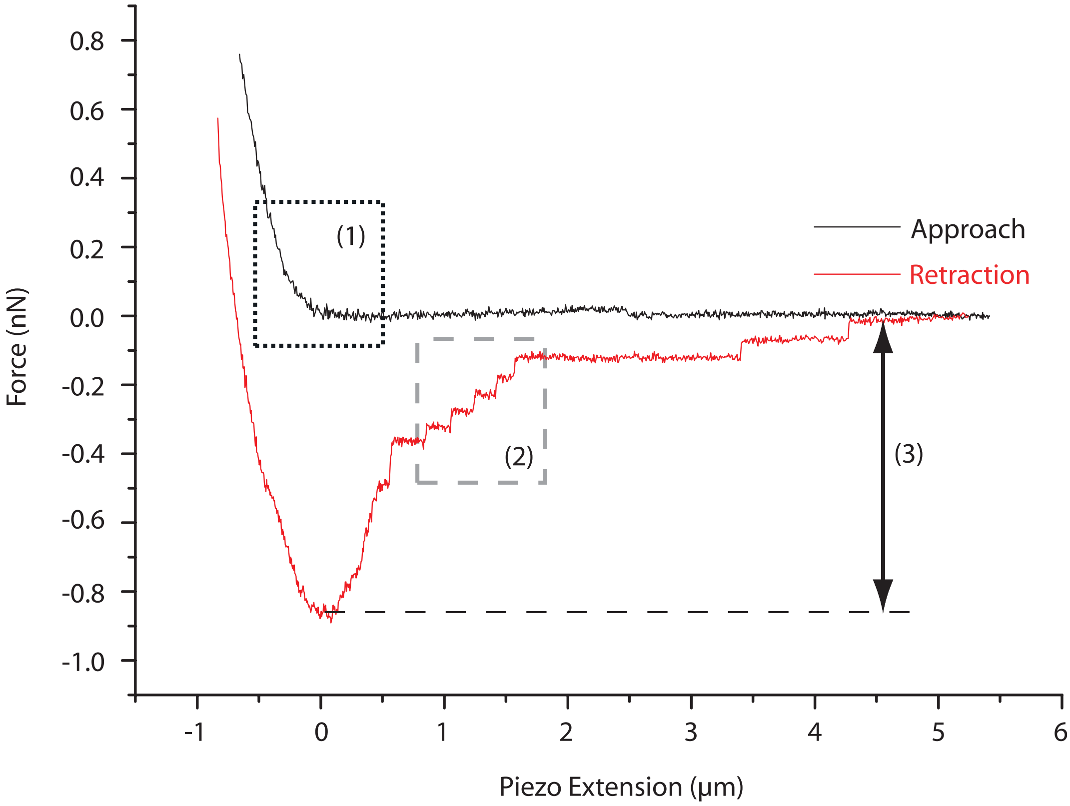

Figure 4.12: Approach curve (black) and retraction curve (red) for a REF 52 wt cell brought into contact with a fibronectin surface. The cell was in contact with the surface for 5 sec. Information on different kinds of cell parameters can be obtained from this curve, for example elastic parameters (1), rupture forces of single bonds (2), and total adhesion forces (3).

In cell experiments, in contrast to the situation when a cantilever is pressed onto a rigid substrate (see figure 4.8), an elastic response of the cell is observed by the nonlinear force signal in region (1). Region (2) shows successive rupture events, which are attributed to the rupture of single bonds. A very important parameter for our study is the maximum adhesion force (3), which coincides with the total force necessary for cell detachment in this kind of experiments. From this force conclusions on the development of adhesion and cluster formation can be drawn (see chapter 7).

Additionally to measuring the forces acting between cells and substrates, also viscoelastic cell properties can be observed. This can be performed in either of two modes: the *constant force mode* and the *constant height mode*. In the constant force mode, a cell is pressed to the substrate and the cantilever position is automatically adapted with a feedback system to keep the force constant. This mode is used for measuring the creep response of a cell. On the contrary, the constant height mode keeps the cantilever position constant and lets the applied stress relax. Data on the viscoelastic creep of cells are given in chapter 7.1.

Long-term Adhesion

In long-term adhesion experiments, where cells are detached from surfaces after they were allowed to spread for several hours, the situation is very different. The cell's connections to the surface are then so strong that the cell has to actively adhere to the cantilever, otherwise it will not be possible to detach it from the substrate. Therefore the cantilevers were coated with fibronectin[3] and to account for the huge forces required for cell detachment, the cantilevers are very stiff with force constants commonly larger than 1 N/m. In the experiment, an appropriate cell was chosen optically and a fibronectin functionalised cantilever was approached to it. The parameters used for the contact between the cantilever and the cell are crucial: Neither too large forces onto the cell should be applied, nor should the cantilever be pressed with its free end onto regions nearby the cell nucleus. In both scenarios the cell is very likely to undergo apoptosis. It turned out during the experiments, that it is reasonable to position the free end of the cantilever right behind the cell, as shown in figure 4.13. This can lead to a successful cell growth onto the cantilever, since the cantilever is tilted to the x-y-plane by an angle of 10° and thus touches the cell slightly from the side.

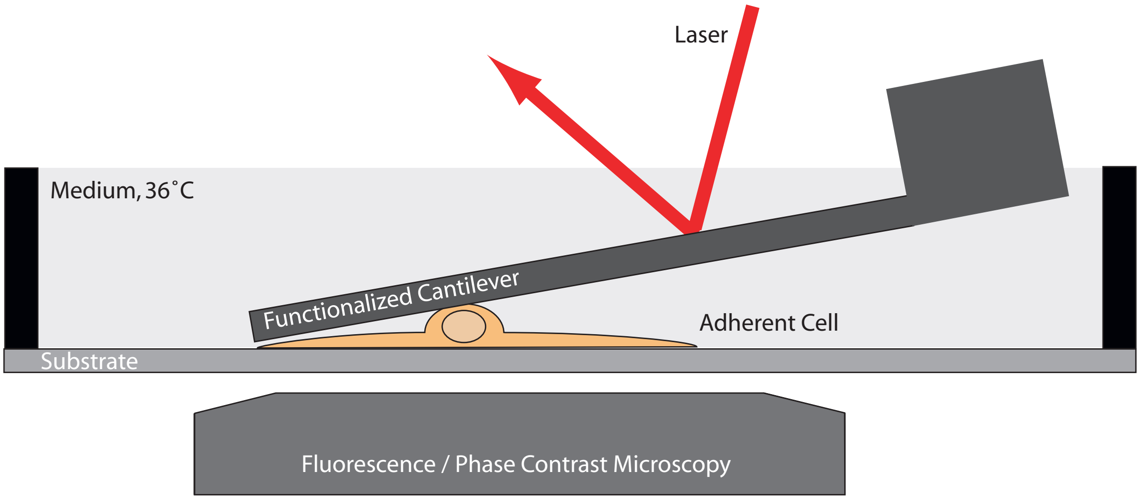

Figure 4.13: Sketch of a typical situation in a long-term adhesion experiment. A tipless, fibronectin coated cantilever touches the cell to induce cell adhesion at the cantilever. Upon cantilever retraction, the cell is detached from the substrate and the cell detachment is followed with fluorescence or phase contrast microscopy. The experiment takes place in a heated fluid chamber, which is filled with cell medium.

The data analysis for long-term adhesion experiments has to be performed in a completely different way than that of initial adhesion experiments. When cells are spread,

---

[3] For a protocol see the appendix.

their elastic properties can be anisotropic and subsequent detachment steps in the force spectrum arise with large cell elongation phases in between. For such experiments an analysis of the maximum cantilever deflection would be incorrect. Possibilities of interpreting the force curves are discussed in chapter 8.

4.4 Capabilities of the Different Techniques

Magnetic tweezers are an inexpensive and easy-to-handle experimental setup. However, the data information gained with magnetic tweezers in cell detachment experiments is much less than that of an AFM, where many different types of data can be generated with one single experiment. A force curve obtained with an AFM provides information on every detail of the detachment process, whereas with our magnetic tweezers setup only the total detachment force can be measured. By contrast, information on discrete molecular rupture events is delivered automatically with each AFM experiment.

Additionally, AFM experiments give information on the viscoelastic properties of the cell body by monitoring the viscoelastic cell creep or relaxation during the cell-substrate contact time. This is on the one hand an advantage, on the other a disadvantage of the AFM: it is an invasive system, whereas magnetic tweezers are rather non-invasive. The bead coupled to the membrane can hardly distort the cell during the measurement time. In contrast to this, the AFM cantilever influences the cell shape and behaviour, but the extent of this impact can be reduced by handling the cell-cantilever system with care. Hence, when AFM experiments are performed, the boundary conditions should always be monitored and controlled, otherwise the data could be misinterpreted.

The combination of RICM and magnetic tweezers allowed the time of cell detachment to be determined with high precision. A combined setup of RICM and AFM was not possible, since the RICM signal was superposed by strong reflections from the cantilever. However, a supplementation of the AFM with a TIRF setup can give particularly insight into surface-close adhesion processes.

An important advantage of the AFM compared to magnetic tweezers is that the experiments can easily be repeated with one and the same cell. Therefore the database of AFM experiments is larger than that of magnetic tweezers experiments. The main reason for supplementing the magnetic tweezers data with AFM experiments were the force limitations of the magnetic tweezers setup, whereas the range of applicable forces is almost unlimited for an AFM. This decision finally brought the breakthrough for the cell experiments (see chapters 7 and 8).

Part III

Adhesion on Nanopatterned Substrates

5 Surface Energy of Nanopatterns

As soon as it starts raining outside, we encounter wetting and dewetting processes by observing ball-shaped raindrops running down the window. Depending on the composition and structure of the glass, the shape of the water droplets at the surface differs. A common parameter for describing an adhesive contact of materials is the so-called surface energy.

The idea of our study was to create a biofunctional substrate of defined, tunable surface energy, where the adhesion between an adhering object and the substrate is mediated via specific bonds. For our approach the biotin-streptavidin bond was chosen to serve as binding system. This decision was due to its well-understood binding properties and its relevance for many applications from biosensors to single molecule experiments (Dahlin et al., 2005; Florin et al., 1994; Merkel et al., 1999; Green, 1990). A successful coupling of streptavidin to nanopatterned substrates implies that any kind of biotinylated molecule can be bound in a second step, which leads to a multitude of different surface functionalisations.

In this chapter, our approach for tuning and characterising the adhesiveness of streptavidin functionalised nanopatterns is presented.

5.1 Experimental Setup for Surface Energy Characterisation

In order to characterise the surface energy of the streptavidin nanopattern, we followed an optical approach developed some years ago by Moy et al. (1999). In our experiments, biotin-functionalised elastic agarose beads (B0519, Sigma, Germany) are allowed to equilibrate and adhere at a streptavidin functionalised, nanopatterned surface in 1x PBS (Gibco, Germany). Due to the long lifetime of the biotin-streptavidin interaction, the elastic bead adheres virtually irreversibly at the substrate. As a consequence of its adhesion at the streptavidin surface, the elastic bead deforms and enlarges its contact area with the substrate. This phenomenon is well-described by the *Johnson-Kendall-Roberts model* (JKR model), which relates the deformation of adhering elastic particles to the surface energy (see section 5.2). A sketch of the experiment is shown in figure 5.1 a. The surface energy in our study depends on the surface density of the streptavidin molecules, which is controlled by the nanopattern. We assume that not more than one streptavidin molecule can bind per gold dot, since the gold dots in the experiments had a maximum diameter of (6 ± 1) nm and the size of a streptavidin molecule is 10x10x12 nm^3 (Weber et al., 1989). The preparation and functionalisation of the gold nanopatterns was performed as presented in sections 3.1 and 3.3.2 and mPEG2000-urea served as a passivation agent to prevent protein attachment in between the gold dots of the nanopattern[1] (see section

---

[1] Most of the nanopatterned substrates used here were kindly prepared by F. Czerwinski.

3.2.1).

In order to measure the adhesion-induced deformation of the elastic beads, their contact area with the streptavidin nanopattern was measured by reflection interference contrast microscopy (RICM), where light of wavelength 546.1 nm was used to illuminate the probe (see section 4.1). By measuring the size of the dark patch in the centre of the interference pattern, the bead-substrate contact area could be determined from an RICM image (figure 5.1 b). The radius of the bead was determined with bright-field microscopy.

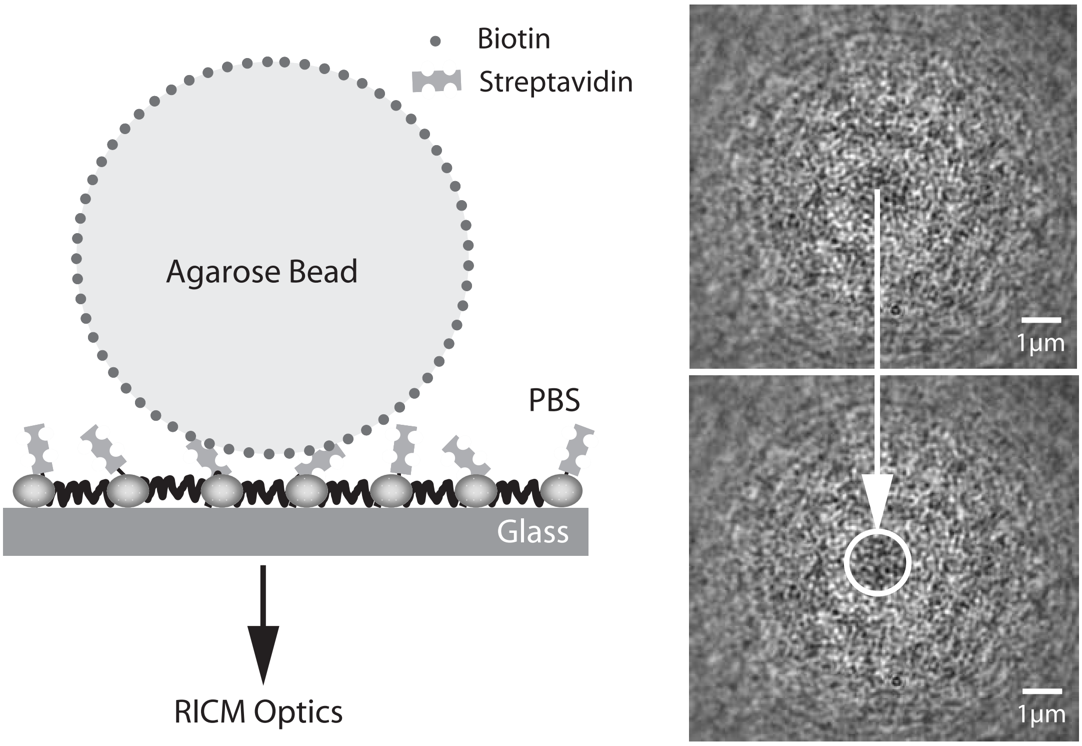

(a) (b)

Figure 5.1: (a) Sketch of the experimental system. An elastic, biotin-functionalised agarose bead rests on top of a streptavidin functionalised nanopattern. (b) RICM image of an adhering bead. The dark contact area is highlighted by a circle. An analysis of the RICM signal from this area is shown in figure 5.8.

To ensure a perfect surface passivation with PEG, the streptavidin nanopatterns were directly used after the surface preparation was completed. In order to obtain a better comparability of experimental data, most of the experiments were performed on samples where each half was covered with a nanopattern of different gold dot spacing. If the beads were left to equilibrate on the substrate for several hours, the magnitude of their convective motion reduced and they adhered preferentially to the streptavidin functionalised regions. Since the particles do not stick to the non-functionalised, PEG passivated region of the glass slide, the borderline of the streptavidin functionalisation is revealed by a particle accumulation along this line (figure 5.2).

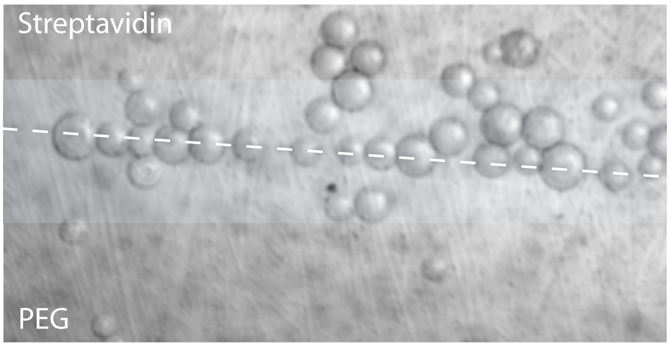

Figure 5.2: Accumulation of biotinylated agarose beads along the borderline between the streptavidin nanopattern and the passivated part of the substrate (dashed line) after an incubation time of 12 hours.

5.2 Models for the Elastic Contact of Solids

A first model describing the contact area between elastic spheres upon a compressive load was introduced by Heinrich Hertz (1882). The Hertz model does not take into account attractive interactions between the materials in contact, therefore it is only suitable for situations where loads are high compared to adhesive interactions. For small loads the Hertz model completely fails, since then attractive interactions lead to the formation of a contact zone which is significantly enlarged compared to that predicted by the Hertz model. Such attractive interactions are, for example, included into the Johnson-Kendall-Roberts (JKR) model. Both the Hertz and the JKR model are introduced in the following.

5.2.1 The Hertz Model

Hertz (1882) originally evaluated the contact of two elastic solid spheres. This result can be transferred to the situation where an elastic sphere of radius R is pressed with a force F onto a planar, rigid substrate. As a result of the load, the contact radius a and the indentation δ of the sphere become

$$a^3 = \frac{RF}{K},\ \delta = \frac{a^2}{R},\ F(\delta) = K\sqrt{R}\delta^{3/2}. \tag{5.1}$$

K is the bulk modulus of the elastic material and related to the Young's modulus E and the Poisson ratio σ via $K = 4E/3(1-\sigma^2)$. A sketch of this situation is given in figure 5.3.

The Hertz model has frequently been applied to characterise the elastic properties of soft colloidal particles and cells (Radmacher et al., 1992). In the studies presented in this chapter, the Hertz model was used to determine the Young's modulus of the elastic agarose spheres.

5.2.2 The Johnson-Kendall-Roberts Model

Measurements characterising the forces between two mica sheets in vacuum as a function of their separation demonstrated, that attractive forces of electrostatic and van der Waals origin cannot be neglected for surfaces in close contact (Tabor and Winterton, 1969). The

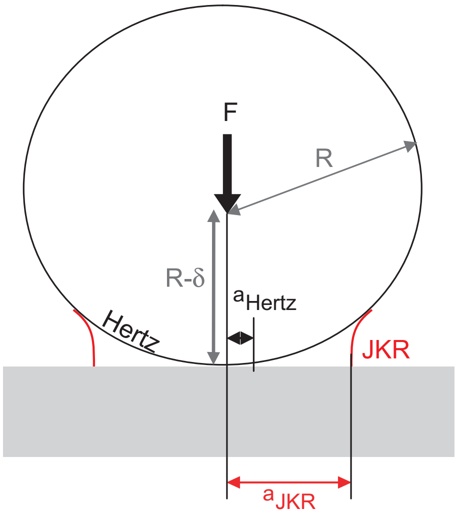

Figure 5.3: Comparison of the Hertz and the JKR model. An elastic sphere of radius R is pressed onto a rigid substrate by a load F. As a result of the load, the bead is indented by δ and a bead-substrate contact zone of radius a is formed. The image sketches the contact formation, as predicted by the two models.

surface energy, which is defined as the net change in free energy per newly formed contact area during adhesion, accounts for such interactions. A continuum mechanical description of the adhesive contact between elastic solids is provided by the JKR model (Johnson et al., 1971). This description is based on the assumption that the energy gain of the system due to adhesion is used for the elastic deformation of the interacting bodies at their contact zone (see figure 5.3).

In terms of the JKR model, the total energy U_T of an elastic sphere pressed onto a rigid, planar substrate is made up of two parts: the elastic energy U_E of the system and the surface energy W. Both of them depend on the radius of the contact zone, a:

$$U_T(a) = U_E(a) + W(a).$$

For the equilibrium condition, $\frac{dU_T}{da} = 0$, the contact radius a becomes

$$a^3 = \frac{R}{K}\left(F + 3W\pi R + \sqrt{6W\pi RF + (3W\pi R)^2}\right), \tag{5.2}$$

where K is again the bulk modulus and R the radius of the sphere, as introduced in section 5.2 (Johnson, 1985). This equation reverts to the ordinary Hertz equation 5.1 for zero surface energy, $W = 0$. Equation 5.2 also allows the force necessary to detach the sphere from the surface to be calculated:

$$F = -\frac{3}{2}W\pi R.$$

Interestingly, this force is independent of the elastic modulus. For zero load, $F = 0$, equation 5.2 simplifies to

$$a^3 = 6W\pi\frac{R^2}{K}. \tag{5.3}$$

This is the equation describing the situation in our experiments, where elastic beads adhered to adhesive substrates at zero external load.

5.3 Elasticity Measurements

Our approach to determining surface energy is based on measuring the elastic deformation of agarose beads, thus knowing the elastic modulus of the beads is essential.

To obtain the Young's modulus of the agarose beads, a defined vertical force was applied at the centre of the beads with a tipless cantilever (Mikromasch, Estonia) and force-extension curves were recorded with atomic force microscopy (JPK Instruments, Germany). For the analysis, the force-extension curves were transferred into force-indentation curves (Domke and Radmacher, 1998). This is necessary, since the piezo extension z is absorbed by both the cantilever and the sample, thus $z = d + \delta$, where d is the cantilever deflection and δ the indentation of the elastic sample. According to Hooke's law, cantilever deflection and loading force are related through

$$F_{load} = kd = k(z - \delta).$$

F_{load} as a function of δ is described by the Hertz model via equation 5.1.

The Young's modulus E was derived by fitting numerous force-indentation curves with the Hertz model. Figure 5.4 a shows a typical force-extension curve. In the plot, two regimes are distinguished, on the one hand the regime where the cantilever is not in contact with the bead, on the other hand where it induces an elastic bead deformation. Figure 5.4 b shows a force-indentation curve and its Hertzian fit. The Poisson's ratio σ was taken to be 0.5, as agarose with its long sliding polymer chains can be assumed to show an elastic behaviour similar to that of rubber (Courtney, 1990; Landau, 1991). Using this method, the Youngs's modulus of the beads was determined to $E = (185.4 \pm 11.9)$ kPa.

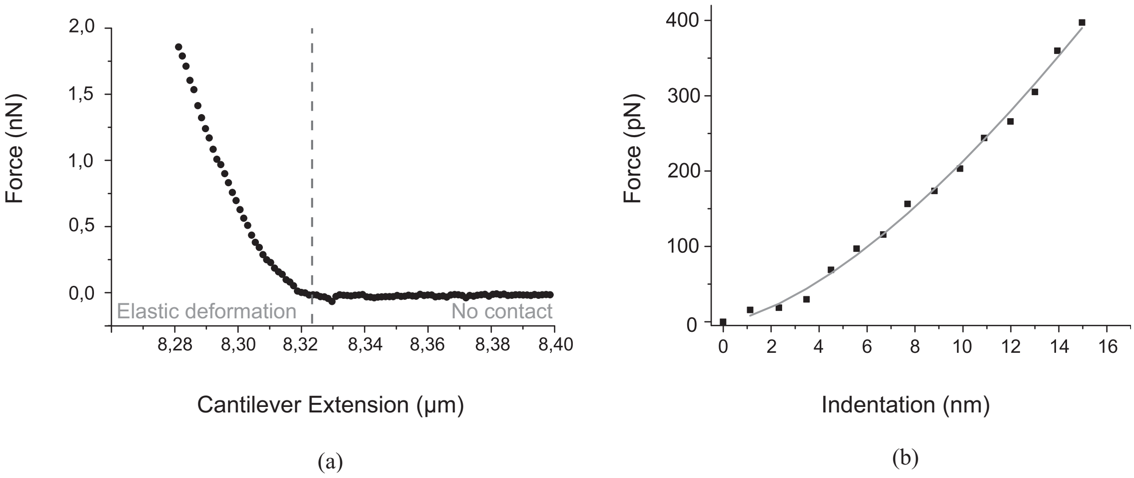

(a) (b)

Figure 5.4: Measurements of the Young's Modulus. (a) Elastic response of the agarose bead upon indentation. (b) Fit of the force-indentation curve with the Hertz model.

5.4 Surface Energy of Streptavidin Functionalised Nanopatterns

According to the JKR model, the surface energy for the experimental situation presented here is obtained by relating the contact area of nanopattern and agarose bead to the bead radius by equation 5.3. Figure 5.5 shows data from a typical experiment, where the radius and the contact area of approximately fifty beads were measured. In figure 5.5 a, a plot of the data with the respective JKR approximation is presented, whereas in figure 5.5 b the double-logarithmic plot of the same data set is shown. For evaluating the experimental data, all external loads are neglected, as is gravitation.

This is justified as follows: The density of dry agarose is 1.64 g/cm^3 (Laurent, 1967; Johnson et al., 1995) and the bead solution contains 4% biotinylated agarose in an aqueous PBS solution (as specified by Sigma, Germany). Therefore the resulting density of an agarose bead is 1.0056 g/cm^3, considering the buoyancy in the liquid the effective density in the buffer solution becomes $\rho = 0.0056$ g/cm^3. The contribution of gravity can be estimated by comparing the magnitude of the different terms in (5.2). This calculation reveals that the gravitational load is indeed negligible, because for a typical experimental situation the corrections induced by gravity are two orders of magnitude smaller than the values of the remaining terms.

A verification of the applicability of equation 5.3 is given by the logarithmic plot (see figure 5.5 b). The slope of this linear fit does not deviate significantly from 2/3, in accordance with (5.3). This suggests that the adhesion conditions in our experiments allow the JKR model to be applied.

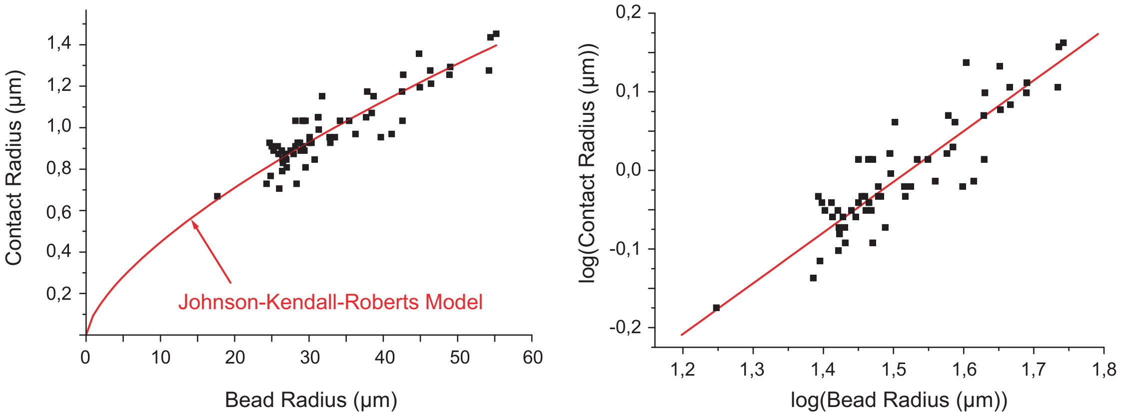

(a) (b)

Figure 5.5: (a) Plot of the data from a typical experiment on a nanopattern with (77 ± 7) nm gold dot spacing, fitted with equation 5.3. (b) Logarithmic plot of the same experimental data. A linear fit of this data yields a slope of 0.68 ± 0.07, in agreement with equation 5.3.

For all our experiments the surface energy was determined by a least squares fit of the data with (5.3). However, the total surface energy W_{tot} not only contains information about the streptavidin-biotin interaction but also includes the nonspecific interaction, $W_{nonspec}$, between bead and substrate. Therefore the samples used for the experiments were only partly covered with a nanopattern, the remaining part contained the pure PEG passivation. $W_{nonspec}$ was measured on the nanopattern-free part of the substrates and then subtracted from W_{tot} for each data set, giving W_{corr} as a first correction of surface

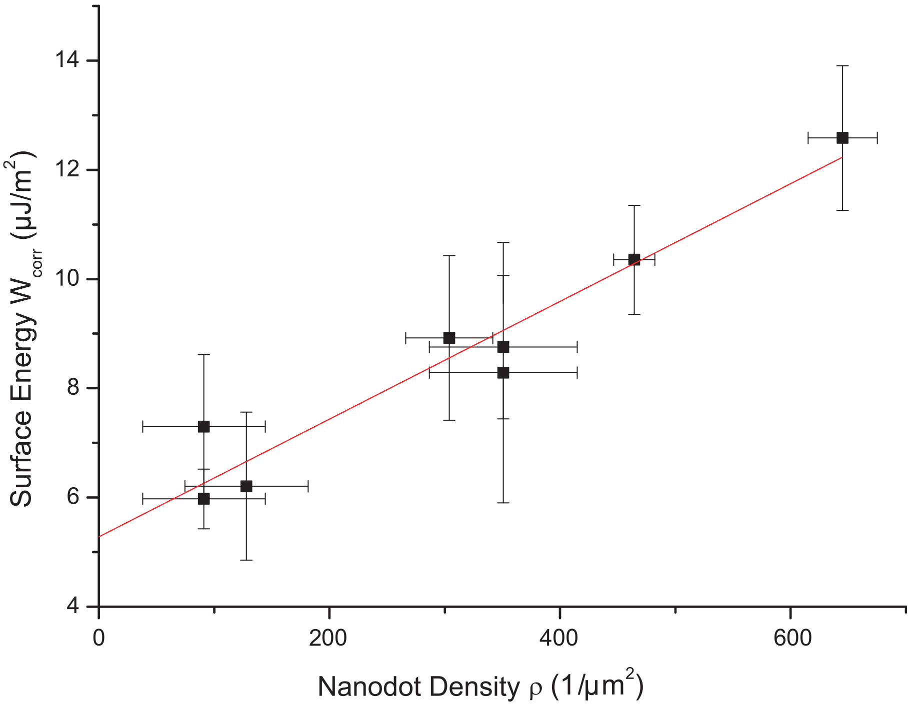

Figure 5.6: Linear dependence of the surface energy on the nanodot density. The error bars in the surface energy refer to the standard error in the mean. The mean nanodot density on a sample was determined by averaging the nanodot densities of several surface spots. The error bars refer to their standard error in the mean.

energy. Figure 5.6 shows data of W_{corr} at different nanodot densities. The experiments reveal a linear relationship between the surface energy and the nanodot density, which is in turn related to the streptavidin density. Although the surface energy values have been corrected for nonspecific interactions, the linear fit still shows a residue value W_0 for zero streptavidin density. This finding suggests that not all nonspecific interactions are taken into account in $W_{nonspec}$. Presumably, the interaction of the bead with the gold dots is responsible for this behaviour. Since gold has an enormously high surface energy contribution (Metzger et al., 2001) of about 1 J/m^2, we expect a residue in spite of the streptavidin functionalisation and the surface passivation. To check the influence of this interaction, we performed experiments with samples where the gold dots were not functionalised with streptavidin, but directly interacting with the beads. On these samples we found stunningly high surface energy values. Bar 1 in figure 5.7 shows the additional contribution to surface energy by the gold nanopattern. In order to account for the bead-gold interaction W_{corr} was further corrected by subtracting W_0 from the data, which yielded values for the pure streptavidin-biotin-mediated surface energy W_{spec} (table 5.1).

The necessity of a surface passivation becomes clear from additional experiments, where the surface energy was measured on a non-passivated glass slide. The surface energy obtained for the glass slide was (34.8 ± 1.9) µJ/m^2, compared to (4.8 ± 1.1) µJ/m^2 on a freshly prepared PEG substrate. This demonstrates that glass-mediated interactions are successfully screened by the PEG layer. However, the PEG layer is to some extent

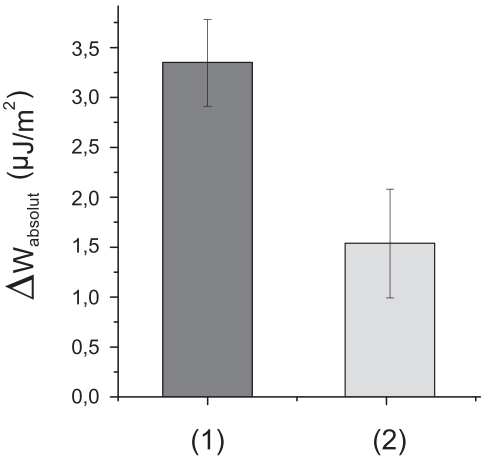

Figure 5.7: Differences in surface energy ΔW due to surface composition and treatment. (1) ΔW between a non-functionalised, PEG passivated, nanopatterned substrate and a PEG passivated, nanopattern-free substrate. (2) ΔW between a pure PEG passivated substrate and a PEG substrate after application of streptavidin binding chemistry.

Streptavidin density ρ ($1/\mu m^2$)	$\Delta\rho$ ($1/\mu m^2$)	W_{spec} ($\mu J/m^2$)	ΔW_{spec} ($\mu J/m^2$)
91	0.53	1.36	0.66
304	0.38	3.64	1.57
351	0.64	3.99	0.76
464	0.18	5.07	1.08
645	0.30	7.30	1.39

Table 5.1: Surface energy W_{spec} and standard errors in the mean ΔW_{spec} after correction for all nonspecific contributions for the streptavidin densities $\rho \pm \Delta\rho$.

affected by the streptavidin binding procedure, as shown in bar 2 of figure 5.7, where the difference in surface energy of a PEG substrate before and after streptavidin binding is given. This justifies our experimental protocol to measure a reference value for nonspecific adhesion on each particular sample. The increase in surface energy as a result of surface functionalisation might either be explained by an incorporation of adhesion molecules into the PEG layer or by a degradation of the passivation due to the extended preparation time, since the PEG layer has been observed to gradually lose its passivation ability with storage time.

5.5 Discussion

A similar approach of utilising elastic beads to measure surface energies has been used recently to study the biotin-streptavidin interaction as a function of pH and ionic strength (Moy et al., 1999). Both this study by Moy et al. (1999) as well as the one presented here are facing the problem, that the measured surface energies are lower than expected. From affinity experiments a binding energy contribution of about 35 kT for each streptavidin-biotin bond is estimated (Green, 1990). In contrast to affinity measurements, where binding partners are free to move in solution, in our experiments the binding partners are coupled to surfaces. Recently it was shown that the free enthalpy of binding is strongly decreased when proteins are anchored to surfaces (Nguyen-Duong et al., 2003). Therefore it is not surprising that our values of surface energy are one order of magnitude smaller than the values expected from binding affinity measurements. Additionally, also an incomplete coverage of the nanopattern with streptavidin cannot be excluded and might be responsible for a certain decrease in surface energy. Another reason accountable for a reduced surface energy in our experiments is the surface roughness of the agarose beads, which prevents their full contact with the surface. In figure 5.8 a, a reconstruction of the surface profile of a bead's contact area is shown, which was calculated from an RICM image by equation 4.1. In spite of the roughness of the beads on the 100 nm scale, the JKR model was still applicable but the effective surface energy is assumed to be decreased, since only about 10 % of the bead surface can be linked to a streptavidin molecule on the surface (see 5.8 b). Figure 5.8 c shows a SEM image of a dried agarose bead, verifying its surface roughness.

To summarise, our results for the surface energy between streptavidin functionalised nanopatterns and biotinylated beads show that, using a nanopatterning technique, we have a method available to adjust the surface energy of bio-adhesive samples over a wide range [2]. So far, we could vary surface energies by a factor of 5.3. In the meantime, progress was made to enlarge the spectrum of possible gold dot distances, so that now also four times smaller surface energies can in principle be achieved. This applicability of nanostructures for imprinting surface energies on substrates opens new avenues to investigate the adhesion of biomimetic systems such as giant vesicles, since for these studies substrates with well-defined and tunable adhesive strengths are desperately needed.

---

[2] The results of this study are published in Selhuber et al. (2006).

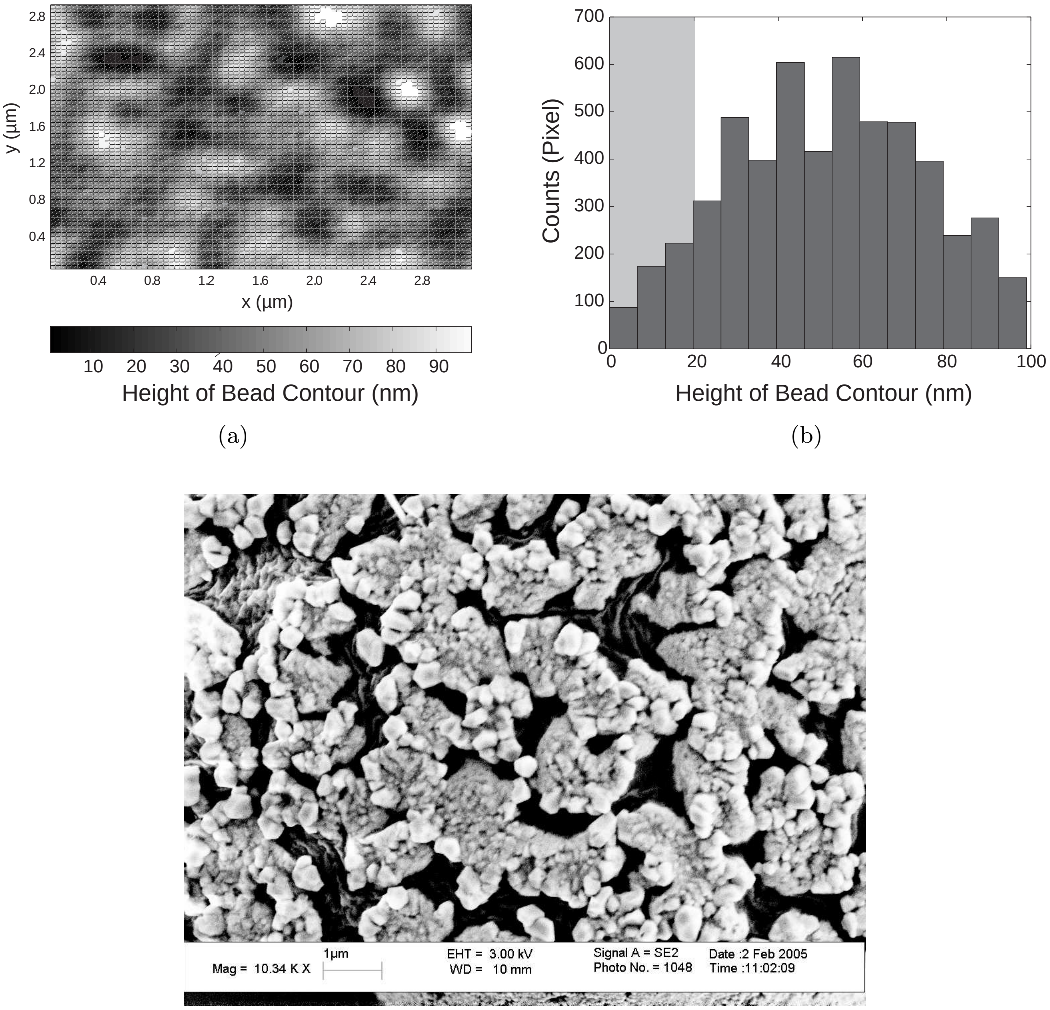

(a) (b)

(c)

Figure 5.8: (a) Height reconstruction of the bead contour in the bead-surface contact area by equation 4.1. (b) Distribution of the distances between glass surface and bead contour. Due to the size of the streptavidin and the gold dots, the bead is assumed to bind to streptavidin molecules up to a height of 20 nm above the substrate. Thus, not more than about 10 % of the streptavidin molecules in the contact zone can be coupled to the agarose bead. (c) Scanning electron micrograph of an agarose bead. Surface ruffles, similar to those observed with RICM, are clearly resolved. The cracks between agarose clots are caused by the drying of the normally water-swollen polymer.

6 Cell-Surface Contact Formation

An intriguing feature of fibroblasts is their spreading on two-dimensional surfaces. During spreading, the cells transfer their originally round shape into a pancake-like, flat and extended geometry and thus increase their area of surface contact enormously. An enlargement of the cell-surface contact area is essential for cells derived from the connective tissue, because they are dependent on a tight contact with their surrounding matrix. Still, little is known about the cell-surface contact at the very early steps of cell adhesion, although first optical studies have been performed to investigate this stage of adhesion (Cohen et al., 2006). One aspect of such initial adhesion processes, the formation of microspikes, which is addressed in the first part of this chapter. The second part deals with the evolution of cell spreading on nanopatterned substrates, which has been the subject of recent work (Arnold et al., 2004; Cavalcanti-Adam et al., 2006) and in this thesis we explain the previous results with a mathematical model. Furthermore, cell spreading on nanopatterns was investigated for different passivation chemistries, to determine their impact on cell spreading. The last part of this chapter is dedicated to the old, but still unsolved question of what conclusion can be drawn from RICM data on focal contacts.

6.1 Substrate Exploration by Cells

In this section we present observations for cell adhesion processes, which occur in close proximity to the substrates and could be observed with reflection interference contrast microscopy (RICM).

Figure 6.1 shows RICM images of a cell while hovering above a substrate right before

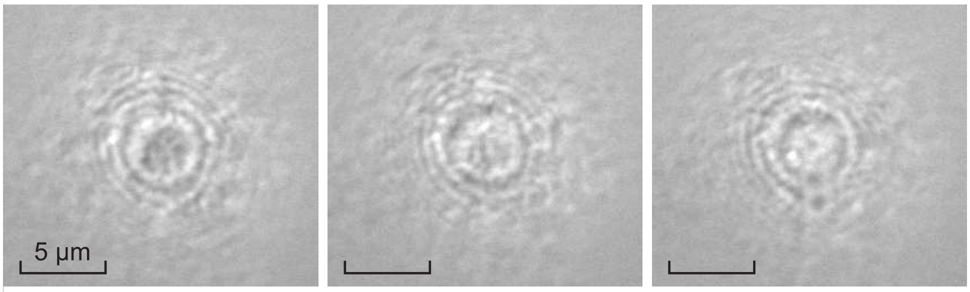

(a) (b) (c)

Figure 6.1: Newton's rings in the RICM interference pattern of a cell hovering above a surface prior to adhesion. Time stamps of the images: (a) $\Delta t = 0$ msec (b) $\Delta t = 97$ msec (c) $\Delta t = 192$ msec.

it touches down for the first time. This cell has a round shape and the light reflected at the cell envelope and the glass surface leads to the typical *Newton's rings*, the interference pattern observed for spherical objects in RICM. At this stage, the cell lacks a stable contact zone, as can be deduced from the strong fluctuations in the interference pattern (for details on RICM see section 4.1).

The situation changes dramatically when the cells find a first anchor point at the substrate. For strongly adhesive substrates this is already the case several minutes after cell seeding. An RICM observation of a cell adhering to fibronectin is shown in figure 6.2 a. In this example, an area of close cell-substrate contact has formed, corresponding to the dark, speckled area in the centre of the image. This area is surrounded by an irregularly

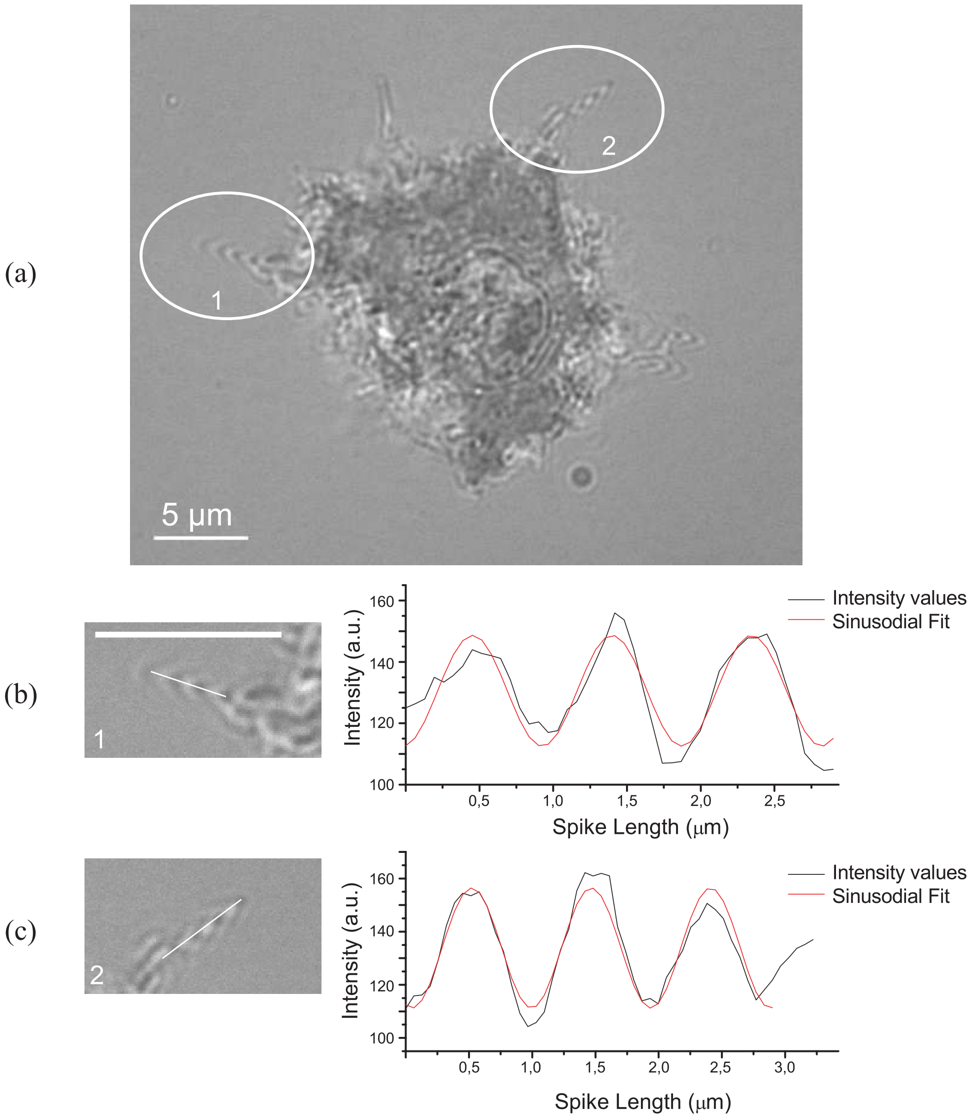

Figure 6.2: (a) RICM image of a cell adhering to a fibronectin substrate. At the time of image recording the cell has been in close contact with the substrate for several minutes. In (b) and (c) magnifications of the RICM signal from microspikes are shown. The intensity variations obtained with RICM are fitted with sinusoidal functions. The scalebars refer to a length of 5 µm.

shaped cell boundary, which contains several spiky bulges[1]. When observed with RICM, these spikes show periodic light and dark interference stripes. Notably, they are hardly visible with phase contrast microscopy.

Figures 6.2 b and c give two examples, where the interference pattern of microspikes was determined an analysed. The sinusoidal variation of the pattern and especially the constant spacing of the interference maxima and minima indicates that the spikes have the shape of straight rods pointing out from the cell, according to formula 4.1 (section 4.1). For cells adhering to fibronectin substrates, the average projected spike length calculated from 23 samples was (3.4 ± 1.5) µm and their angle relative to the surface was (12.1 ± 4.8)°. Hence, the effective spike length was on average (3.5 ± 1.7) µm. All these data were derived from cells which adhered to the substrate for 5 to 15 minutes.

As already mentioned in section 1.3.1, microspikes are membrane-enclosed, actin fibre and fascein containing structures of 2-10 µm length and 0.2-0.5 µm diameter. Thus, we suggest that the observed spiky cell structures are microspikes and not filopodia, due to their relatively short length. A precise measurement of the spike diameter is not possible, since it is close to the optical resolution limit. Thus, a clear cut edge of the spikes was never observed. In order to test whether actin participates in spike formation, we performed a control experiment, where the standard cell medium was exchanged to medium containing 1 µM cytochalasin D. Cytochalasin D is a fungal alkaloid which interferes with actin polymerisation (Voet and Voet, 1995). Microspike formation stopped when cytochalasin D was present and started again after exchanging the medium back to standard cell medium. This indicates that actin polymerisation and microspike formation are indeed directly related.

The dynamics of spike formation are rapid. Microspikes are formed within several tens of seconds and can be retracted at the similar timescale. Their lifetimes vary greatly: some

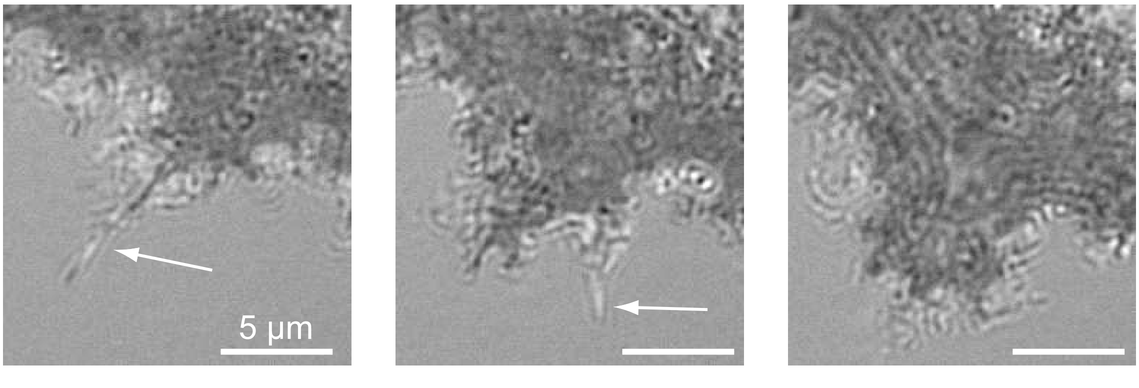

(a) (b) (c)

Figure 6.3: Temporal development of the cell adhesion area, induced by the formation of microspikes (arrows). (a) Single microspike. (b) Formation of an enlarged cell adhesion area and an additional microspike after 3.7 minutes. (c) Cell-substrate contact zone 8.3 minutes after (a).

---

[1] Experimental conditions: Rat embryonic fibroblasts (REF 52 WT) were trypsinised and resuspended. For cell spreading experiments, the supernatant was removed and the pellet was resuspended in 1-2 ml DMEM containing 10% FBS, 2% L-Glutamine). A fibronectin coated glass slide (for preparation see appendix) was glued with silicon grease to a teflon sample holder where the cell solution was added. RICM experiments were performed using green light with a wavelength of 546.1 nm.

disappear after a few seconds, while others scan the substrate for a long time, ranging out from the cell body at different angles. Eventually, some spikes stick to the substrate and direct cell attachment by paving the way for subsequently formed new cell adhesion area, as shown in the time-series of figure 6.3. Figure 6.3 a shows a microspike (arrow) pointing out from the cell adhesion area and figure 6.3 b presents how the spike has directed the formation of new cell adhesion area after only 3.7 minutes. This image also shows the formation of an additional microspike and after further 4.6 minutes the whole region around the two spikes has become part of the cell-substrate contact zone.

Microspikes have first been reported in the literature 30 years ago, where they were visualised in scanning electron microscopy studies. Such early studies revealed microspikes and filopodia to be straight extensions from the cell, as shown in figure 6.4 (Albrecht-Buehler and Goldman, 1976; Albrecht-Buehler, 1976).

To our knowledge, no live cell study on the geometry and dynamics of microspike formation has been performed so far. In this study, RICM has proven to be a good tool for unravelling microspike nature, especially since it does not require time-consuming, difficult preparation steps as necessary for SEM studies. Instead, RICM monitors cell adhesion *in vivo* without the risk of imaging artefacts caused by sample drying, which is a substantial problem of SEM studies.

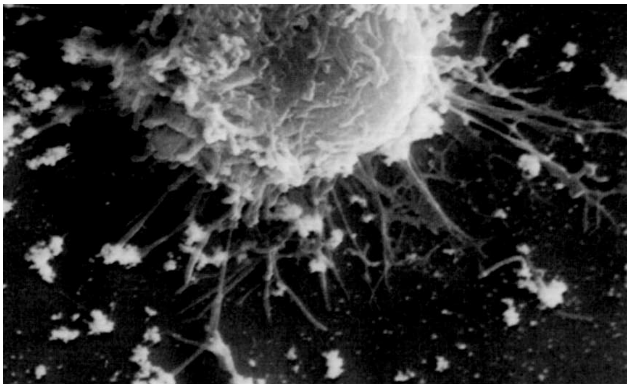

Figure 6.4: SEM image from an adhering cell. The microspikes are the long, straight membrane extensions formed between cell and surface (from Albrecht-Buehler and Goldman (1976)).

6.2 Fibroblast Spreading and its Quantitative Description

Several recent studies have tried to describe the progression of cell spreading by mathematical models. Depending on the cell type, the evolution of cell spreading with time was modelled using an error function for endothelial cell spreading (Reinhart-King et al., 2005), a hyperbolic tangens for *D. discoideum* (Chamaraux et al., 2005) and a power law function for fibroblast cells (Döbereiner et al., 2004). All these functions are characterised by a quasi-linear increase of cell spreading area with time followed by a plateau value.

The model proposed by Döbereiner et al (2004) for fibroblast spreading is expected to fit the cell data of our study, since we are using a similar cell type. This particular model describes cell spreading as a three-phase process, where each of the phases can be modelled

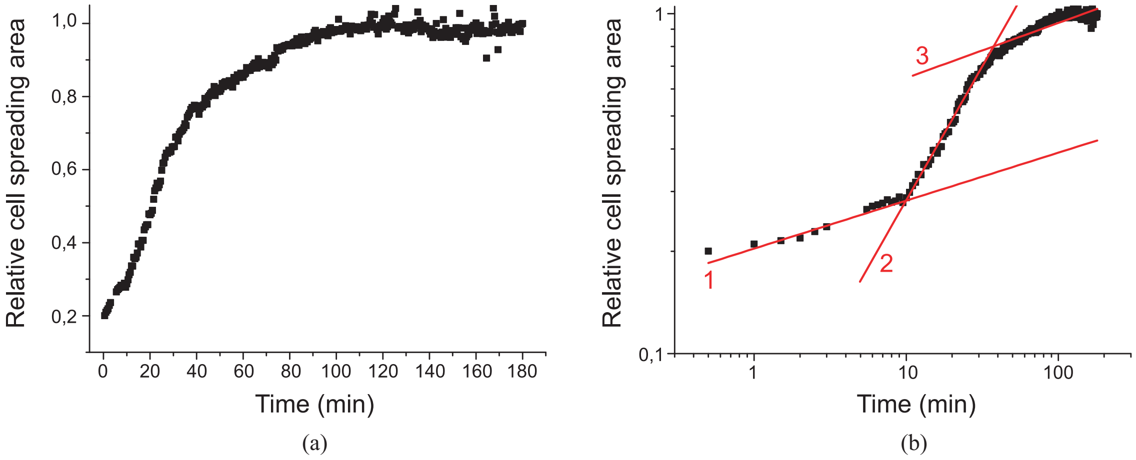

Figure 6.5: Typical time-course of the relative cell spreading area of a fibroblast on a (58 ± 6) nm RGD nanopattern. (a) Spreading area versus adhesion time. (b) The same data in a double-logarithmic plot, showing the three spreading phases. Each of these phases was fitted with equation 6.1. The fit functions of the three phases are numbered in the graph and for this example we obtained $\alpha_1 = 0.14 \pm 0.06$, $\alpha_2 = 0.74 \pm 0.03$ and $\alpha_3 = 0.14 \pm 0.01$.

by a power law relation between cell spreading area and adhesion time:

$$A(t) \propto t^{\alpha_i}, i = 1, 2, 3. \tag{6.1}$$

To investigate cell spreading on nanopatterns in the framework of this model, we have analysed data previously taken by Ada Cavalcanti-Adam and Eva Kowalinsiki in phase contrast microscopy on fibronectin surfaces and RGD nanopatterns[2]. To detect the edge of spread cells, an algorithm which performs a morphological image segmentation was employed[3] (Mathworks, MA) and extended by a graphical user interface to make a high-throughput image analysis possible[4].

As known from earlier analyses, the cell spreading behaviour depends strongly on the distance of integrin binding sites offered by nanopatterned substrates (Cavalcanti-Adam et al., 2006). By automatising the image processing, it was much easier to measure the cell spreading area over a large number of time points than with the previous time-consuming by-hand analyses. Two examples of our analyses are shown in figures 6.5 and 6.6. Figure 6.5 a shows data for the spreading of a cell on a nanopattern with 58 nm integrin binding site spacing. From this plot it is obvious that the cell spreading area strongly increases with time before it reaches a rather stable plateau value. In the double-logarithmic plot of figure 6.5 b, the three spreading phases described by Döbereiner et al. (2004) can be identified. For such data it was possible to approximate the spreading behaviour by equation 6.1, showing that each of the spreading phases qualitatively follows the power law proposed by Döbereiner et al. (2004).

---

[2] Experimental conditions: For cell adhesion experiments, trypsinised for 5 min, re-suspended and washed in complete DMEM and plated at a density of 1-5x10^5/sample in DMEM containing 1% FBS. The live imaging was performed in a humidified chamber which contained CO_2 in its atmosphere and was held at 37°C. Images were taken with phase contrast microscopy.

[3] Matlab, Image Processing Toolbox Demos, “Detecting a Cell Using Image Segmentation”.

[4] The image analysis was performed together with C. Hökel.

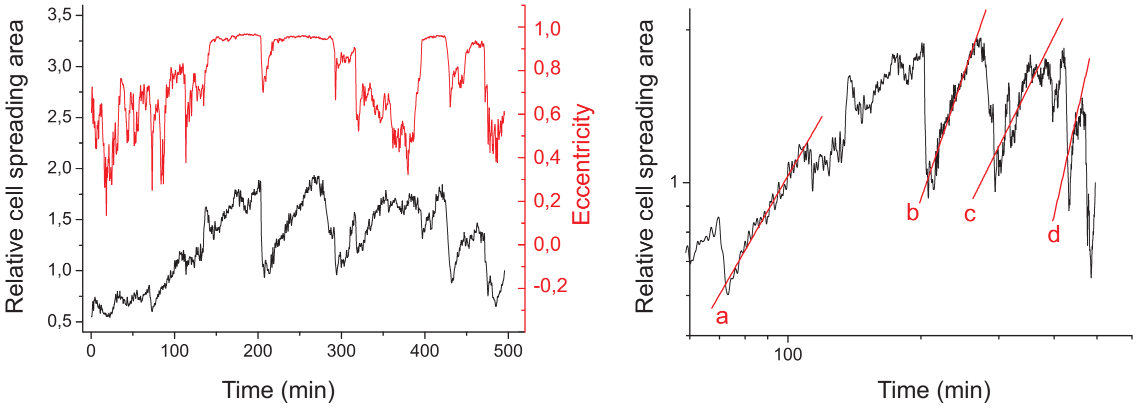

(a)

(b)

Figure 6.6: Cell spreading on a (108 ± 6) nm RGD nanopattern. (a) Linear plot of the relative cell spreading area and eccentricity as a function of time. (b) Log-log plot of the same data. The red lines represent approximations of the spreading data by equation 6.1 and the slopes of the spreading processes a-d were fitted to $\alpha_a = 1.53 \pm 0.04$, $\alpha_b = 2.53 \pm 0.08$, $\alpha_c = 1.75 \pm 0.06$ and $\alpha_d = 3.86 \pm 0.47$.

Compared to cell spreading on 58 nm nanopatterns or fibronectin, cells placed on a nanopattern with a distance of integrin binding sites of 108 nm exhibit delayed spreading and perform repeated spreading-retraction cycles without allowing a plateau in cell spreading area to be reached. Additionally, these cells do not adopt a round pancake-like shape during spreading, instead they elongate. As soon as they retract, they become spherical. The black curve in figure 6.6 a shows the typical situation for a cell performing spreading-retraction cycles over a timescale of several hours. The elongation of cells during cell spreading can be followed by the values of eccentricity[5], as shown with the red curve of figure 6.6 a. From this graph it is obvious, that the spreading-retraction cycles coincide with cell rounding-elongation cycles. Interestingly, the recurrent spreading phases also follow a power law behaviour. The obtained values for these α_x are similar for several spreading-retraction cycles of a single cell, as indicated in figure 6.6 b. This result is important, because it indicates that the spreading behaviour is not changed by ECM proteins, which are continuously secreted by the cell. A comparison of the power law exponents obtained for the spreading phases on fibronectin and on nanopatterns of 58 and 108 nm integrin binding site spacing is given in table 6.1.

For substrates where three cell spreading phases could be determined (58 nm RGD nanopatterns, fibronectin surfaces), the values received for the exponents α_i follow the spreading behaviour reported by Döbereiner et al. (2004) for fibroblast spreading on fibronectin substrates: a slow initial spreading phase is followed by a fast spreading in the second phase ($\alpha_2 > \alpha_1$) and the spreading velocity slows down again in the third phase ($\alpha_3 < \alpha_2$). Our result for spreading on fibronectin surfaces is qualitatively similar to that of Döbereiner et al. (2004). The difference in the precise numbers of the α_i between the two studies can be attributed to the usage of a different cell type and a different preparation protocol for binding fibronectin to the surface. A comparison of our values

---

[5] The eccentricity was determined by approximating the cell region by an ellipse that has the same second moment as the cell region. The eccentricity is defined as the ratio of the distance between the foci of the ellipse and its major axis length. A perfect circle has an eccentricity of 0, a line has eccentricity 1.

Substrate	α_1	$\Delta\alpha_1$	α_2	$\Delta\alpha_2$	α_3	$\Delta\alpha_3$	No. of analyses
Fibronectin, Döbereiner	0.4	0.2	1.6	0.9	0.3	0.2	20
Fibronectin	0.2	0.1	0.9	0.1	0.2	0.1	4
58 nm	0.1	0.04	0.7	0.2	0.1	0.03	3
110 nm	-	-	2.45	1.65	-	-	10

Table 6.1: Exponents α_i with standard deviations $\Delta\alpha_i$ for power law descriptions of cell spreading in the different spreading phases. Values for fibronectin substrates given in Döbereiner et al. (2004) are compared with data obtained from our experiments. Data on nanopatterned substrates with 58 nm and 108 nm integrin binding site spacing are added. For 108 nm integrin binding site spacing α_2 is the exponent for the recurrent spreading phases. The errors of our analysis refer to standard deviations.

for the α_i between fibronectin and 58 nm nanopatterns indicates that the cell spreading on nanopatterns is decelerated in all three spreading phases. This result can be explained by a reduced density of integrin binding sites on nanopatterns compared to homogeneous fibronectin surfaces, so that the cells need a longer time to find ligands to bind to. In the case of 108 nm nanopatterns, α_2 was determined for the repeated spreading cycles. These spreading cycles proceed much faster than in the spreading phases on fibronectin or 58 nm RGD nanopatterns, as shown by the large value of α_2.

This study quantitatively supports the hitherto existing results about cell spreading on nanopatterns (Cavalcanti-Adam et al., 2006; Arnold et al., 2004), but now describes the strong dependence of cell spreading on integrin binding site spacing in terms of a mathematical model. So far, the biological mechanisms behind the differences in the cell spreading process on different RGD nanopatterns are not solved. However, the finding of three distinct spreading regimes gives some hints to the existence of three different mechanisms controlling the biological spreading process, which are obviously distorted by the large distance of integrin binding sites on a 108 nm nanopattern.

6.3 Dependence of Cell Adhesion on Passivation Chemistry

In section 3.2, two PEG systems were introduced which can be used for preventing nonspecific protein adsorption on nanopatterned substrates. In most of the studies performed in our group, a surface passivation with mPEG2000-urea is used. However, the preparation of mPEG2000-urea passivated substrates is time-consuming and the necessary reagents are sensitive and hazardous. Therefore an alternative passivation method with PLL-g-PEG polymers was established in the scope of this thesis. The PLL-g-PEG passivation has been developed in the group of Marcus Textor at the ETH Zürich, where they could show that nonspecific cell adhesion on glass substrates is prevented for up to ten days with the PLL-g-PEG (VandeVondele et al., 2003). Additional studies demonstrated a substrate coating with a 12 nm thin layer of niobium oxide (Nb_2O_5) prior to PLL-g-PEG binding leads to an enhanced passivation stability compared to SiO_2 surfaces and allows cell adhesion to be prevented for up to 13 days (Lussi et al., 2006).

Figure 6.7 shows images of fibroblasts, which are spreading[6] close to the dipping edge

---

[6] In the experiments, REF YFP Pax fibroblasts were cultivated on nanopatterned substrates in DMEM, containing 2% FBS, 2% L- glutamine and 100 µg/ml penicillin-streptomycin.

of a 28 nm RGD nanopattern. This nanopattern was passivated with PLL-g-PEG and biofunctionalised as described in chapter 3. After one hour of adhesion, the dipping edge is still the borderline of cell spreading. As evident from image 6.7 b, after adhering for 12 hours the cells crossed this borderline[7].

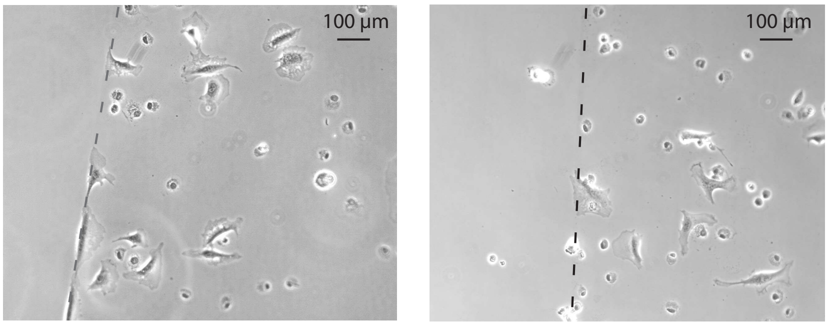

(a) (b)

Figure 6.7: Time series of a cell spreading in the proximity of the dipping edge (dashed line) for a PLL-g-PEG passivated, RGD functionalised nanopattern. (a) 1 hour, (b) 12 hours after cell seeding.

To check for an influence of the particular passivation chemistry on the cell spreading process, experiments were performed in order to compare the cell spreading areas for PLL-g-PEG and mPEG2000-urea passivated nanopatterns. These experiments were performed at a single day, since then variations due to differences in cell culture history could be excluded. Figure 6.8 a shows a comparison of the cell spreading areas after four

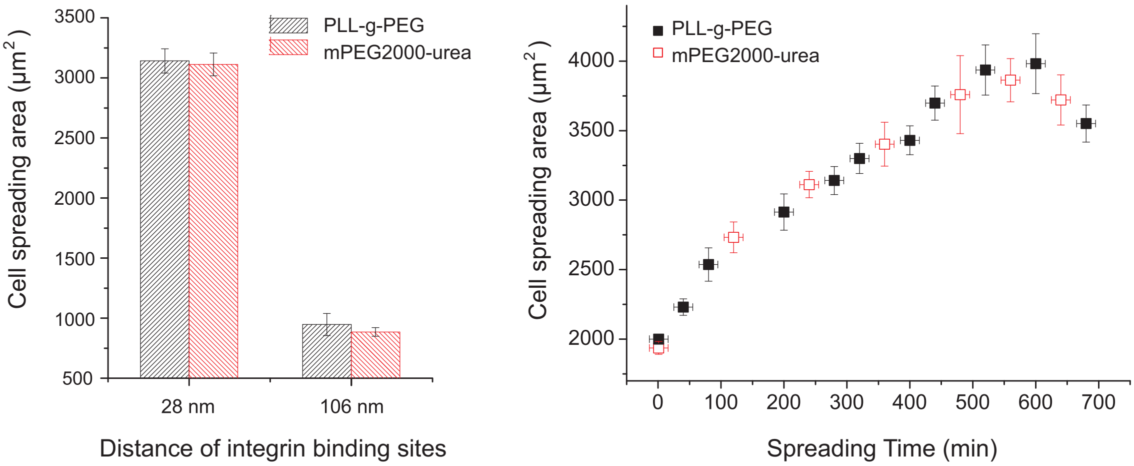

(a) (b)

Figure 6.8: (a) Spreading areas of cells after spreading for 4 hours on PLL-g-PEG and mPEG2000-urea passivated, nanopatterned glass slides. (b) Temporal development of the cell spreading area in a direct comparison between the two passivations on a 28 nm substrate. For determining the mean spreading areas, more than 50-100 cell spreading areas were evaluated per substrate with the Matlab algorithm presented in 6.2. Error bars refer to the standard error in the mean.

---

[7] These experiments were performed together with M. Geibel.

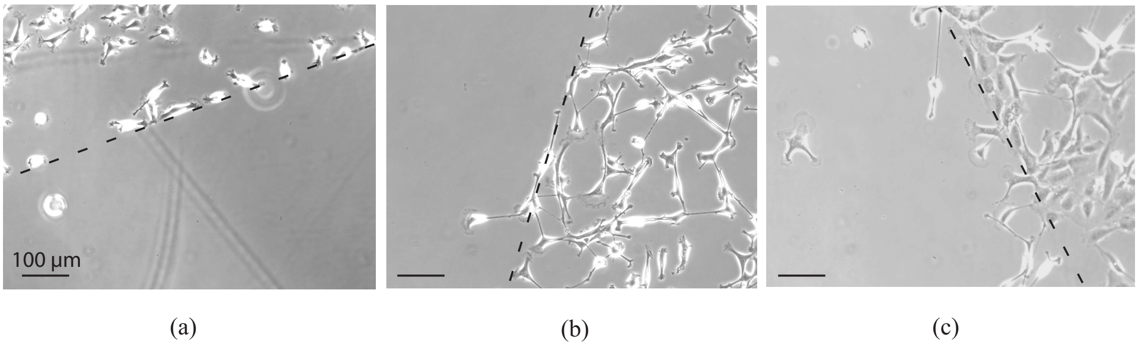

(a) (b) (c)

Figure 6.9: Phase contrast image of cells spreading close to the dipping edge (dashed line) on a Nb_2O_5 coated, nanostructured (70 nm), biofunctionalised substrate. (a) 3 hours, (b) 24 hours and (c) 48 hours after cell seeding.

hours of cell spreading on a 28 nm RGD nanopattern and a 106 nm RGD nanopattern, respectively. The results of the cell spreading areas for the two passivations coincide in the range of the errors. In order to give a direct comparison of the development of cell spreading areas with time, figure 6.8 b shows a time series of cell spreading areas on a 28 nm nanopattern for the two different PEG passivations. From this comparison it is evident that cell spreading does not depend on the particular passivation chemistry used here.

Additionally we probed, if the timescale of passivation stability could be increased by dip-coating Nb_2O_5-coated samples instead of bare glass[8]. As shown in the images of figure 6.9 for a 70 nm RGD nanopattern, the Nb_2O_5 coating leads to a stable PLL-g-PEG passivation for up to 24 hours. After 48 hours, the cells start to cross the dipping edge also on these substrates. However, a stable passivation for 24 hours is already a big improvement for long-term cell adhesion studies, which are, for example, necessary to investigate the protein expression of cells on different nanopatterns. Thus, by using this simple coating procedure a large database could efficiently be achieved.

The results show that the PLL-g-PEG prevents adhesion on nanopatterned substrates for much shorter timescales (12 hours on glass, 24 hours on Nb_2O_5) compared to non-nanostructured substrates, as reported in literature (Lussi et al., 2006). This reduced passivation stability could be a result of the gold dots which are embedded in between the passivation layer and serve as distinct cell anchorage sites. Cells could then actively remodel the space around the anchorage site and in this way degrade the passivation layer in the surroundings of a gold dot.

6.4 RICM Studies of Focal Contacts

Although many properties of focal contacts have been unravelled in recent years, the influence of focal contact formation on the size of the gap between substrate and cell membrane is still a big mystery. In the 1970s, it was proposed that focal contacts are areas of close proximity between cell membrane and substrate (Gingell and Todd, 1979). This

---

[8] Glass samples coated with a 20 nm layer of Nb_2O_5 were a kind gift of J. Vörös, ETH Zürich. The nanopattern on Nb_2O_5 surfaces was performed following the same steps as for glass samples, with the difference that the surface cleaning prior to dip-coating was performed by an oxygen plasma treatment.

was concluded, since focal contacts appear as dark patches in the reflection interference image, what can be a sign for a small distance between substrate and cell membrane. On the other hand, a dark patch in such images is not necessarily a region of small cell-substrate distance and can also be caused by changes in the refractive index due to optically dense regions in the cell membrane or the cytoplasm. For example, focal contacts are expected to be such optically dense regions.

This view was strongly supported by experiments using fluorescence interference contrast microscopy (FLIC), where no explicit correlation between a membrane deformation and the presence of focal contacts was found. Instead, the distance between cell membrane and substrate was with approximately 48 nm rather homogeneous all over the cell adhesion area (Iwanaga et al., 2001).

A possible way to receive more information about the real origin of the dark appearance of focal contacts in RICM is the usage of two-colour RICM. In our setup, illuminations with light of $\lambda = 436$ nm (blue) and $\lambda = 546$ nm (green) were possible. Since blue light is due to its shorter wavelength more sensitive to variations in the cell-substrate distance than green light, the size of the dark areas is expected to differ significantly for the two wavelengths if the cell membrane was curved.

RICM images from an experiment[9] where focal contacts were studied in blue and green RICM are shown in figure 6.10. To ensure that with our measurements indeed focal contacts are monitored, RICM experiments were supplemented by observing the fluorescence of the YFP labelled paxillin protein, a member of the focal contact plaque.

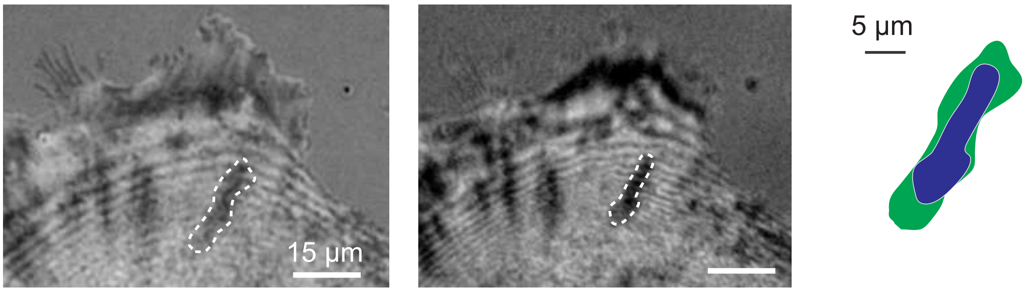

(a) (b) (c)

Figure 6.10: Focal contact areas obtained with RICM for (a) $\lambda = 541$ nm (green) and (b) $\lambda = 436$ nm (blue). In each image, the same focal contact is encircled and (c) shows an enlarged comparison of its area obtained with the two wavelengths. The areas are shown in the respective colour.

As obvious from image 6.10 and table 6.2, a different focal contact size was obtained with the different imaging methods: the focal contact appeared smallest when the fluorescence of paxillin was observed. RICM measurements using $\lambda = 436$ nm led to smaller dark zones than those using $\lambda = 546$ nm, but were on average still slightly larger than the fluorescent areas.

For an interpretation of these data several aspects have to be considered. Firstly, we discuss the RICM signal for a locally decreased gap between substrate and cell mem-

---

[9] The conditions in the experiments presented here were identical to those in 6.3. Images were taken after 4-8 hours of cell adhesion.

Sample	$\lambda = 546$ nm	$\lambda = 436$ nm	Fluorescent Area
28 nm, PLL-PEG	1	0.76 ± 0.12	0.78 ± 0.24
28 nm, mPEG2000-urea	1	0.79 ± 0.06	0.73 ± 0.09
55 nm, PLL-PEG	1	0.67 ± 0.15	0.58 ± 0.13

Table 6.2: Areas of the paxillin fluorescence and of the dark spots measured with two-color RICM and. All areas were normalised to the values measured with green light (546 nm) and then averaged over the analysed cell samples. Focal contacts were analysed on different types of nanopatterned substrates and passivations.

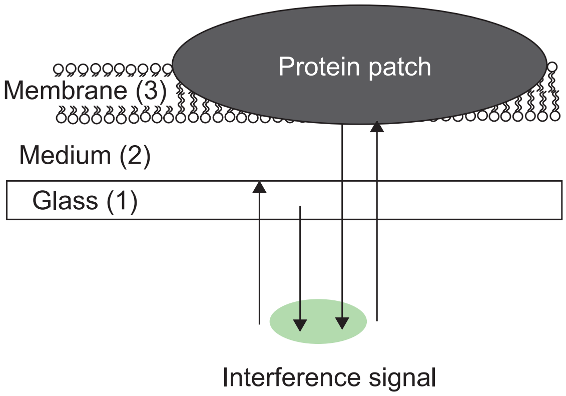

Figure 6.11: Schematic representation of a protein patch incorporated into the membrane. The reflective interfaces between glass and medium (1/2) and medium and cell-membrane (2/3) are shown.

brane. Secondly, we show with a short calculation how a locally increased refractive index affects the RICM signal. The two reflective layers 1/2 (glass/medium) and 2/3 (medium/membrane) taken into consideration for our calculations are shown in figure 6.11.

To demonstrate the effect of a close proximity between cell membrane and substrate, the substrate-membrane distance was modulated as $d(x) = 48\ \text{nm} - (10\ \text{nm}) \exp(-x^2/(20\ \text{nm}^2))$ (figure 6.12 a). With equation 4.1 (section 4.1), the RICM signal was calculated. The refractive indices used here are $n_1 = 1.5$ for glass, n_2=1.33 for the medium and a constant value $n_3 = 1.4$ for the cell membrane (Vörös, 2004). The effect of the height modulation on the RICM signal is presented in figure 6.12 b, where the intensity of the blue RICM signal relative to the green RICM signal is shown. This plot demonstrates, that the intensity of the blue signal is enhanced compared to the green signal in the region of close cell-surface contact. Thus, this region appears smaller in blue RICM than in green RICM. Comparing the RICM data with the situation in figure 6.12 reveals that the experimentally obtained difference between the size of focal contacts in blue and green RICM qualitatively agrees with this calculation.

A similar calculation can be performed for the influence of changes in the refractive index. The influence of the refractive index on the interference pattern is caused by changes in the intensities which are reflected at each of the reflective interfaces. The reflected intensities $I_{i/j}$ at the interfaces 1/2 and 2/3 can be calculated from the Fresnel equations

$$I_{i/j} = I_k (\frac{n_i - n_j}{n_i + n_j})^2,$$

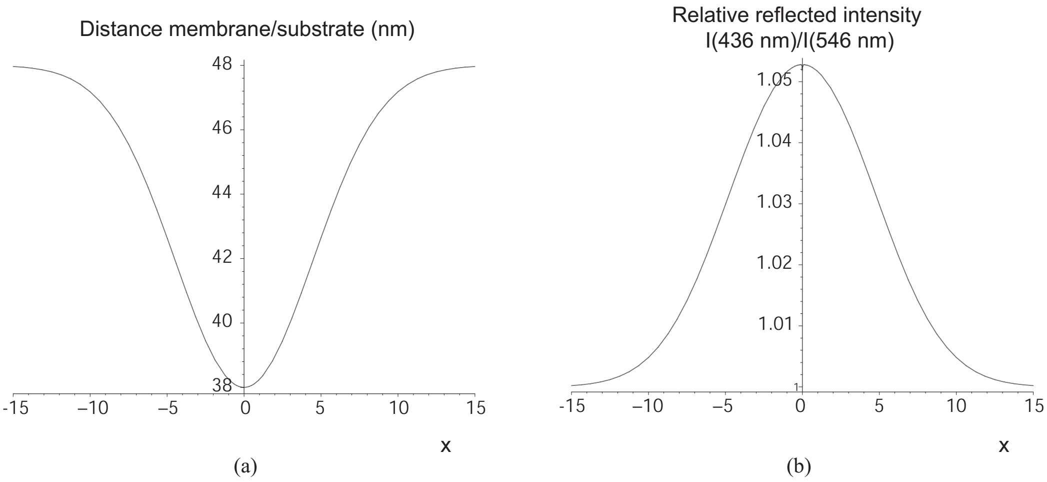

(a) (b)

Figure 6.12: (a) Decrease of the gap between cell membrane and surface according to $d(x) = 48\text{ nm} - (10\text{ nm})\exp(-x^2/40)$. (b) Relative RICM intensity for blue light compared to green light, I(436 nm)/I(546 nm).

where I_k is the intensity illuminating the boundary between layer i and layer j. In the particular example regarded here, the refractive index $n_3 \approx 1.4$ of the membrane was modulated around $x = 0$ with $n(x) = 1.4 + 0.05\exp(-x^2/40)$ to simulate the refractive index of the optically dense protein patch. The parameters used to obtain the RICM interference signal were $n_1 = 1.5$ and $n_2 = 1.33$ for glass and medium, respectively, and the distance between glass and membrane was set to be constant at $d = 48$ nm. Figure 6.13 b shows the change in the RICM intensity around $x = 0$ as a result of the refractive index modulation plotted in figure 6.13 a. This image makes clear, that in the situation regarded here the green RICM signal is enhanced compared to the blue signal, thus the area of the optically dense region turns out to be smaller in green RICM than in blue RICM.

This analysis demonstrates that for a distance of membrane and substrate of d=48 nm, as proposed by Iwanaga et al. (2001) and used for our calculation, the appearance of focal contacts as dark zones in RICM cannot be due to an increase of the refractive index in the focal contact area. Of course, a comparison of experimentally obtained RICM signals with calculated intensities bears many uncertainties. For example, it is not clear what the true refractive indices in a focal contact are and if the reflective layers chosen for the analysis are correct.

With this background information at hand, our experimental data can be explained in two ways: either there is a close gap between substrate and cell membrane in the focal contact zone or the focal contact patch itself carries a certain curvature. This might be of importance, since the refractive index of the dense focal contact protein patch is expected to be larger than that of the membrane and the reflection of light at the protein patch might play the major role. However, as shown in figure 6.14, SEM images taken by M. Arnold (2005) revealed a distinct membrane deformation of the cell membrane towards single integrin binding sites for cells adhering to biofunctionalised nanopatterns. Hence, a deformation of the membrane in focal contacts cannot be fully excluded, especially when adhesion is studied on nanopatterns. A possible artefact in the results of the above

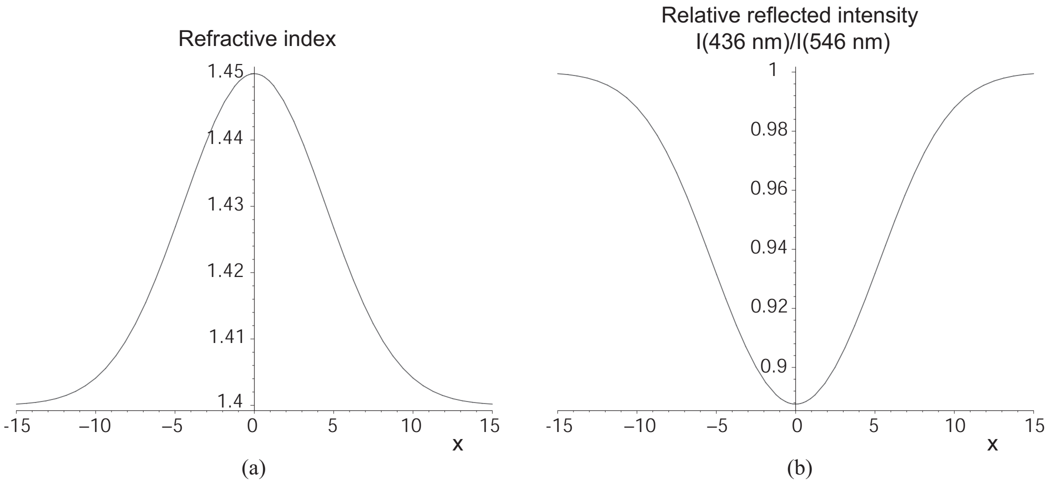

(a) (b)

Figure 6.13: (a) Local increase of the membrane refractive index modelled with $n_3(x) = 1.4 + 0.05\exp(-x^2/40)$. (b) Relative RICM intensity for blue light compared to green light, I(436 nm)/I(546 nm). The distance of membrane and surface was set to be constant at d=48 nm.

mentioned study by Iwanaga et al. (2001) could be their usage of ECM protein-coated surfaces. For example, the fibronectin is known to be rearranged by the cells to 20-25 nm thick fibres (Pompe et al., 2005) and such a fibronectin spacer could account for a large part of the measured cell-substrate gap of 48 nm. A future project, where cell adhesion on a nanopatterned silicon oxide substrate will be investigated with FLIC, should reveal whether fibres of ECM proteins are responsible for the observed large cell-substrate distances and if biofunctionalised nanopatterns are able to close this gap.

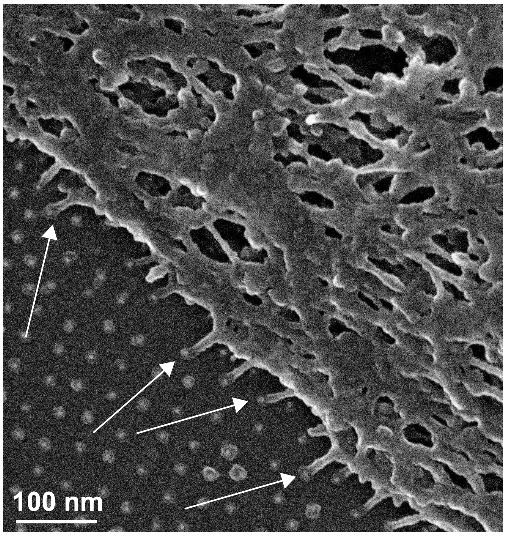

Figure 6.14: 40° angle tilt scanning electron micrograph of REF 52 cells plated for 24 hours on functionalised nanopatterns with 58 nm integrin binding site distance. The arrows indicate the regions of close contact between gold dots and cell membrane (from Arnold (2005)).

Part IV

Force Experiments with Live Cells

7 Initial Adhesion

Initial adhesion studies investigate the adhesion process during the first seconds and several minutes of cell-substrate contact. At this timescale, adhesion is dominated by glycocalix-mediated interactions and the binding of single receptor-ligand pairs, before early molecular clusters form. While many previous biophysical studies of integrin mediated adhesion are focused on the manifold properties of long-term cell adhesion and focal contacts (Vogel and Sheetz, 2006), little is known about the detailed mechanisms of initial integrin-mediated cell adhesion.

A possible method to quantifying initial adhesion is to study the molecular interactions between cells and surfaces. In the experiments presented here, cell-substrate interaction forces were measured both with magnetic tweezers and AFM. However, not only specific molecular interactions, but also the viscoelastic response of cells and nonspecific cell-substrate interactions can be detected in such experiments. This is the subject of the first two sections in this chapter. The subsequent sections address the transition from single molecule to molecular cluster mediated adhesion and discuss the impact of the results on the picture of early adhesion clusters.

7.1 Viscoelastic Cell Response

Viscoelasticity describes the time-dependent elasticity of materials and is a fundamental concept in cell mechanics. Viewed from a biological perspective, an understanding of the short-term viscoelastic cell behaviour is desirable, since it can provide deeper knowledge on the effect of diseases such as malaria and cancer (Wottawah et al., 2005; Suresh, 2006).

7.1.1 Viscoelastic Models

The two functions characterizing viscoelastic properties are the creep and the relaxation function. The creep function $J(t)$ describes the development of the material strain during the application of a constant stress. On the other hand, the relaxation function describes changes in the tensile or compressive stress, while a constant strain is applied. In several studies on cell viscoelasticity, the so-called Kelvin model or its extended version have been used for data interpretation (Thoumine et al., 1999; Fernández et al., 2006; Bausch et al., 1999; Fung, 1981). All such linear viscoelastic models describe the mechanical properties of cells in terms of combinations of elastic and viscous elements, represented by springs and dashpots. For springs the applied stress is proportional to the strain, for dashpots the stress is proportional to the strain rate. In combinations of springs and dashpots, the stress is partitioned in a time-dependent manner between the constituent elements (Courtney, 1990). A sketch showing the combinations of mechanical elements for the Kelvin and the extended Kelvin model is given in figures 7.1 a and b. The creep function of both models contains an exponential decay of the strain with time, as summarised in table 7.1.

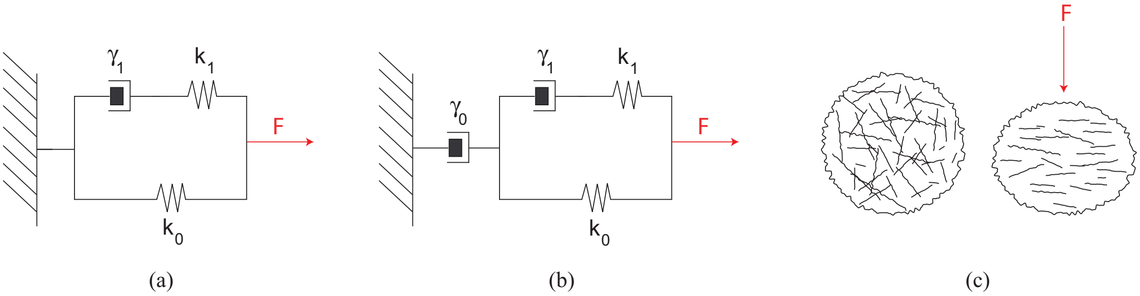

Figure 7.1: Configuration of dashpots γ_i and springs k_i for (a) the Kelvin model and (b) the extended Kelvin model. (c) shows the deformation of a cell using a glassy description, where the polymeric cell interior is suggested to be reorganised as a result of the applied force.

During recent years a different approach was followed by describing the cell as a soft, glassy material. This treatment presumes that cell mechanics is dominated by structural disorder, metastability, and rearrangements (Desprat et al., 2005; Fabry et al., 2001). A sketch of such a situation is given in figure 7.1 c. According to this picture, the creep function shows a power law time dependence (see table 7.1).

Model	**Creep Function** $J(t)$
Kelvin body	$\frac{1}{k_0}(1-\frac{k_1}{k_0+k_1}e^{-t/\tau})$
Extended Kelvin body	$\frac{1}{k_0}(1-\frac{k_1}{k_0+k_1}e^{-t/\tau})+\frac{t}{\gamma_0}$
Glass-like body	At^{α}

Table 7.1: Comparison of creep functions $J(t) = x(t)/F$ with $x(t)$ the cell deformation and F the applied force. The k_i denote the spring constants and τ is the decay parameter of the exponential, which is a function of the k_i and the viscosities γ_i. A and $\alpha \leq 1$ are parameters describing the behaviour of a glassy material, according to Desprat et al. (2005).

So far, only for certain experimental situations viscoelastic models have been well-established. For example, the Kelvin-model and the glassy power-law description are often favoured if cells are well-adhered at two opposing surfaces in micromanipulation devices (Fernández et al., 2006; Desprat et al., 2005). In contrast to this, optical stretcher experiments, where cells are probed in suspension, are usually interpreted in terms of a viscoelastic shell-model (Wottawah et al., 2005). This emphasises that a general description of cell viscoelasticity is still missing and in each particular case the viscoelastic model is adapted to the experimental data.

7.1.2 Cell Experiments and their Interpretation

In order to study the creep behaviour of cells, AFM data, which were originally intended to study only the cell-substrate interaction, were additionally analysed with respect to the viscoelastic cell creep. In our experiments, a spherical cell was pressed onto a substrate

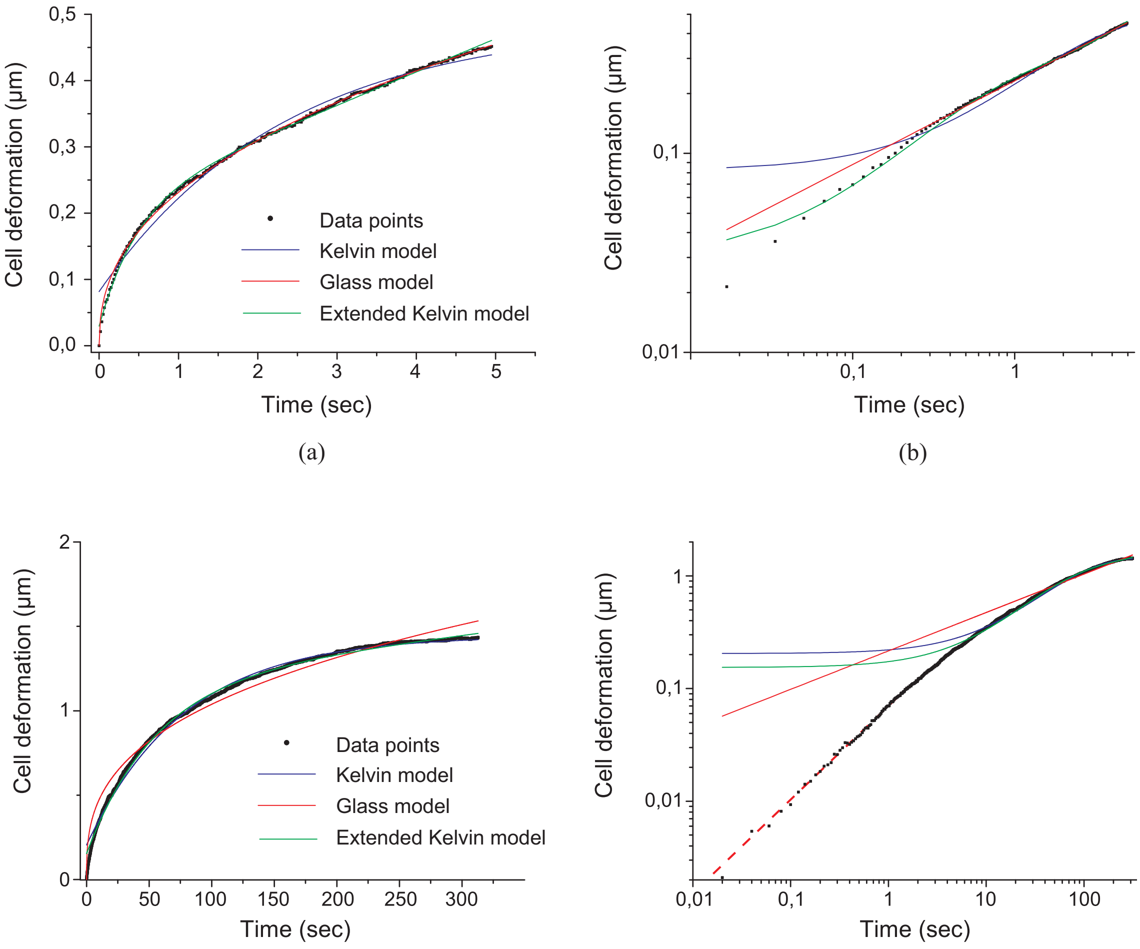

(a) (b)

(c) (d)

Figure 7.2: Creep function of a spherical cell in a linear and a double-logarithmic plot fitted with the Kelvin, the extended-Kelvin and the power-law model. In (a) and (b) F=2 nN, Δt= 5 sec. In (c) and (d) a different cell experiment with F=0.4 nN, Δt= 300 sec is shown. The red, dashed line in (d) marks the power law behaviour of the initial creep data.

with a constant force and the creep response of the cell was recorded for the time of cell-substrate contact.

Figures 7.2 a and b show a cell creep response for a spherical cell[1], which was pressed onto a passivated substrate with a force of 2 nN for five seconds both in a linear and a double-logarithmic plot. In these graphs, data approximations with the Kelvin, the extended Kelvin and the glassy power-law model are added. The double-logarithmic plot shows that the quality of the fit, especially in the initial creep, is best for the power-law and the extended Kelvin-model, although the latter ranks slightly behind in a comparison of the coefficients of determination (power law: $R^2 = 0.99824$; extended Kelvin: $R^2 =$

---

[1] Experimental conditions: Cells (REF YFP Pax) were trypsinised from cell cultures dishes, resuspended with CO_2 independent medium (2 % FBS, 2 % L-glutamin, 100 µg/ml penicillin-streptomycin) and kept at 36 °C in this medium throughout the experiment. Cells were immobilised at the cantilever by concanavalin A and left to recover for at least 15 min after their immobilisation at the cantilever. For a detailed description of the cell immobilisation procedure see section 4.3.4 and the appendix.

0.99812). The standard Kelvin model strongly deviates from the data (R^2 = 0.98569), especially for time points smaller than one second. Graphs 7.2 c and d present data for an extended observation time of 300 seconds and a force of 0.4 nN pressing a cell onto a functionalised nanopattern (70 nm integrin binding site spacing). No striking difference for the viscoelastic cell behaviour between different substrate functionalisations was observed, which is probably due to the relatively short cell-substrate contact times. Figure 7.2 c demonstrates that the Kelvin and the extended Kelvin model fit our data best in the long-term creep behaviour (power law: R^2 = 0.97062; extended Kelvin: R^2 = 0.99685; Kelvin: R^2 = 0.99457). The double-logarithmic plot in figure 7.2 d clearly shows the problems of all models to satisfy both the initial and the long-term creep phases, although the data follow a power law in the initial creep phase for timescales smaller than one second (dashed line). Such short-time effects could be revealed because our experiments deal with much shorter timescales than most of the studies reported in literature and are with a possible temporal resolution of less than 15 milliseconds extremely time sensitive.

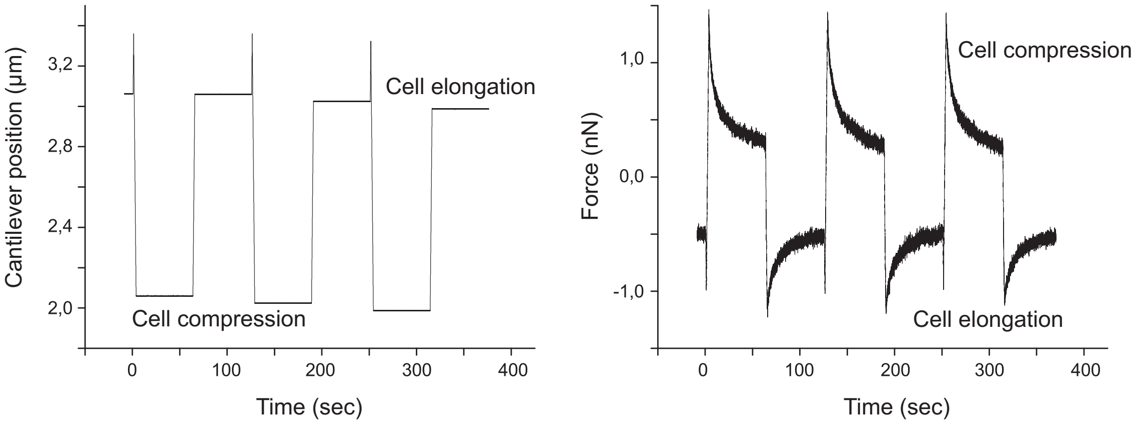

(a) (b)

Figure 7.3: Repeated force relaxation curves for a cell which is either compressed or tensed by a cantilever. (a) shows the cantilever position for the force relaxation processes plotted in (b).

A reason why the power-law model fits so well for short timescales might lay in the disordered polymer network inside a spherical cell, which could undergo orientational changes due to the application of an external force. At that stage no distinct network of cytoskeletal fibres has formed yet, in contrast to the situation for well-spread cells in other experiments (Fernández et al., 2006). The disorder inside well-spread cells is expected to be much smaller, thus structural reorganisations due to the application of a force might play a minor role. Desprat et al. (2005) argued that the power law behaviour of the cell creep could be a consequence of a continuous distribution of relaxation time constants in a cell, which cannot be described in terms of a finite number of linear viscoelastic elements.

Figure 7.3 presents the force relaxation behaviour of a cell pressed repeatedly onto a PLL-g-PEG substrate. Figure 7.3 a shows the cantilever position, figure 7.3 b the force relaxation. The high reproducibility of the cell's viscoelastic behaviour is obvious. When the cell is elongated, the (negative) force on the cantilever relaxes to a smaller absolute value. The force was given a negative sign because the cantilever is deformed in the -z direction. A similar relaxation occurs, when the cell is compressed, but then the force has a positive sign due to the cantilever bending in +z direction.

Our first approaches to explain the viscoelastic behaviour of the cell system showed discrepancies to conventional descriptions of cell viscoelasticity, proving that the mechanics of single cells still bears many open questions. The presented data should motivate future AFM based work on the nature and origin of viscoelasticity for single, spherical cells.

7.2 Interaction Forces of Cells with Passivated Substrates

Apart from studying the specific interactions of cells with nanopatterned substrates, also the nonspecific adhesion of cells to the PEG passivation was characterised. In this study, we quantified the interaction of cells with the two available PEG passivations, the PLL-g-PEG and the mPEG2000-urea. The data discussed in the following were measured after pressing a cell onto a substrate for five seconds with a defined, constant force. The cells were detached from the substrate with a cantilever retraction speed of 5 µm/sec and the force associated with the detachment was recorded. After each detachment the cell was allowed to relax for several seconds[2].

Figure 7.4 shows the adhesion forces of cells to PLL-g-PEG and mPEG2000-urea passivated substrates[3] for different regimes of load. For both kinds of passivation the adhesion forces increase with growing load and for all load regimes the adhesion forces on the PLL-g-PEG are smaller than on the mPEG2000-urea.

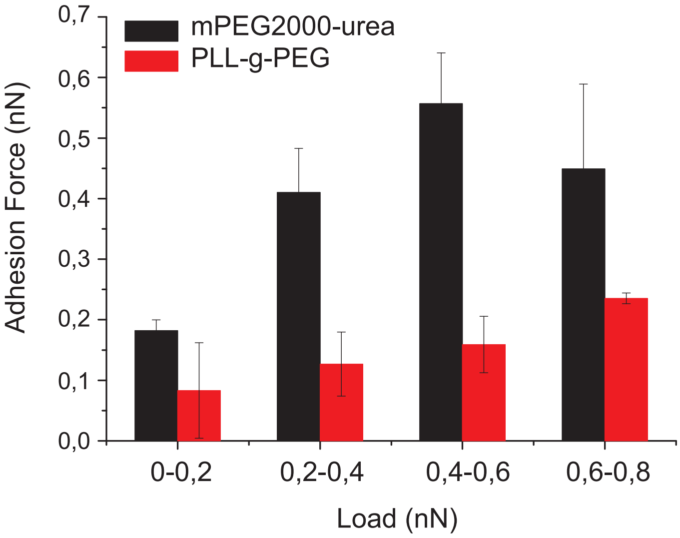

Figure 7.4: Comparison of cell-substrate interaction forces for PLL-g-PEG and mPEG2000-urea coated surfaces. Each bar comprises average values for a load interval of 0.2 nN. The error bars refer to standard deviations.

Figure 7.5 shows the strong increase in interaction forces between a cell and a mPEG2000-urea substrate when the load is raised into the nanonewton regime. In this example, the load was increased in steps until values of more than 5 nN were reached (black squares). Subsequently, the experiments were repeated with a reduced load of 2-3 nN

---

[2] The experimental conditions were identical to those given in section 7.1, see page 81.

[3] mPEG-urea substrates were kindly provided by I. Slizskaia for this experiment.

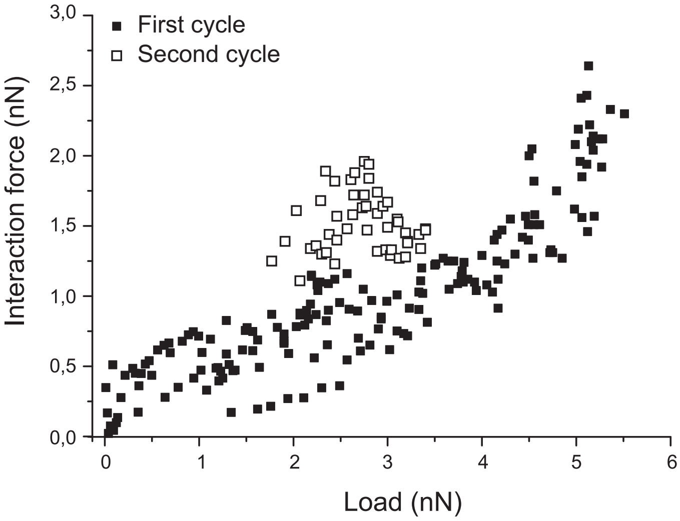

Figure 7.5: Dependence of adhesion forces between a cell and a mPEG2000-urea surface on the load. The load was applied to the cell for 5 seconds. Full squares: Force measurement at stepwise increasing load. Empty squares: Force measurements for intermediate loads, after the first cycle of the experiment was finished.

(empty squares). Strikingly, the interaction forces for a load of 2-3 nN are significantly increased in the second cycle of the experiment. This indicates a deformation of the cell by large loads, and thus an enlargement of the cell-substrate interaction zone in the second cycle of the experiment. Damage to the passivated surface during the experiments was excluded by probing different surface spots. To avoid cell deformation, a load of much less than 1 nN was applied in all cell detachment experiments shown in the subsequent sections. Additionally, the cell was extensively allowed to relax in between single experiments.

It is not yet possible to give a precise quantitative interpretation of the adhesion forces shown in figure 7.5. Adhesion forces depend strongly on the size of the cell-substrate contact zone, which is for the short cell-substrate contact time of 5 seconds still dominated by the viscoelastic cell creep and not only controlled through the applied load. So far, the cell-substrate contact area could not be determined in such experiments, thus a further interpretation of the dependence of adhesion forces on load would be speculative.

From figure 7.5 it follows that the values for the extrapolated interaction forces for mPEG2000-urea at zero load ($F \approx 100 - 200$ pN) do not agree with the ones measured with magnetic tweezers. There, a much smaller value for the cell interaction force with mPEG2000-urea of approximately 2.5 pN was obtained. This discrepancy is assumed to result from the invasive character of AFM, where the cell is actively pressed onto the substrate. This leads to an artificially induced increase in the cell-substrate interaction area, which is not the case in the less invasive magnetic tweezers experiments. Consequently, cell detachment forces measured with AFM and magnetic tweezers can in general only be compared qualitatively, but not quantitatively.

7.3 Single Molecule Interactions

Single molecule interactions between cell adhesion receptors and their respective ligands have attracted substantial interest during the last decade. Most of such studies involved transmembrane proteins, which are difficult to extract from the cell membrane without damage. Therefore experiments are often performed by directly using living cells. Early approaches on integrin-mediated adhesion were performed by Lehenkari and Horton (1999), where they immobilised RGD ligands at an AFM cantilever and measured its interaction with the integrins in the cell membrane. In order to study protein-mediated interactions between two cells, Benoit et al. (2000) performed force experiments where one cell was immobilised at the AFM cantilever, the other at the substrate.

Studying single molecule interactions was not the main focus of this thesis, but every force curve from a single cell detachment process bears the significant force steps, which are attributed to the breakage of bonds between the surface bound RGD peptide and the integrin $\alpha_V\beta_3$ receptor in the cell membrane. Thus, the measured force curves were also analysed with respect to single molecule events. The principle of how single molecule unbinding is manifested in a force curve is described in section 4.3.4 above and here only the results of the analysis are given.

To verify the involvement of the integrin/RGD bond in the binding process, cells were incubated in an 1x PBS solution containing linear RGD (G1269, Sigma-Aldrich) for 30 minutes. This PBS solution was also used for the force experiments. A 350 µM RGD solution blocked most of the force steps, a 2.8 mM solution finally prevented all specific binding events. Despite this proof of specificity for the cell-substrate binding, small bond breakages between cellular polysaccharides and the con A proteins at the cantilever during cell detachment cannot be excluded per se. However, it was never observed that the cell-cantilever contact broke during our experiments, indicating that the majority of the measured force steps is indeed a result of the breakage of RGD/integrin bonds.

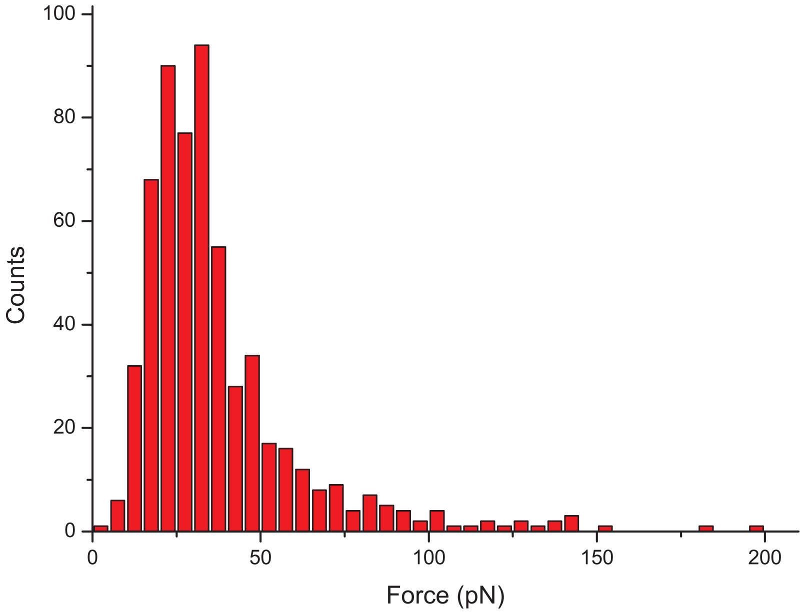

Figure 7.6: Distribution of rupture forces for the integrin $\alpha_V\beta_3$/RGD bond.

Figure 7.6 shows the distribution of rupture forces for the RGD/integrin $\alpha_V\beta_3$ bond. In this experiment, the RGD was covalently coupled to a homogeneous gold surface via a 5 nm long PEG-thiol linker[4]. The cell was brought into contact with the substrate for 5 seconds before it was retracted with a speed of 5 µm/sec[5]. Due to the stochastic nature of single bond rupture, the measured rupture forces follow a probability distribution that is defined by the energy landscape of the bond and by the bond loading rate r. From several experiments, the most frequent rupture force of the RGD/integrin $\alpha_V\beta_3$ bond was determined to be $F_{sm} = (32 \pm 24)$ pN, the error denotes the width of the maximum of the force distribution. The obtained value for the rupture force is comparable to that reported for the fibronectin/integrin complex in recent studies (Li et al., 2003a; Puech et al., 2005). The asymmetry of the force distribution, as evident from figure 7.6, is suggested to be enhanced by the simultaneous rupture of multiple bonds. Such events cannot be distinguished from single bond ruptures and lead to limitations for a precise loading rate analysis, since it is not known among how many bonds the applied load is actually distributed. For excluding such multiple binding events, the cell-substrate contact time should be reduced to less than 1 second. In our study, loading rates were determined by analysing the slopes of the force curves prior to single rupture events and the obtained loading rates ranged from less than 1 to 400 pN/sec. We observed that rupture forces tend to increase with increasing loading rate, but a distinct conclusion on the precise loading rate dependency and thus the shape of the binding potential cannot be drawn for the RGD/integrin $\alpha_V\beta_3$ interaction so far. No measurable deviations in the single molecule rupture force F_{sm} were found when the length of the RGD peptide was modified to 2 nm and 7.5 nm, respectively.

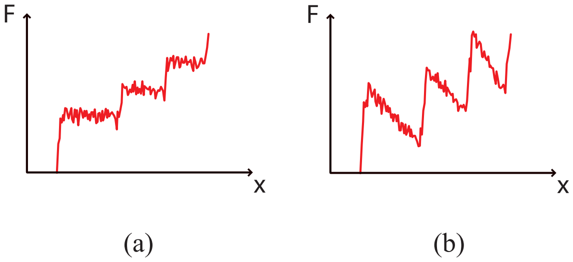

(a) (b)

Figure 7.7: (a) Extraction of viscous tethers during cell detachment, apparent through flat regions prior to rupture events. (b) Saw-tooth pattern in the force curve, indicating the elastic response of the bonds before they rupture.

A striking feature of force curves taken in initial adhesion experiments are shorter or longer viscous regions prior to rupture events. This is in contrast to the assumption that a bond should be stretched elastically when subject to an external force (see figure 7.7). The appearance of viscous effects is attributed to be a result of the formation of thin membrane tubes, the so-called tethers. These tethers are assumed to form when the cell body is retracted and the bonds to the surface are still intact. In such a situation, the membrane can flow viscously into the contact zone without any resistance, comparable to the fibres pulled out from a sticking chewing gum (Benoit and Gaub, 2002; Benoit, 2000). Thus, the tether membrane applies a constant, nonzero force to the enclosed bonds and

---

[4] Normally, the RGD peptide, as used in this study, has a 2 nm long linker, see section 3.3.1.

[5] The experimental conditions are identical to those given in section 7.1, page 81.

represents a cell-internal “force clamp”. When a tether breaks, the force is released and the length of the tether can be related to the lifetime of the enclosed bond or bonds.

According to Bayas et al. (2006), the probability density function for a bond rupture between times t and $t + dt$ is described by an exponential decay

$$p(t) = k \exp(-kt), \tag{7.1}$$

where k is the dissociation rate constant $k = k_0 e^f$ with $f = F/F_0 = F x_B / k_B T$ the dimensionless force and k_0 the dissociation rate constant in the absence of force. From the probability of bond breakage, the probability of bond survival up to time t can be derived and is

$$S(t) = \exp(-kt). \tag{7.2}$$

An example for a distribution bond lifetimes is shown in figure 7.8, where an approximation of the data with equation 7.2 is included.

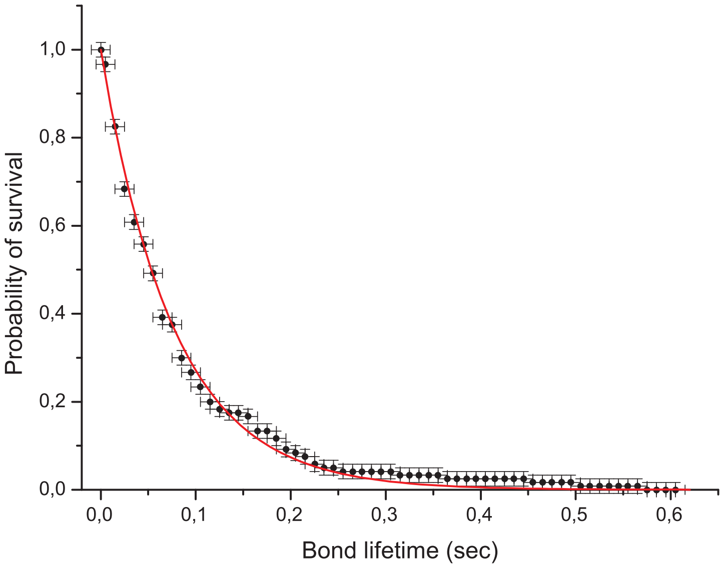

Figure 7.8: Survival probability of integrin/RGD bonds, measured on a nanopattern with $d_{site} = (35 \pm 6)$ nm. The red curve shows an approximation using equation 7.2, which gave $k = (13.0 \pm 0.2)\,\text{sec}^{-1}$.

The criterion used for picking a pure membrane tether event was a flat region in the force curve prior to bond rupture, where the average loading rate should not exceed 1 pN/sec. An approximation of our data with equation 7.2 revealed $k = (13.0 \pm 0.2)\,\text{sec}^{-1}$. A similar approach using a biomembrane force probe as a force clamp was reported recently for the cadherin-cadherin bond (Bayas et al., 2006). There, the measured dissociation rate constants are of the same order of magnitude as the values measured in this study. This motivates that the tethers can serve as a cellular force clamp system and are indeed capable of providing useful information on the lifetime of single molecules. Up to now only little information on the real nature of the tethers formed in the cell-substrate contact zone has been retrieved. Moreover, these presumably very thin tethers have never been detected optically. Many open questions remain to be solved in future experiments, for example, how many bonds are enclosed inside a tether and how membrane stiffness affects tether formation.

7.4 Adhesion Cluster Formation

Focal contact formation and cell spreading are strongly influenced by the distance of integrin binding sites (Arnold et al., 2004; Cavalcanti-Adam et al., 2006). An important question left open by these previous studies is, at what timescale variations in integrin binding site spacing start to affect cell adhesion and to what extent this influences cell adhesion strength. In order to answer this question, a characterisation of interaction forces between cells and nanopatterns can provide important information. High-resolution force measurements should be able to resolve cooperative integrin interactions already during the first minutes of adhesion, thus long before conventional optical techniques are capable of detecting adhesion clusters.

In this work, the first ten minutes of adhesion were investigated with magnetic tweezers[6] and AFM experiments. The results of these studies, including a model for initial adhesion cluster formation, are presented in the following.

7.4.1 Magnetic Tweezers Studies

For measuring cell detachment forces[7], vertical forces were exerted with a magnetic tweezers device, as described in section 5.1.

The lateral inter-particle spacing d of the nanopatterns used for this study ranged from 58 nm to 145 nm (± 10 %) and single gold dots had a diameter of (6 ± 1) nm (for preparation issues see section 3.1). On the nanopatterns, nonspecific protein attachment was prevented by covalently coupling mPEG2000-urea to the substrate, as described in section 3.2.1. The gold dots are biofunctionalised with an RGD peptide according to the procedure given in section 3.3.1. The small size of the nanoparticles prevents the binding of more than one $\alpha_V\beta_3$ integrin per particle (Glass et al., 2003; Arnold et al., 2004), hence the position of integrin binding sites is identified with the position of gold nanodots in the following. The cells used for the experiments were REF 52 wt fibroblasts. In order to apply forces to cells, epoxy-terminated magnetic beads were covalently attached to the cell envelope and these beads transduced the magnetic force to the cell-surface contact zone.[8]. For the experiments, only cells that carried a single bead were used. Reflection interference contrast microscopy (RICM) was employed to observe the detachment of the cell from the surface. Figures 7.9 a and b show images of a cell prior to its detachment in bright-field microscopy and RICM, respectively. After cell detachment, no cell-surface contact area is observed with RICM, since the interference signal from the cell membrane has completely disappeared (see figure 7.9 c).

---

[6] Magnetic tweezers experiments were performed in collaboration with Nadine Walter. The results are published in Walter et al. (2006).

[7] In the following the term *cell detachment forces* or *unbinding force* is used instead of *cell adhesion forces*. This convention was introduced since in adhesion cluster formation active processes are involved. Particularly, effects like the formation of tethers or anisotropic force distributions at the cell-surface interaction zone can lead to discrepancies between the real adhesion forces and the measured detachment forces.

[8] For the coupling of magnetic beads (M450 Expoy, Dynal, Norway) to amino groups in the cell envelope, cells were trypsinised, suspended in PBS and the magnetic beads were added. After 2 minutes of incubation the cells were centrifuged and the PBS was replaced by DMEM supplemented with 1 % FBS. This cell suspension was used within one hour to avoid endocytosis of the magnetic beads. Magnetic tweezer experiments were performed at 37 °C and 5 % CO_2 in DMEM containing 1 % FBS and 1 % L-glutamine.

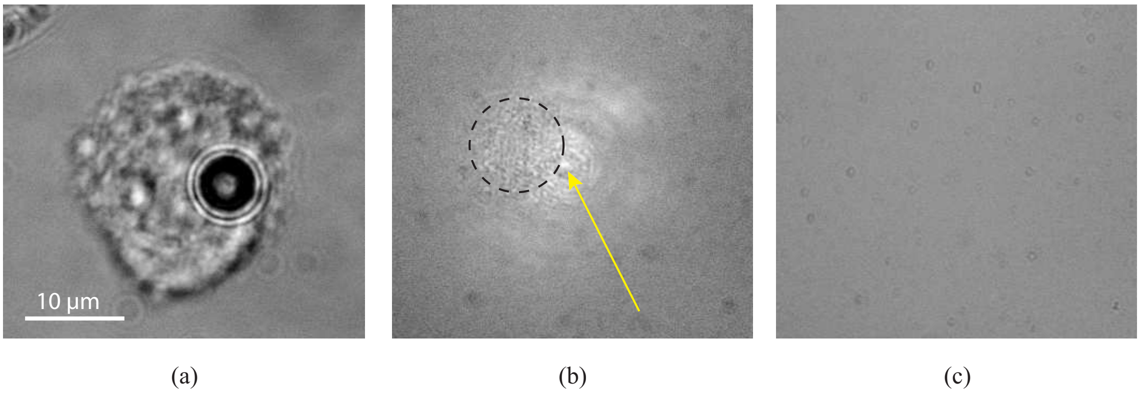

(a) (b) (c)

Figure 7.9: Different stages in a magnetic tweezers experiment. A cell adhering to a substrate is detached by a magnetic force, which is applied to a cell-bound paramagnetic bead. (a) An adhering cell which is carrying a magnetic bead in bright-field microscopy. (b) The same cell in RICM, where the contact area is encircled and the magnetic bead is marked with an arrow. (c) RICM image of the same surface region after cell detachment.

In order to induce cell detachment, the applied magnetic force was raised every 5 seconds by (3 ± 1) pN for forces lower than 20 pN, and by (7 ± 1) pN for forces above 20 pN, up to a maximum force of 200 pN. At least five measurements were performed on each type of substrate. The accuracy of the force measurements was limited by the applied force steps, a retarded cell detachment was never observed while the force was held at a constant value. Instead, the cells detached directly after the magnetic force was raised. The bead-cell coupling was very tight, since a detachment of beads from the cell envelope was never observed.

Figure 7.10 shows cell detachment forces for RGD nanopatterns with integrin binding site spacings of $d = 58$, 69, 93, 120 and 145 nm. To verify specific integrin binding to the RGD ligands and to quantify nonspecific cell-substrate interactions, control experiments on non-nanostructured as well as on RGD-free nanopatterns were performed. The upper limit of these interaction forces is (2.5 ± 1) pN, which is negligible compared to the specific integrin-mediated forces (see section 7.3). Hence, the measured cell detachment forces are attributed to specific interactions between the integrins in the cell membrane and the RGD peptides on the surface. The data in figure 7.10 show a strong increase of the cell detachment forces with decreasing integrin binding site spacing and increasing binding site density, respectively. For each distance of integrin binding sites, the cell detachment forces scatter. For large integrin binding site spacings, d=145 nm and d=120 nm, the distribution of unbinding forces is narrow and the magnitude of the measured forces is comparable to that of single molecule rupture events, as discussed in section 7.3. For small binding site spacings, the force distribution is broad and unbinding forces increase strongly with the density of integrin binding sites. The magnitude of these detachment forces indicates that several bonds are involved in the unbinding process. For a nanopattern with $d = 69$ nm, the data vary between a few and more than 200 pN in different experiments. As the force applicable by the magnetic tweezers is restricted to 200 pN, it was never possible to detach cells from a nanopattern with $d = 58$ nm.

Additionally to being due to the statistical nature of biological bonds, the broad distribution of unbinding forces can be a result of the strong time dependence of the adhesion

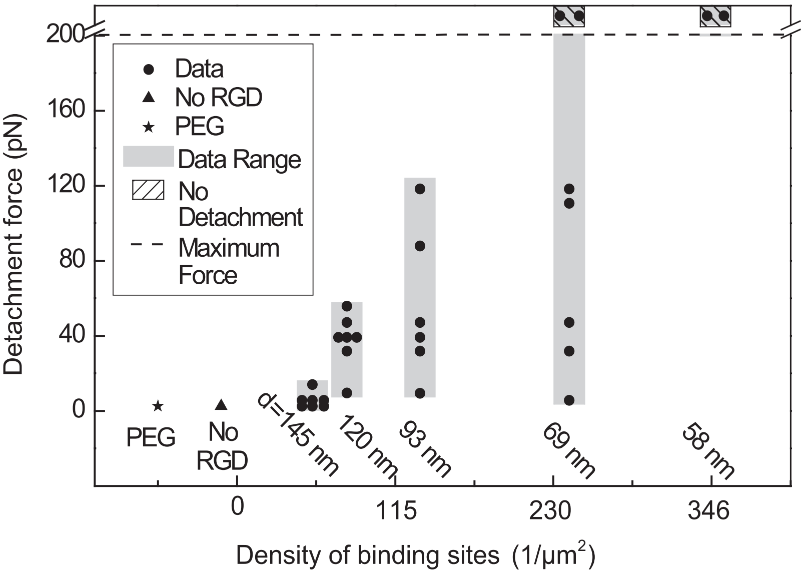

Figure 7.10: Detachment forces of cells that were allowed to adhere for (5 ± 2) min on substrates with binding site spacings from d=58 nm to d=145 nm are shown as a function of the density of integrin binding sites. Data of control experiments on pure PEG and on non-RGD-functionalised nanopatterns (no RGD) are added. The dashed line in the force axis marks the maximum applicable force of 200 pN.

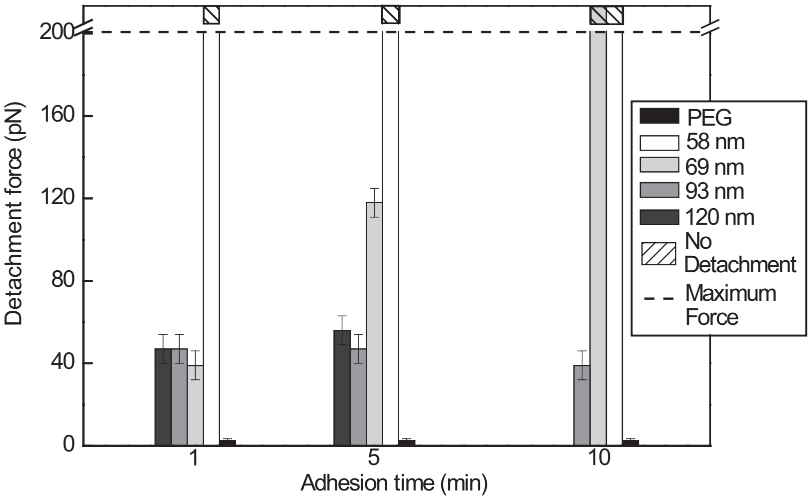

Figure 7.11: Time dependence of cell detachment forces. For each nanopattern a single cell was allowed to adhere for 1, 5, and 10 min on the surface. A strong time dependence can be observed for a nanopattern distance of d=69 nm, suggesting that cell adhesion is activated by this pattern.

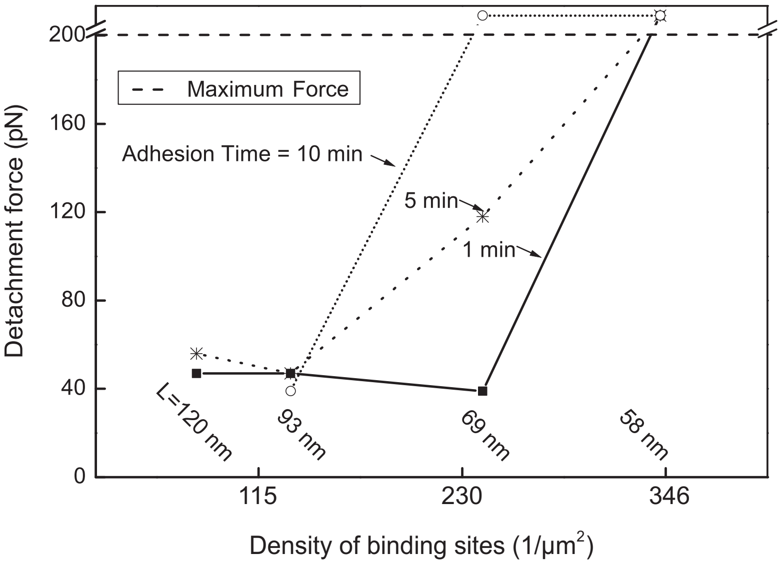

Figure 7.12: Cell detachment force versus the density of integrin binding sites for different adhesion times. A nonlinear behaviour is observed for the development of detachment forces with adhesion time on different nanopatterns, which is a first sign of cooperative integrin binding for $d \leq 69$ nm.

process. In our experiments, the adhesion time could only be determined with an uncertainty of ± 2 minutes because the time a cell needed to touch down onto the substrate varied with each cell. An additional retardation was caused by difficulties in grabbing individual cells with the magnetic tweezers. The effects of different cell-substrate contact times were analysed by using one single cell for repeated detachment cycles. In such experiments, the adhesion time in between the cell detachment events was determined exactly. This allowed the time dependence of cell adhesion strength on different nanopatterns to be evaluated. Figure 7.11 shows data for such measurements, where adhesion times of 1, 5 and 10 minutes were probed on different nanopatterns and on a PEG substrate, respectively. As expected, the cell's interactions with the PEG surface turned out to be time-independent, since adhesion is fully prevented. For cells adhering on substrates where integrin binding sites are separated by 120 and 93 nm, the cell detachment forces were also time-independent and values of around 40 pN were measured. For nanopatterns with d=69 nm, the cell detachment forces increased significantly with time and after 10 minutes the cell could not be detached any more. On the nanopattern with d=58 nm, the cells adhered to the substrate with an interaction force of more than 200 pN already after one minute of cell-substrate contact, thus they could never be detached.

These observations coincide with the distribution of detachment forces presented in figure 7.10. Cells respond to certain integrin binding site spacings by strengthening adhesion with time, thus the variations in cell-substrate contact time of ±2 min can explain the broad distribution of unbinding forces for small integrin binding site spacings. To further demonstrate the effect of cell-substrate contact time on different nanopatterns, figure 7.12 shows the detachment forces versus binding site density for 1, 5 and 10 minutes of cell-substrate contact. Only for nanopatterns with d=69 nm adhesion time plays a crucial role. This is in agreement with the recent observation that cell spreading and focal contact formation are restricted for a binding site separation larger than 73 nm, whereas a separation of 58 nm does not obstruct cell adhesion (Arnold et al., 2004). The data presented here clearly demonstrate the dependence of cell adhesion activity on integrin binding site density and they let us suggest that adhesion associated protein clustering is relevant already during the first minutes of adhesion.

7.4.2 AFM Studies

While force limitations and a low temporal resolution restrict the scope of magnetic tweezers applications, these problems do not occur in AFM experiments. There, forces up to the micronewton regime can be exerted and the cell-substrate contact time is precisely defined with a resolution of several milliseconds. The goal of performing initial adhesion experiments with AFM was to receive detailed information on how the interaction strength depends on the cell-substrate contact time and how adhesion strength is influenced by integrin binding site spacings smaller than 69 nm, which was the limit in the magnetic tweezers experiments.

In the experiments presented here, the preparatory work and the experimental conditions were identical to those given in section 7.1, page 81. Homogeneously biofunctionalised substrates and RGD nanopatterns were prepared according to the procedures given in section 3.1 and in the appendix. The passivation of the substrates was performed with PLL-g-PEG. For measuring cell detachment forces, soft tipless cantilevers with a force constant between 0.03 and 0.3 N/m were used, which led to a force resolution in the piconewton regime. When “fishing” a cell from the suspension, special attention was paid at immobilizing the cell at the tip of the free end of the cantilever in order to avoid force recalibrations (compare section 4.3.3). In order to induce cell-substrate adhesion, a cell was pressed to the substrate with a force of 300-600 pN for up to 5 minutes before it was retracted with a velocity of 5 µm/sec. Artefacts caused by surface defects were avoided by probing several surface spots in each experiment. A detachment of gold dots from the surface is not expected, since no change in the interaction strength was observed when probing a single surface spot in numerous experiments.

All initial adhesion experiments were performed in the *constant force mode*, where a temporally constant load was applied to the cell during cell-substrate contact. However, for cell-substrate contact times of more than 160 seconds an adjustment of the cantilever position to maintain the load constant was a real challenge for the feedback system. From cell spreading studies it is known that at this timescale cells are actively exploring the substrate by forming and retracting microspikes (see section 6.1). This leads to many cell-induced force impulses which the feedback system was not capable to balance. If such effects occurred, the force measurements were continued in the *constant height mode*, where the piezo extension was held constant. The experiments showed, that the impact of the AFM mode on the cell detachment forces is small for long cell-substrate contact times.

In order to receive information on the strength of cell adhesion, the total detachment forces from at least five cell detachment curves per substrate type and cell-substrate contact time, $t_{contact}$, were evaluated. For small cell-substrate contact times, no damage of the cell due to the applied load could be expected, thus for $t_{contact} \leq 40$ sec the adhesion of

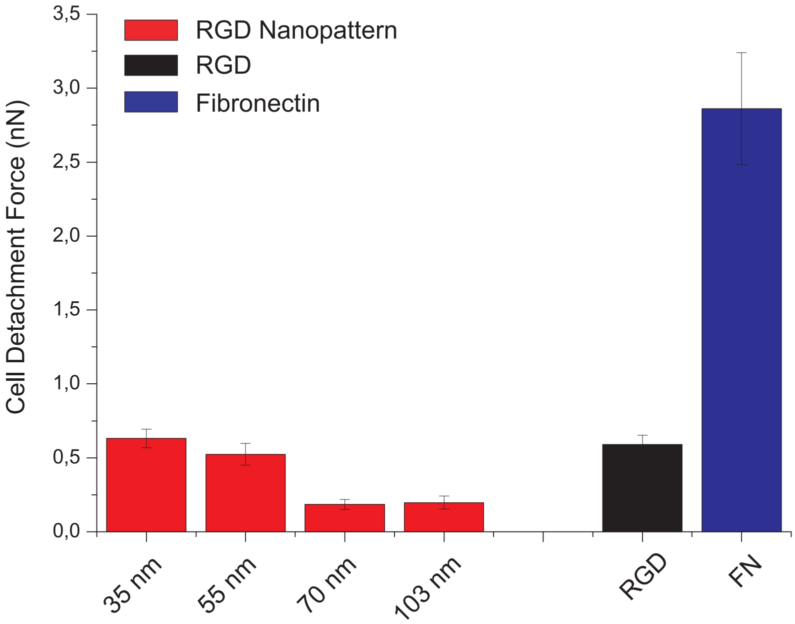

Figure 7.13: Total cell detachment forces on RGD nanopatterns compared to homogeneously coated RGD and fibronectin surfaces for $t_{contact}$=10 sec. Errors in the forces refer to standard errors in the mean. For the variations in integrin binding site spacing the standard deviations are given.

a single cell was frequently probed and the mean detachment forces were calculated from more than 20 cell detachment events.

Figure 7.13 shows total cell detachment forces measured on RGD nanopatterns and on homogeneously coated RGD and fibronectin substrates for a cell-substrate contact time $t_{contact}$ = 10 sec. A homogeneous surface coating with fibronectin leads to almost tenfold higher cell detachment forces than RGD nanopatterns and homogeneous RGD surfaces. This is suggested to be caused by a large number of integrin binding sites offered on fibronectin surfaces and additionally by an enhanced affinity of cells for binding to the natural ECM protein fibronectin, which is supported by the finding that cell spreading proceeds faster on fibronectin surfaces than on RGD nanopatterns (see section 6.2).

Interestingly, detachment forces on RGD nanopatterns with d=35 nm and d=55 nm are almost identical to the forces measured on homogeneous RGD substrates, although one might expect much higher values for the homogeneous RGD substrates because they are expected to carry a higher RGD density. Our results indicate that there is either a minimum spacing of integrins in the cell membrane, which prevents enhanced adhesion on homogeneous RGD substrates, or that the orientational disorder of RGD molecules on the homogeneously coated substrates leads to a restricted accessibility of RGD molecules for integrin binding.

In addition, figure 7.13 allows two regimes of adhesion strength on RGD nanopatterns to be identified, which are separated by the decrease in cell detachment forces between 55 and 70 nm integrin binding site spacing. The existence of the two regimes is more pronounced in figure 7.14. On nanopatterned substrates with d=35 and 55 nm, the detachment forces increase strongly with cell-substrate contact time before they reach a rather high plateau value of more than 1 nN. The forces measured on nanopatterns with d=70 and 103 nm stay constantly below 0.5 nN and are almost independent of the cell-substrate contact time. This also applies for the PEG reference. The observed behaviour is in total agreement with the data obtained with magnetic tweezers, but provides evidence for the influence of integrin binding site spacings on initial cell adhesion in a much larger regime of binding site spacings and cell-substrate contact times (see figure 7.11).

A striking feature of the evolution of the detachment forces shown in figure 7.14 is that the plateau value in our experiment is reached for a time-scale, where cells normally are expected to strongly increase their spreading area and are far away from reaching a stable adhesion state. However, cells are known to react significantly on the 3D structure of their surrounding environment (Beningo et al., 2004). Thus, the simple presence of a second surface might let the cell polarise towards the cantilever and restrict its attachment to the nanopattern, although no biological signalling events are expected to be induced by the concanavalin A coated cantilever, neither do the cells spread onto it. The impact of this second surface might also explain why even for extended cell-substrate contact times of more than ten minutes never an enlarged cell-substrate spreading area could be observed.

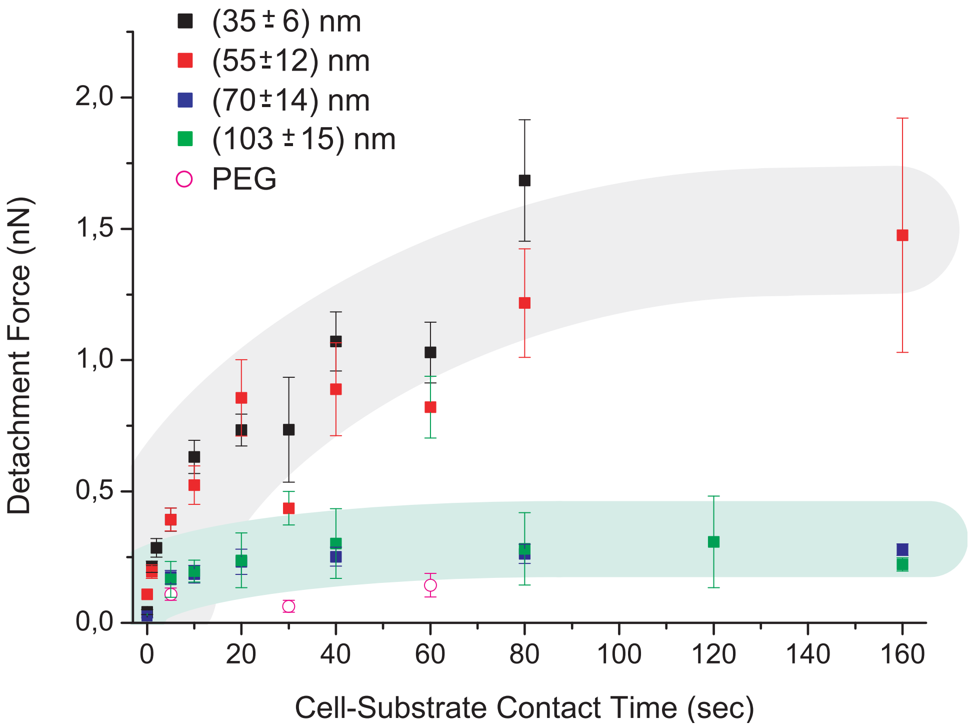

Figure 7.14: Development of cell detachment forces with cell-substrate contact time for different RGD nanopatterns. To simplify a distinction between the two nanopattern regimes, they are shaded green and grey, respectively. Error bars refer to the standard error in the mean.

Figure 7.15 shows the same data in a different representation, where cell detachment forces are plotted as a function of integrin binding site density and spacing, respectively. Cell-substrate contact times were varied from 5 seconds to 310 seconds. For contact times of a few seconds, adhesion forces were dominated by single molecule events, whereas a vast number of successive rupture events lead to an almost continuous detachment process

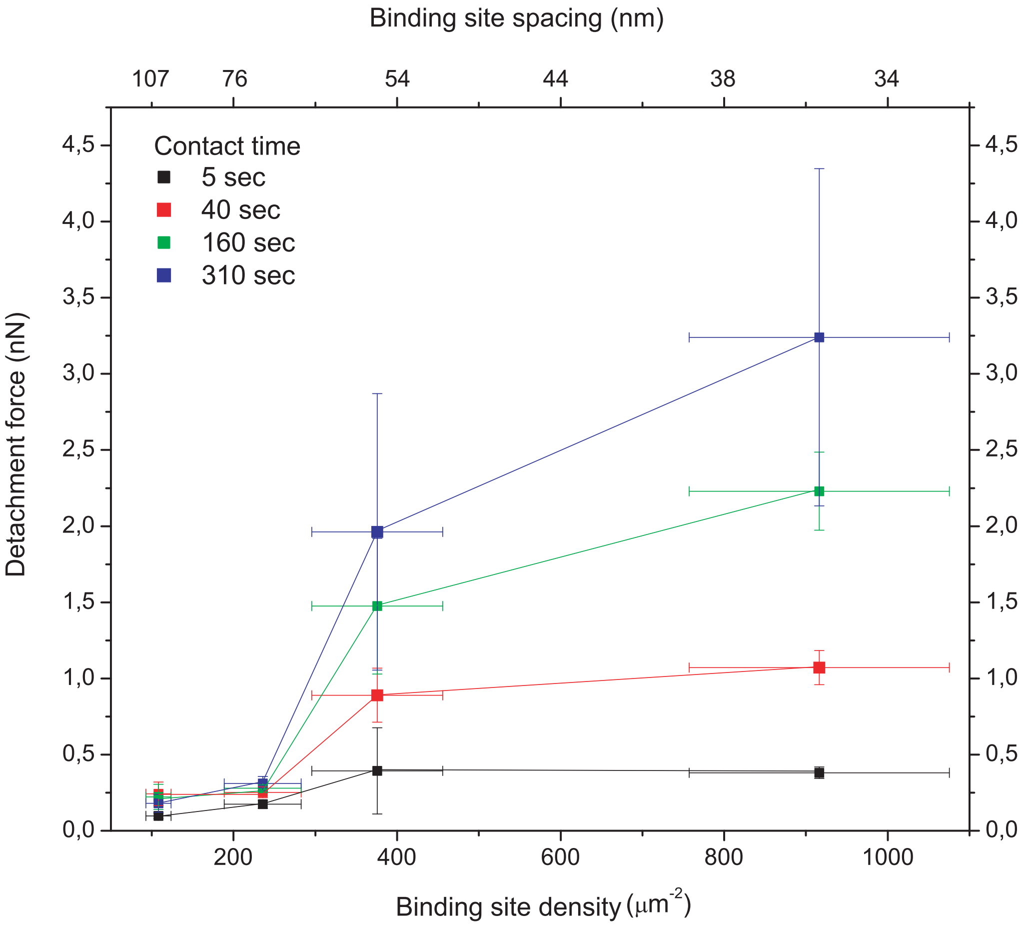

Figure 7.15: Mean cell detachment forces of initial adhesion experiments for different densities (bottom scale) and distances (top scale) of integrin binding sites. The lines serve as a guide to the eye. The error bars in the density of integrin binding sites denote standard deviations. Error bars in detachment force refer to standard errors in the mean.

for $t_{contact} \geq 1$ minute. A distinct transition in detachment forces is observed when the integrin binding site spacing d is decreased from 70 nm to 51 nm. This step is not very pronounced for short cell-substrate contact times ($t_{contact} = 5$ sec), but the longer the cell-substrate contact time, the stronger becomes the discontinuity in the detachment forces. This discontinuity enlarges because the detachment forces stay almost constant for $d \geq 70$ nm whereas they significantly increase for $d=$ 35 and 55 nm. It is important to note that detachment forces for $d=$ 35 and 55 nm are approximately equal for $t_{contact} = 5$ sec but rise differently with contact time and the force increase is larger for higher binding site densities.

The intriguing feature of cell adhesion strength as a function of integrin binding site spacing and cell-substrate contact time can be interpreted within the framework of cooperative integrin interactions and the formation of small integrin clusters, which are expected to be precursors of focal contacts. The formation of such clusters requires an aggregation of integrins either in the form of a direct integrin-integrin or integrin-linker-integrin interaction (Li et al., 2003b; Cluzel et al., 2005). As discussed in chapter 2, clusters strongly stabilise biological adhesion. With nanopatterned substrates, integrins can be held at defined spacings and above a critical value the integrin interactions and consequently also cluster formation could fail. Then the relatively weak RGD-integrin bonds are not stabilised, bond rupture is favoured and no stable adhesion can be established. On the contrary, cluster formation can support integrin binding if the distance of integrins is smaller than the critical value. Then adhesion is stabilised and can be extended. Accordingly, we attribute the obtained discontinuity in cell detachment forces and their time evolution to a failure of cooperative integrin interactions above a critical integrin spacing. The transition between cluster-supported and non-supported adhesion was found to lie between 55 and 70 nm of integrin binding site spacing, in agreement with previous studies (Arnold et al., 2004; Cavalcanti-Adam et al., 2006). A function which quantitatively summarises these ideas is derived in the next section and compared to the experimental data.

So far, all presented data resulted from experiments where the cantilever was retracted with a speed of 5 µm/sec. Additionally, experiments with different cantilever retraction speeds were performed. Figure 7.16 a shows detachment forces of a cell which was in contact with a 55 nm RGD nanopattern for 5 seconds before it was retracted with a velocity between 0.3 and 30 µm/sec. The plot indicates a dependence of the detachment forces on the logarithm of the cantilever retraction speed. We suggest that this cantilever retraction speed v is in direct proportion to the loading rate r, which is applied to the bonds in the cell-substrate contact zone. In figure 7.16 b, similar data for the interaction of a cell with a 35 nm RGD nanopattern are plotted, with the difference, that this experiment was performed for several cell-substrate contact times. Although the data cover less than one decade of cantilever retraction speeds, they show that with increasing cell-substrate contact time not only the absolute values of detachment forces increase, but also the force per retraction speed, dF/dv, and consequently dF/dr.

These results can be understood in the framework of a theory, which describes the rupture force of adhesion clusters as a function of loading rate (Erdmann and Schwarz, 2004a). For the situation in the experiments shown in figure 7.16, we propose that the total loading is shared equally among the cell-substrate bonds (see section 2.3). For such an arrangement of bonds, the analysis by Erdmann and Schwarz (2004a) revealed two distinct scaling regimes for the dependence of rupture force on loading rate, namely slow and fast loading. In the regime of slow loading, the rupture force is independent of loading rate and thus cannot describe our experimental results. Instead, for fast loading the rupture force is given by

$$F = N_{eq} F_0 \ln(r/(N_{eq} k_0 F_0)) \tag{7.3}$$

and depends strongly on the loading rate r and the stationary number of bonds at zero force, N_{eq}. $F_0 = k_B T/x_B$ is the internal force scale of the molecular bonds and k_0 is the unbinding rate at zero force. Equation 7.3 predicts the linear relation between rupture forces and the logarithm of loading rate, as it is observed for the data shown in figure 7.16 a. An increase in the total detachment forces with time, as shown in figure 7.16 b, is equivalent to an increase in the number of cell-substrate bonds, N_{eq}. From equation 7.3 it follows that dF/dr increases with increasing N_{eq}, in agreement with our experimental data (figure 7.16 b).

However, so far it is neither clear how the loading rates are distributed among the bonds in the cell-substrate contact zone nor to what extent viscous effects, for example the formation of tethers, influence the experimental data and particularly the loading rates. Future experiments using total internal reflection fluorescence microscopy for the detection of substrate-close protein and membrane areas have the potential to answer these questions.

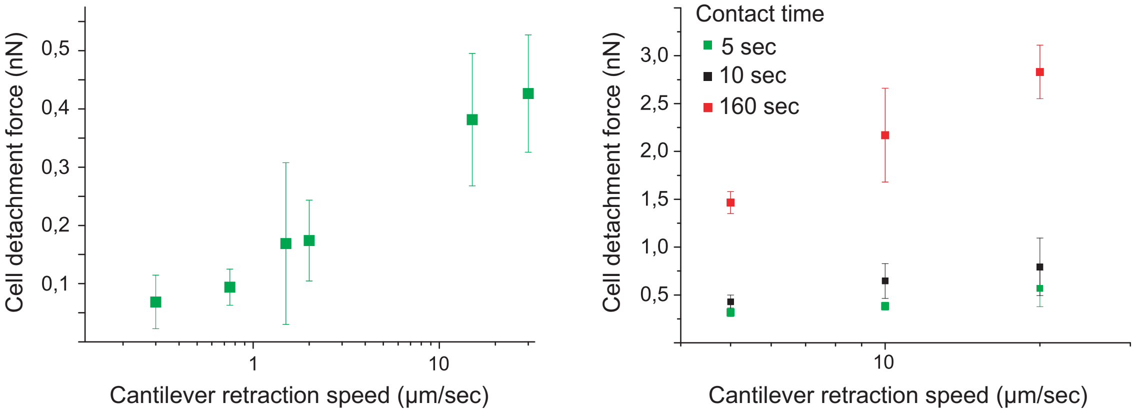

(a) (b)

Figure 7.16: (a) Detachment forces of (a) a cell brought into contact with a (55±12) nm RGD nanopattern for 5 seconds and (b) for different cell-substrate contact times on a (35±6) nm RGD nanopattern as a function of retraction speed. Error bars refer to the standard error in the mean.

7.4.3 Modelling Adhesion Cluster Formation

Integrins are known to cluster in focal contacts, where they induce the hierarchical assembly of a huge number of proteins, which interconnect them with each other and with the cytoskeleton (Zamir and Geiger, 2001a). When integrins are positioned far apart, for example with nanopatterns, such a linkage might fail due to spatial restrictions. The basic idea of the derived model is that a cross-linker protein interconnects integrins and thus stabilises their binding and promotes adhesion cluster formation. A bona fidae candidate for integrin cross-linking is talin, an approximately 60 nm long focal adhesion protein which provides three binding sites for integrin in its antiparallel, homodimeric configuration (figure 7.17) (Xing et al., 2001; Critchley, 2000; Critchley, 2004; Calderwood, 2004). Furthermore, talin has proven to be involved in early adhesion events (Jiang et al., 2003).

Firstly, the kinetics of the cell-substrate contact formation is examined. Benoit (2000) presented a simple approach which assumes that the number of formed bonds per time, $dN_b(t)/dt$, is proportional to the number of unoccupied binding sites, $N_l(t)$, on the substrate. Since the number of newly formed cell-substrate bonds per time $dN_b(t)/dt$ is equal to the loss of unoccupied binding sites $dN_l(t)/dt$ it follows

$$\begin{aligned}\frac{dN_b(t)}{dt} = -\frac{dN_l(t)}{dt} &\propto N_l(t)\,\text{, and thus}\\ N_l(t) &= N_{max}\,e^{-\lambda t},\ \lambda \geq 0.\end{aligned}$$

N_{max} is the totally available number of binding sites in the cell-substrate contact zone and proportional to the binding site density, $\rho = 2/(\sqrt{3}d^2)$, offered by the quasi-hexagonal

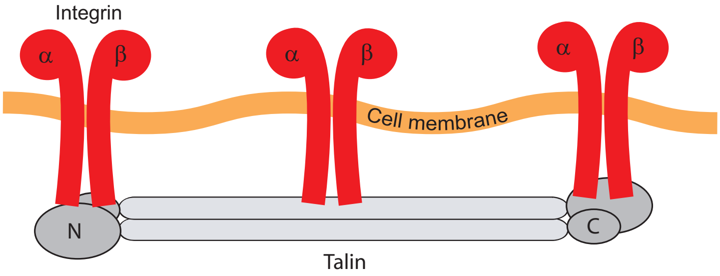

Figure 7.17: Sketch showing the integrin binding sites at the antiparallel talin homodimer (from Critchley (2000)). The high-affinity integrin binding site is located at the N-terminal talin head groups.

nanopattern. λ is a decay parameter and related to the binding probability. With $N_l(t) + N_b(t) = N_{max}$ the number of closed cell-substrate bonds as a function of time becomes

$$N_b(t) \quad = \quad N_{max}(1 - \exp(-\lambda t)). \tag{7.4}$$

A prerequisite of this description is that the number of integrins is unlimited. This should be fulfilled, since receptor densities in the cell membrane of up to 1000/µm^2 are reported (Akiyama and Yamada, 1985) and diffusion processes in the membrane lead to a continuous integrin transport into the contact zone.

We account for integrin cross-linking by introducing a binding stabilisation probability A_1. This probability describes the stabilisation of binding for binding site spacings which fit the integrin cross-linker length. As a quantitative example, we propose the above mentioned talin dimer to be the relevant integrin cross-linker. In talin, the high-affinity binding sites for the integrin are located at the two ends of the approximately 60 nm long dimer, an additional low affinity binding region has been found in the talin rod (Calderwood, 2004). Taking only into account the high-affinity binding sites, then integrin binding can be stabilised on all nanopatterns with a neighbour-to-neighbour distance of 60 nm. As a result of the hexagonal arrangement of binding sites on the nanopatterns, nanopatterns with a binding site spacing of $d_{stable} = 60, 34, 30, 17...$ nm are supposed to support adhesion.

The RGD peptides are bound to the gold dots via a polymer linker of 2 nm length, which allows their lateral position to fluctuate around its mean. This is introduced into A_1 by normally distributed stabilisation probabilities around the d_{stable}. Additionally, the surface available for cell attachment on a functionalised gold dot is expected to have a radius of about 2 nm. Consequently, the stabilisation of binding as a function of integrin binding site spacing d is modelled with normal distributions around d_{stable}, each with a standard deviation of ± 4 nm. Taking together all binding site spacings which facilitate adhesion, then, according to this model, the stabilisation probability $A_1(d)$ varies even below d=60 nm, as shown in figure 7.18. This variation would be caused by a failure of integrin cross-linking due to an inappropriate distance of integrin binding sites. So far it was not possible to investigate this hypothesis experimentally, so we set this issue aside for the present study and instead take the bond stabilisation probability to be constant for $d \leq d_0 = 60$ nm (dashed curve in figure 7.18):

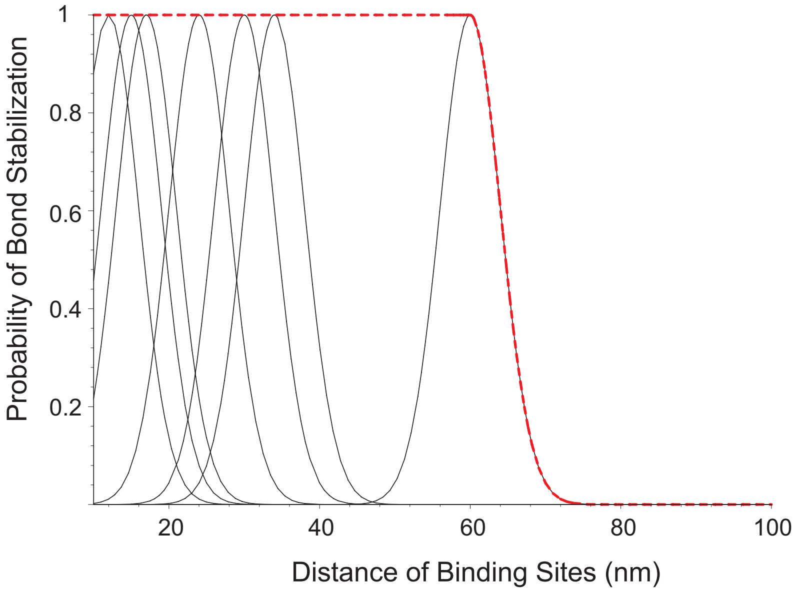

Figure 7.18: Bond stabilisation by talin through integrin cross-linking at appropriate distances of integrin binding sites. The black lines correspond to stabilisation through the integrin binding sites at both ends of the talin dimer. The dashed, red curve gives the bond stabilisation probability used for fitting the experimental data.

$$A_1(d_{site}) = \begin{cases} 1 & : \quad d \leq d_0 \\ e^{-\frac{(d-d_0)^2}{2\sigma^2}} & : \quad d > d_0 \end{cases} \tag{7.5}$$

In contrast to the situation for $d \leq d_0$, the probability for a survival of non-cross-linked bonds at $d > d_0$ is much smaller. This is accounted for by the parameter $A_2 < 1$.

Even for $d \leq d_0$ only integrins with a distance of d_0 can be cross-linked, thus the effectively cross-linked density of integrins cannot exceed the one defined by d_0, corresponding to a maximum cross-linked density of $\rho_0 = \rho(d_0)$. Accordingly, the residual bonds on substrates with $d \leq d_0$ cannot be cross-linked and have a much higher unbinding probability than the cross-linked ones. Since the clusters formed for $d \leq d_0$ both decrease membrane fluctuations and the diffusion coefficient for protein traffic inside the contact zone, the rebinding rate for non-cross-linked proteins inside a cluster is suggested to be higher than for free-standing proteins. Therefore, the survival probability of such non-cross-linked integrin bonds is accounted for by introducing the parameter A_3 with $1 > A_3 > A_2$. The density of non-cross-linked integrins is $\rho_{eff} = \rho(d < d_0) - \rho_0$. The binding of these non-cross-linked integrins results in differences of the detachment forces for integrin binding site spacings at $d \leq d_0$. In consequence, the detachment forces are for $d \leq d_0$ not expected to scale directly proportional to $\rho(d)$, but to ρ_{eff}. The experiments for detachment forces at $t_{contact}$= 310 sec support this picture, as there the detachment forces are indeed not in direct proportion to $\rho(d)$.

The stabilisation probability through integrin cross-linking, A_1, and the bond survival probabilities A_2 and A_3 can be used to calculate the maximum number of bonds which can stably form as a function of integrin binding site spacing d:

$$N_{max}(d) \propto \begin{cases} 1 \cdot \rho_0 + A_3(\rho(d) - \rho_0) & : \quad d \leq d_0 \\ e^{-\frac{(d-d_0)^2}{2\sigma^2}}(1 - A_2)\rho(d) + \rho(d)A_2 & : \quad d > d_0 \end{cases} \tag{7.6}$$

For a final fit of this model to the experimental data, a time dependent hindrance of receptor diffusion was included. Such subdiffusive effects are expected to be induced by the increasing density of obstacles in the form of clusters for $d \leq d_0$. The time t in (7.4) is commonly related to the area a receptor can explore by diffusive motion. When subdiffusive motion occurs, this area is reduced and then proportional to an effective time $t_{eff} = t^\alpha$ with $\alpha \leq 1$. The existence of such subdiffusive effects in the context of molecular crowding has been shown recently (Weiss et al., 2004; Tolic-Nørrelykke et al., 2004) and is theoretically well-described (Höfling et al., 2006). The final relation for the number of stably formed cell-substrate bonds as a function of time and binding site spacing is then

$$N_b(t, \alpha) = N_{max}(d)(1 - \exp(-\lambda t^\alpha)) \tag{7.7}$$

with $\alpha < 1$ for $d \leq d_0$ and $\alpha = 1$ for $d > d_0$.

The number of stably formed bonds per area was related to a force by multiplication with the rupture force of a single bond, F_{sm}, and the area of the cell-substrate contact zone, $\mathcal{A}$. For simplicity, corrections according to equation 7.3 are assumed to play a minor role for the situation discussed here. The final fit function for the cell detachment forces explicitly reads:

$$F(t, d, \alpha) = \begin{cases} F_{sm}\mathcal{A}(1 - \exp(-\lambda t^\alpha))(\rho_0 + A_3(\rho(d) - \rho_0)) + F_0 & : \quad d \leq d_0 \\ F_{sm}\mathcal{A}(1 - \exp(-\lambda t))\, \rho(d) \left(e^{-\frac{(d-d_0)^2}{2\sigma^2}} B + A_2 \right) + F_0 & : \quad d > d_0 \end{cases} \tag{7.8}$$

In order to remove the discontinuity of the piecewise defined function, the two parts were adapted by introducing the factor B, which accounts for the relative difference of the values at $d = d_0$. F_0 describes nonspecific cell-substrate interactions. The experimental data can be fitted with (7.8), as shown in figure 7.19. The parameters of the data approximation are $F_{sm} = 0.032$ nN, $\mathcal{A} = 2$ µm^2, $A_2 = 0.02$, $A_3 = 0.1$, $\lambda = 0.01147$ 1/sec and $F_0 = 0.09$ nN. The values received for α are shown in table 7.2 for different cell-substrate contact times. As expected, α decreases with increasing contact time, since the number of obstacles in the contact zone grows with time. The effect caused by subdiffusion could in principle also be modelled by a change in the binding probability λ. We have decided to explain our data in terms of subdiffusion, since it provides a clearly defined physical model for the diffusive processes in the cell-substrate contact zone. A short calculation shows the relevance of subdiffusion processes in our experiments: if a cell-substrate contact zone of 2 µm^2 is assumed on a 55 nm nanopattern, then $N_{max} \approx 750$ and the measured force for $t_{contact} = 310$ sec corresponds to $N_b \approx 60$ and thus to an obstacle density of approximately 8 %. For such obstacle densities a decrease of the diffusion coefficient is indeed predicted by theory (Höfling et al., 2006).

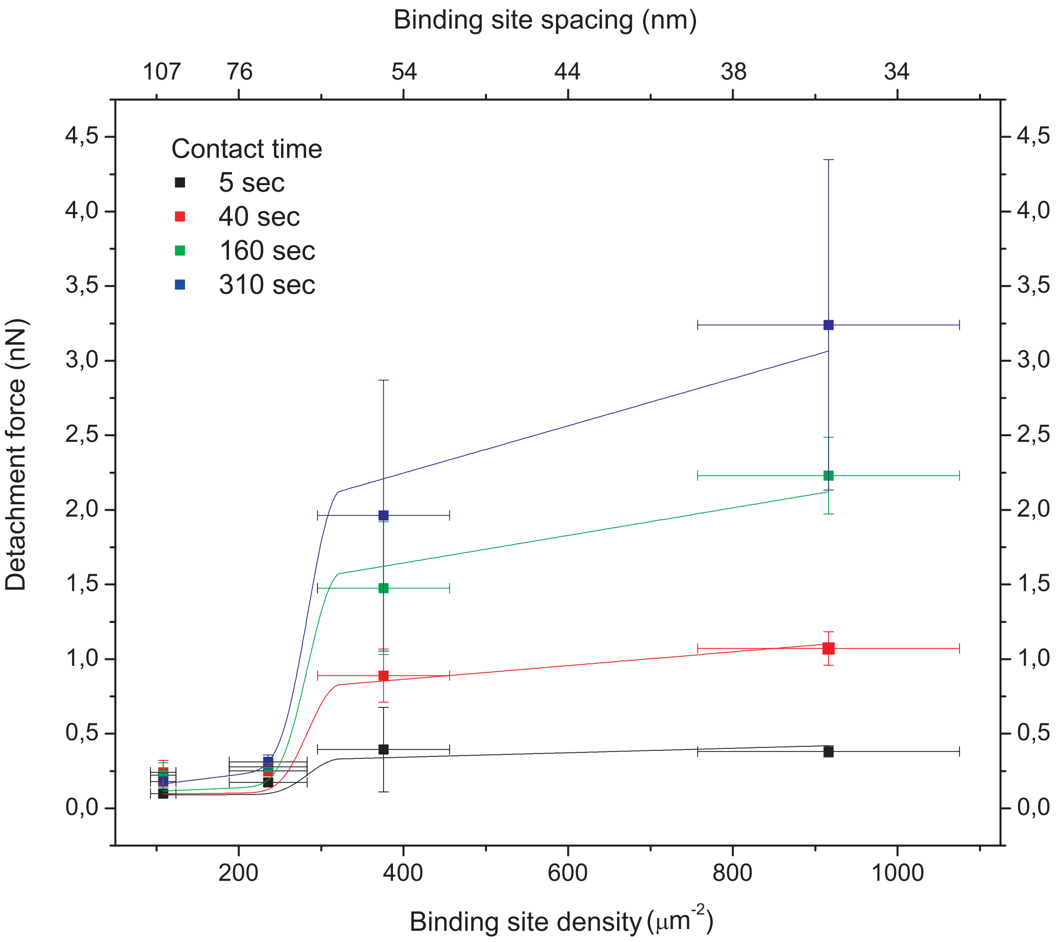

Figure 7.19: Mean cell detachment forces measured in initial adhesion experiments for different densities (bottom scale) and distances (top scale) of integrin binding sites. The data were fitted with $F(t, d, \alpha)$. The error bars in the density of integrin binding sites denote standard deviations. Error bars in detachment force refer to standard errors in the mean.

t_{cont} (sec)	α
5	1 ± 0.09
40	0.74 ± 0.02
160	0.68 ± 0.01
310	0.65 ± 0.01

Table 7.2: The fit of our experimental data shows a decrease of α with $t_{contact}$ as a consequence of subdiffusive processes in the cell-surface contact zone.

7.5 Discussion

The results presented in this chapter show that substantial information on cell properties can be received by addressing questions on viscoelasticity and cell adhesion with force spectroscopy. An additional tool are nanopatterned substrates. Such substrates offer the possibility to restrict or support integrin cluster formation by variations in the distance of single integrin binding sites. This was demonstrated by measuring the temporal development of cell detachment forces as a function of integrin binding site spacing and the results show that cooperative integrin interactions are relevant even for short adhesion timescales of a few tens of seconds. This reflects the amazingly fast nature of adhesion processes and adhesion cluster formation, as it was indicated by a recent study, where the reinforcement of adhesion by externally applied forces was measured (Choquet et al., 1997).

Fibroblast interactions with homogeneous fibronectin substrates have been studied by Garcia and Boettiger (1999) for the first 15 minutes of adhesion. In contrast to our results, they report the absence of cooperative effects during early integrin binding. Instead, a linear increase of bound integrins with fibronectin density was observed. This is no surprise, because in contrast to our measurements on nanopatterns, the usage of homogeneously coated fibronectin surfaces only allows a definition of the global integrin binding site density, but the distance of single integrin binding sites cannot be tuned. For studying integrin clustering, nanopatterns are a great tool, since they allow local binding site densities and spacings to be precisely imprinted onto the surface. This is essential, since integrin clustering is assumed to be switched on and off by integrin binding site spacing, and not necessarily by the global integrin binding site density (Arnold et al., 2004). Our experimental setup makes it for the first time possible to quantify the cooperative strengthening of adhesion from the non-clustered to the clustered integrin configuration during the first five minutes of adhesion. This result is very far-reaching, since no other experiment could study the effect of cooperative integrin clustering in early cell adhesion events so far.

A crucial aspect for the comparison of different works on adhesion is the definition of the term “cooperativity”. In our work, we define the cooperativity of integrins as a direct or linker-mediated integrin interaction. This leads to the formation of stable integrin clusters, and thus preserves adhesion. With this definition, adhesion is strengthened at the global cell level, but it does not necessarily mean that the unbinding force of single bonds is enhanced. Therefore our picture of cooperative binding cannot be directly related to cooperative biochemical systems, such as the well-known example of oxygen binding to hemoglobin.

The picture of a linker-mediated cooperative integrin interaction allowed the experimental data to be explained in terms of a simple model, which includes binding kinetics, subdiffusion and a bond survival probability, which depends on integrin cross-linking. The question, which protein indeed plays the fundamental role for integrin cross-linking and clustering on nanopatterns is the subject of future experiments.

Saturation processes, as observed in the detachment forces for $d \leq d_0$, are not necessarily induced by cross-linkers. Smith and Seifert (2005) have shown that the number of formed bonds in a thermodynamic picture of vesicle adhesion does not scale linearly with ligand density, but instead reaches a saturation level. To some extent a relevance of this view is imaginable, although it cannot explain the force discontinuity observed here.

8 Long-term Adhesion

In contrast to initial cell adhesion, long-term cell adhesion is dominated by the formation of large, micrometre-sized protein clusters, such as focal contacts. A quantitative understanding of the mechanical properties of such adhesion contacts is crucial for unravelling the mechanisms of cell-matrix interaction and their impact on cell adhesion strength.

A very elegant way of studying long-term adhesion contacts is by measuring cell detachment forces with AFM. Within the scope of this thesis a procedure was developed, that permits single cell adhesion strength to be probed at almost any adhesion timescale. In this chapter, our results on experiments probing the long-term cell adhesion strength are presented. The first part covers the methodical aspects of the experiments, in the second and third section the results for the dependence of cell adhesion strength on the distance of integrin binding sites is presented. In the fourth section, we relate our experimental results to a theoretical model, which relates the rupture forces of an adhesion cluster to the applied loading rate. The last section shows results of experiments performed on microstructured substrates.

8.1 Experimental Setup

For the studies presented here, fibroblasts (REF YFP Pax) were allowed to adhere to biofunctionalised substrates under standard cell culture conditions for the desired time period[1]. For a cell detachment experiment, the sample was carefully transferred from the cell incubator into the AFM sample holder, the cell medium was exchanged to CO_2-independent medium (10 % FBS, 2 % L-glutamin, 100 µg/ml penicillin-streptomycin) and the sample temperature adjusted to 36°C. This temperature was chosen to avoid cell damage during heating phases of the sample holder, as then the set temperature could be exceeded by 1-2°C. The FBS concentration was increased to 10% in order to induce a firm cell attachment at the tipless cantilever. For a successful cell detachment, the connection between cell and cantilever must be stronger than that between cell and substrate. Therefore the only way to detach focal contacts from the substrate is to induce adhesion contacts at the cell-cantilever interface of at least an equivalent strength. These contacts must be connected to the cytoskeleton and the cytoskeletal fibres to transmit the forces from the cantilever to the cell-substrate contact zone. A cantilever functionalisation with glutaraldehyde, which has previously been used for cell stretching experiments (Micoulet,

---

[1] Prior to cell plating, the substrates were immersed in sterile PBS. The PBS was exchanged twice before adding the cell medium (DMEM, 2 % FBS, 2 % L-glutamin, 100 µg/ml penicillin-streptomycin) and the cell suspension. For issues concerning the substrate preparation and the cell culture protocols see section 3 and the appendix, respectively. The passivation reagent used for the studies in this chapter was the PLL-g-PEG.

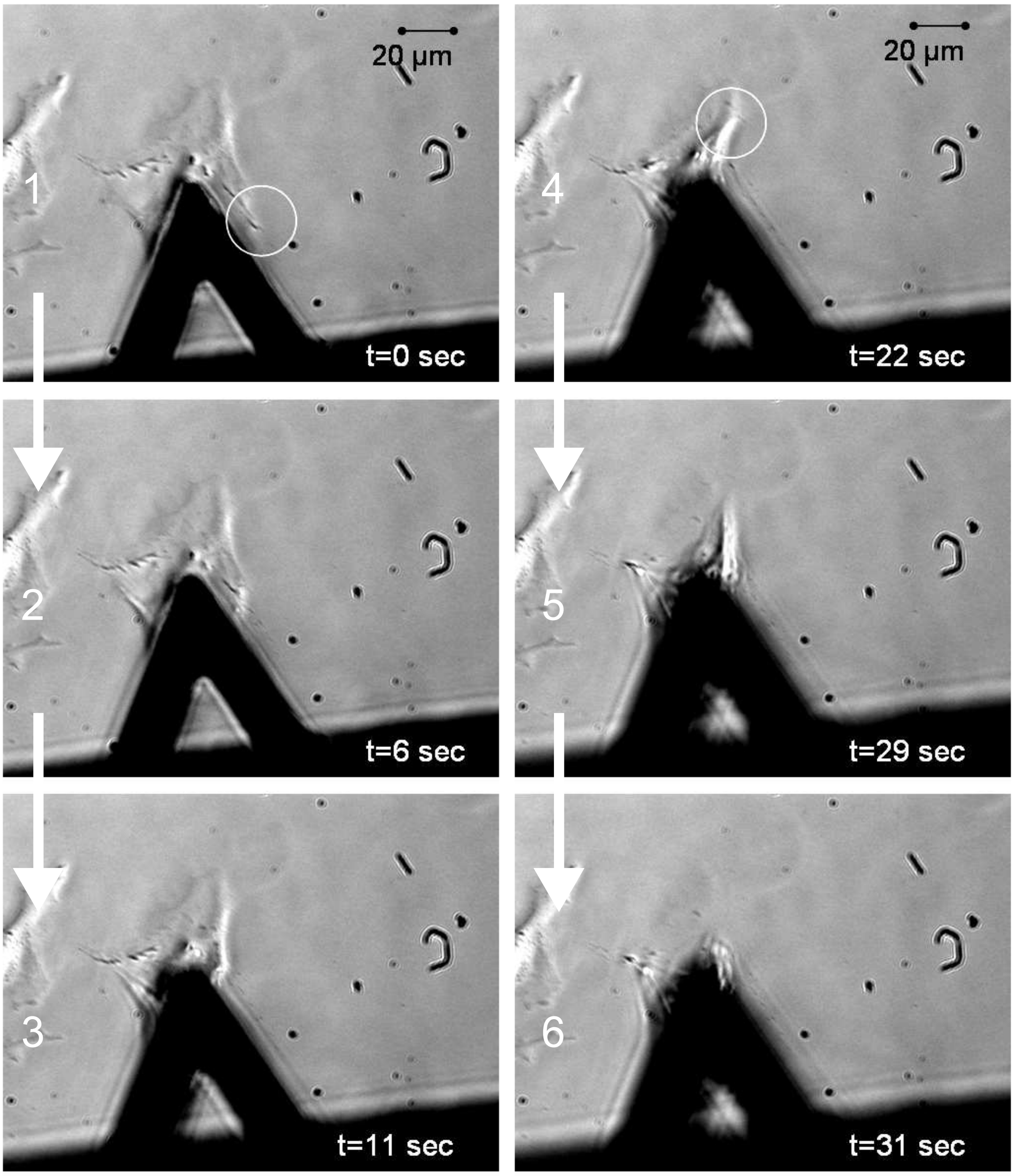

Figure 8.1: Series of bright-field images showing the detachment of a well-spread cell from a glass surface by an AFM cantilever. The cell was allowed to adhere to the surface for 24 hours prior to the experiment. In the images, the detached parts are highlighted with circles, the arrows and the image numbers guide through the time course of detachment.

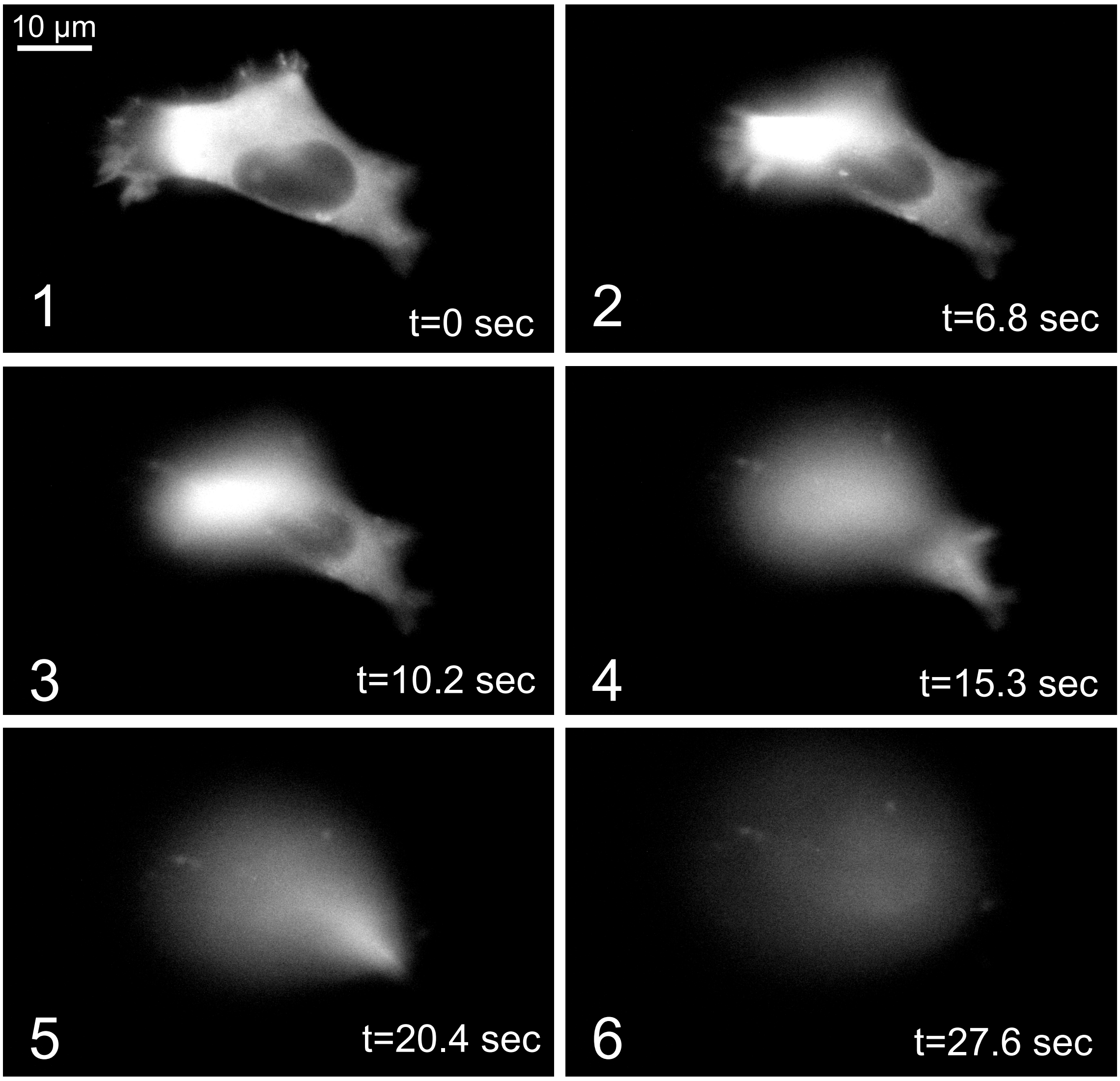

Figure 8.2: Typical example showing the fluorescence of YFP paxillin of a cell while it detaches from an RGD nanopattern with integrin binding site spacing $d = (90 \pm 15)$ nm. The cell was allowed to adhere on the substrate for 3 hours prior to its AFM driven detachment.

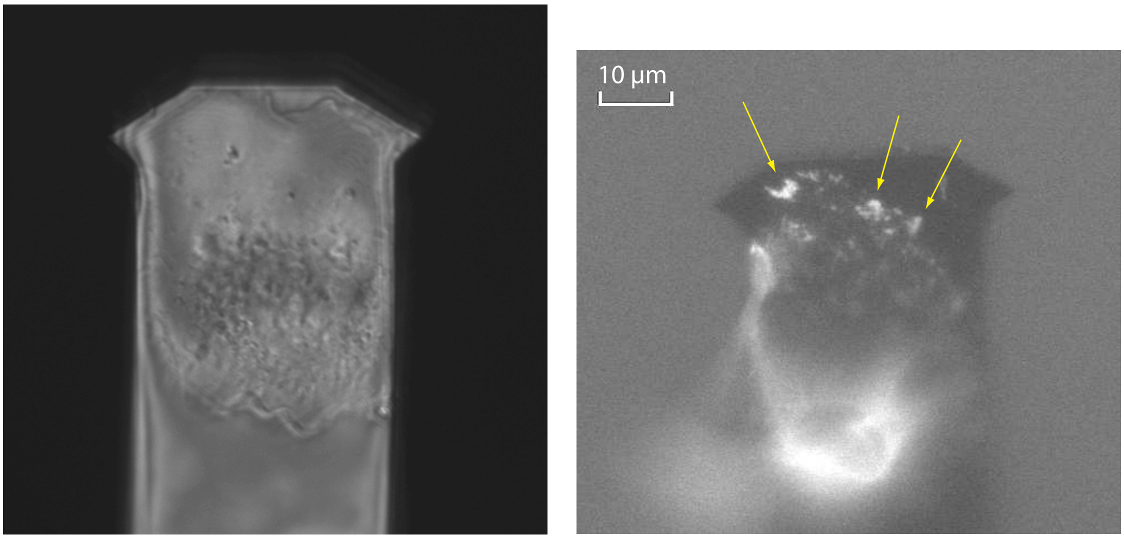

(a) (b)

Figure 8.3: (a) Reflection microscopy image of a cell spreading at the cantilever after being detached from a substrate. (b) Fluorescence image, which shows adhesion clusters at the cantilever (arrows) by the fluorescence of YFP paxillin.

2004), did not lead to a firm cell attachment. Glutaraldehyde covalently binds proteins in the membrane, but does not lead to adhesion cluster formation or a coupling to the cytoskeleton. For our experiments the cantilevers were functionalised with fibronectin, in order to induce focal contact formation at the cell-cantilever interface (see figure 8.3 b). Because fibronectin binds the same class of integrins as the RGD on nanopatterned substrates, the cell-cantilever contact could diminish the cell-substrate binding strength by a depletion of the integrin contacts. In order to limit this effect, the cantilever was touching the dorsal[2] side of the cell for a relatively short time period prior to cell detachment. For nanopatterns offering a distance of integrin binding sites $d < 70$ nm, this time period was not longer than 10 to 15 minutes, for nanopatterns with $d \geq 70$ nm, it was 4 to 6 minutes. The cell is coupled to the cantilever only shortly before the force measurement, thus it is influenced by the cantilever for a comparably short time compared to the timescale it was allowed to adhere at the substrate prior to any external mechanical stimulus (see chapter 4.3.4).

A typical experiment is shown in figure 8.1, where a well-spread cell is detached from a glass slide by retracting the cell-bound cantilever. In contrast to initial adhesion experiments, where cells remain in a spherical shape throughout the experiment, the cell here was spread onto the substrate before the cantilever was attached. The detached parts of the cell are highlighted with circles. This image series shows the main aspect of the cell detachment process: the cell is detached from the substrate step by step, with a tensional stretching of the cell body in between the detachment steps. To avoid cell damage due to excessively quick detachment, slow cantilever retraction velocities of 0.33 to 0.83 µm/sec were used.

Bright-field microscopy does not give precise information on the detached cell area or fo-

---

[2] The dorsal side of a cell is the opposite side to that in contact with the substrate.

cal contacts. Hence, in all experiments the cell detachment was observed with fluorescence microscopy, where the fluorescence of YFP labelled paxillin, a major component of focal contacts, was excited[3] (see figure 8.2). To make sure that only cell-substrate detachment events and not cell-cantilever ruptures are detected in the force curve, the steps in the force curve were identified with rupture events observed in the fluorescence images. Cells normally do not undergo apoptosis after detachment but instead continue spreading onto the cantilever, as shown by a reflection microscopy image in figure 8.3 a.

Long-term experiments are quite time-consuming and complex to realise, so that the data discussed in the following sections show the results of a total of 141 single cell experiments, where in only 56 cases the cell was successfully detached from the substrate. This leads to a final output of about 10 to 15 cells that were probed on each of the four nanopattern types used in our study. In order to avoid systematic errors by accidentally only having probed weakly adhering cells, the mean values of cantilever-cell detachment forces were calculated for those experiments where the cell was released from the cantilever. On average, the means of these values lie below the measured forces of successful cell-substrate detachment. All force values discussed in the following sections were calculated from the cantilever deflections according to the procedures described in chapter 4.3.

8.2 Cell Detachment Forces

There are several approaches to analysing cell detachment forces in order to receive a comparison of adhesion on different substrates. The easiest way to quantify cell detachment is by determining the total cell detachment force, that is the sum of all observed steps in the force curve. An example of a typical force curve is shown in figure 8.4.

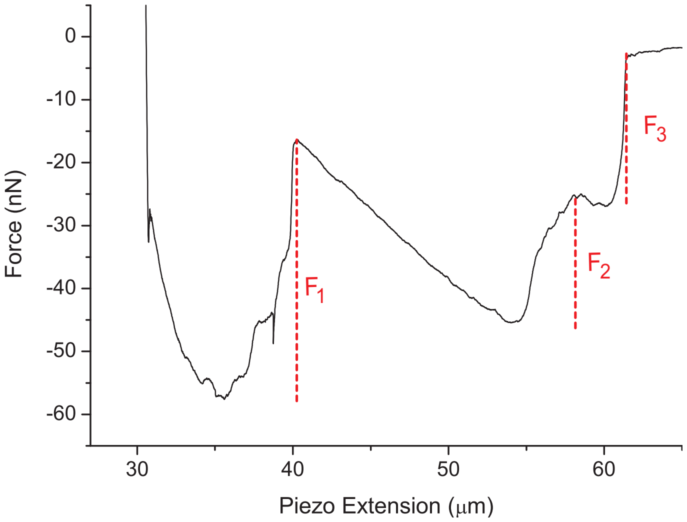

Figure 8.4: Typical force curve for cell detachment. The dashed lines show the distinct rupture events. The total detachment force is $F = F_1 + F_2 + F_3$.

---

[3] All fluorescence images were taken with a 40 x objective (EC Plan-Neofluar, NA=0.75, Zeiss, Germany) and recorded with a high-resolution camera (Digital CCD Camera ORCA-ER, Hamamatsu Photonics, Germany).

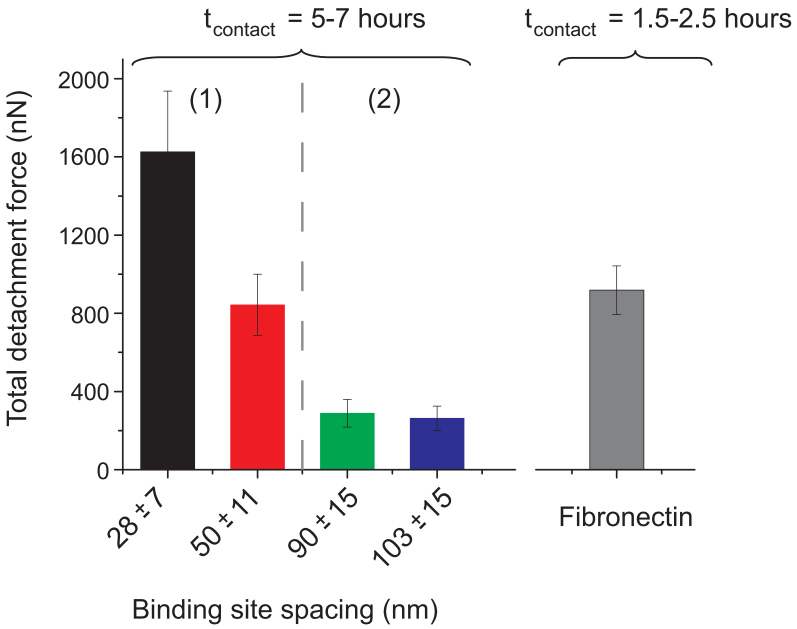

Figure 8.5: Average total detachment forces on nanopatterns after 5-7 hours of cell adhesion compared to detachment forces on fibronectin after 1.5-2.5 hours of adhesion. The dashed line marks the transition between regimes (1) and (2).

Figure 8.5 shows the average total unbinding forces for different nanopatterned substrates measured after 5-7 hours of cell adhesion and compares them to the total unbinding forces on homogeneous fibronectin surfaces after 1.5-2.5 hours of adhesion. Longer adhesion times were also tested for fibronectin substrates, but then no sufficient attachment of the cantilever at the dorsal side of the cell could be achieved. This is presumably a result of a strong cell polarisation towards the substrate, which is induced by the adhesion to fibronectin. The total unbinding forces on these substrates demonstrate three things: Firstly, cell adhesion on fibronectin substrates is much stronger than on nanopatterns, since the detachment force of cells on fibronectin surfaces after 1.5-2.5 hours of adhesion is comparable to that on 50 nm nanopatterns after 5 hours of adhesion. Results from cantilever-cell detachment events suggest a cell-fibronectin interaction force of more than 2 µN after 3-4 hours of adhesion. Secondly, the data indicate the existence of two adhesion regimes on nanopatterns: A regime 1 of high adhesion strength for an integrin binding site spacing of d=28 nm and d=50 nm, and a regime 2 of low adhesion strength for d=90 nm and 103 nm. Thirdly, in regime 1, a difference in adhesion forces between nanopatterns of d=28 nm and d=50 nm is obtained, which is a logical consequence of the larger surface density of integrin binding sites for d=28 nm compared to d=50 nm. However, no cooperative increase in the total cell detachment forces between regimes 1 and 2 is obtained. This was originally expected, because in regime 1 focal contacts can form, in contrast to regime 2 (Arnold et al., 2004). Instead, a comparison of the cell detachment forces obtained for d=50 nm and d=90 nm shows that the increase in total cell detachment forces between regimes 1 and 2 can equally well be explained by the increase in the density of integrin binding sites on the substrate.

For membrane systems, such as giant vesicles, it is known that the edge of the contact

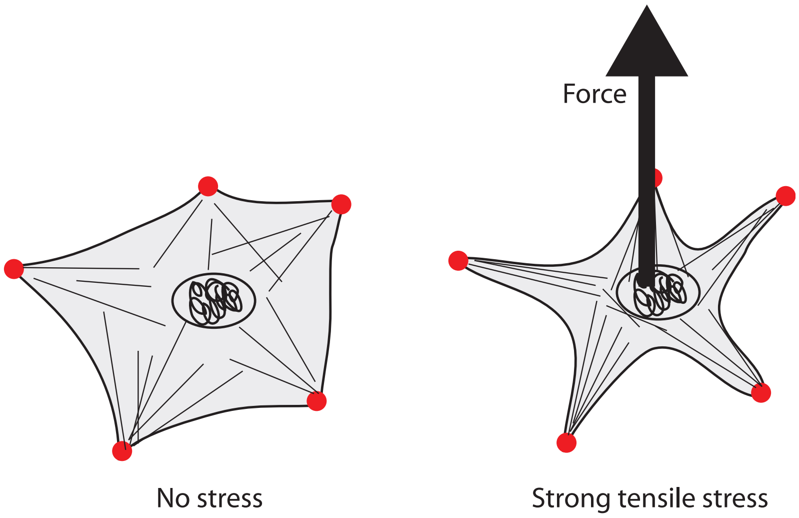

Figure 8.6: Sketch of a well-spread cell when it is loaded with a tensile stress. The adhesion force is then concentrated in the adhesion centres (red circles), which pin the cell to the substrate.

zone has to resist the largest stress. Therefore, at first glance a normalisation of the forces to the cell perimeter seems to be reasonable. This is contradicted by the typical way of cell detachment, where the cell edge slides along or is even detached from the surface without leading to a measurable detachment force signal. This proceeds until the tensile forces are concentrated in the adhesion centres, as is illustrated in figure 8.6 and shown in figure 8.1. For the same reason, a normalisation of the cell detachment forces to the cell spreading area is not reasonable.

In order to determine the locally acting cell detachment force, we normalised the data by taking the detached cell-substrate contact zone as a reference for normalisation. This means that for 28 and 50 nm nanopatterns only the focal contact area is taken as reference, since the focal contacts sustain the major part of the load and the situation shown in figure 8.6 precisely applies. For nanopatterns where no focal contacts are formed, the load-bearing contact zones are extended compared to focal contact areas, as can be observed in figure 8.2 in the beginning of this chapter. In such cases, cells are often very elongated, for example having two extended binding areas, whereas the central cell region in between is only loosely connected to the substrate. With the fluorescence images, also for these cases the area detached in a rupture event could be determined. Figure 8.7 shows the results of the analysis, which clearly proves the local increase of detachment forces per area due to focal contact formation. While the binding site density between d=50 and 90 nm increases by a factor of 3.2, the cell detachment force per area increases by a factor of 14.3. This incidence is assumed to be due to a cooperative enhancement of the local detachment forces as a result of focal contact formation. This means that the cell concentrates the majority of the bonds in the comparably small focal contacts. If no focal contacts can form, the bonds are distributed over the large cell-substrate contact zone. Interestingly, the unbinding forces per detached focal contact area do not increase in direct proportion to the adhesion spot density, which is clear from the forces for $d = 50$ nm and $d = 28$ nm (figure 8.7). The simplest explanation for this observation is the existence of a maximum protein packing density in the adhesion plaque. From a biological point of view

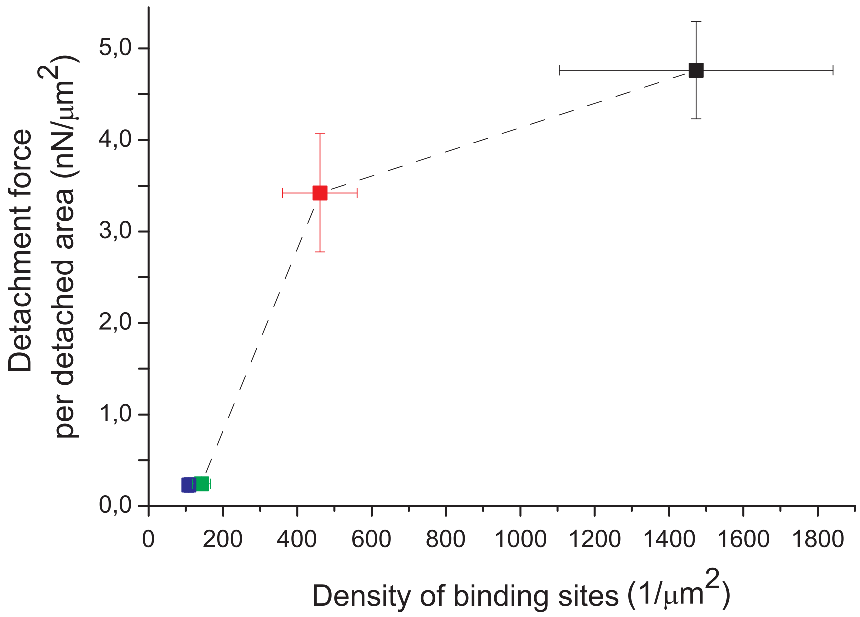

Figure 8.7: Cell detachment force per detached area versus the density of integrin binding sites. The dashed line serves as a guide to the eye. The error bars in the density of integrin binding sites denote standard deviations, error bars in the detachment force refer to standard errors in the mean.

this observation needs further investigation, for example by determining the fluorescence intensity of different focal contact proteins as a function of binding site density.

In single molecule experiments, the detachment forces are often interpreted in terms of binding energy (Li et al., 2003a). In our experiments, a calculation of binding energy would also contain the energy used for elastic and inelastic cell deformations. Thus, the physical meaning of cell binding energy is questionable and a discussion of this aspect is left aside for this study.

Further analyses of the force curves allow conclusions on the cell elasticity to be drawn. This is achieved by determining the force slopes prior to detachment events, as shown in figure 8.8. This example shows that the cellular force constant typically decreases from one detachment event to the next, since less and less cell volume is stretched. Such a situation can be compared with pulling parallel springs over a certain distance. The more springs are stretched, the larger is the force necessary to obtain an extension of the whole system. If fewer springs are pulled, the force needed to stretch the configuration over the same distance is less. The averaged cell force constants on nanopatterns are given in figure 8.9. The elastic resistance of cells on nanopatterns with integrin binding site spacings of 28 and 50 nm is quite high, which is a sign for a well-developed cytoskeleton. The results for a binding site spacing of 90 and 103 nm show the opposite behaviour, there cells can be extended by very small forces. This observation is strongly supported by results from Arnold et al. (2004), where no actin stress fibre formation was observed for ligand distances above 73 nm. In conclusion, the cellular force constants shown in 8.9 represent the dramatic differences in cell elasticity between regimes 1 and 2 of integrin binding site spacing.

The cellular force constants presented here cannot be related to Young's moduli, since

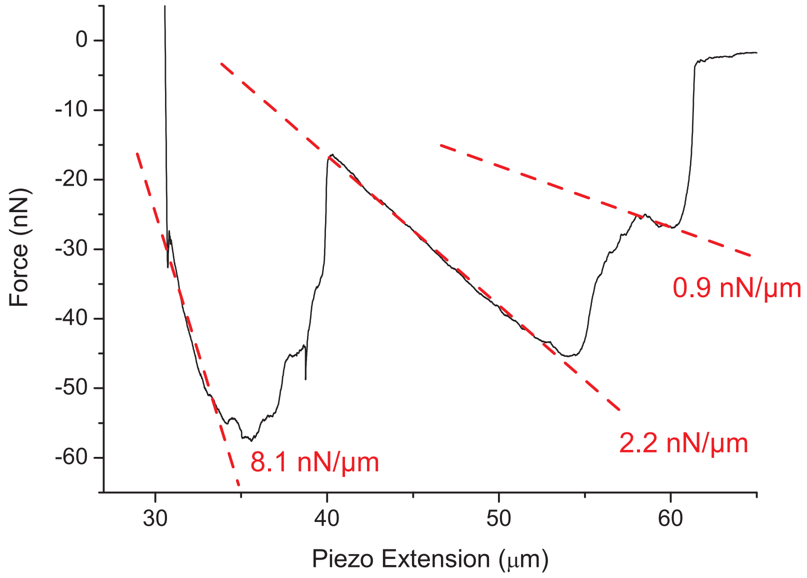

Figure 8.8: Typical force curve showing the regions where the cell is elastically stretched before rupture occurs (dashed lines). The force constant decreases with the number of detachment events.

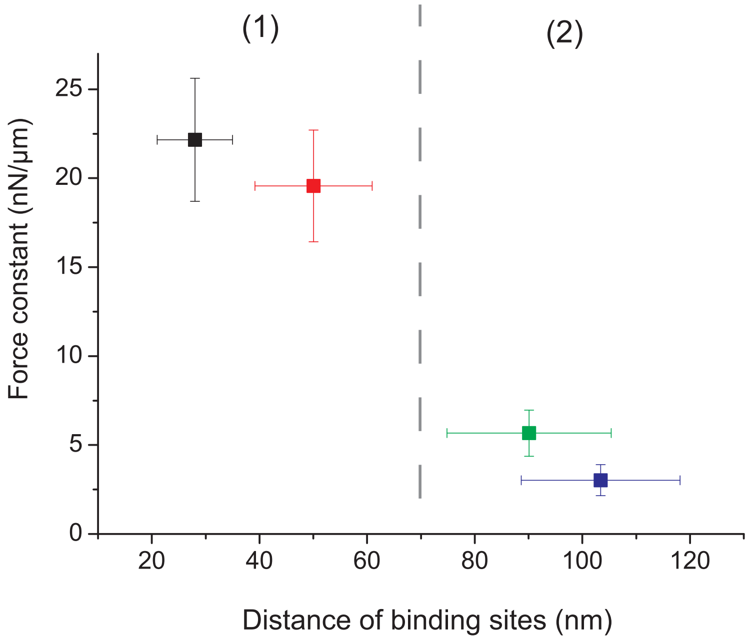

Figure 8.9: The force constant of cells depends on the distance of integrin binding sites. The dashed line marks the transition between regimes (1) and (2). Error bars refer to the standard error in the mean.

our present AFM setup does not provide information on the three-dimensional shape of the cell and the stress distribution. However, the force constants measured with the AFM are of the same order of magnitude as those recently obtained with a micromanipulation device, where an adherent cell was stretched by the separation of two microplates (Micoulet, 2004).

An important further application of detecting force slopes is the calculation of loading rates on single focal contacts, which is one prerequisite for a comparison of experimental data with adhesion cluster theories. This is the subject of section 8.4.

8.3 Focal Contact Detachment

By relating fluorescence images series and force-extension curves, the detachment forces can be studied as a function of detached focal contact area. Figure 8.10 shows a focal contact detachment scenario in such an experiment. The cell is well-spread to the substrate and a cantilever is attached at its dorsal side (figure 8.10 a). When the cell is detached from the surface, the different adhesion sites are torn off one after the other. Following this process with fluorescence microscopy shows that not the bonds between substrate and cell, but the focal contacts themselves are broken. This is displayed comparatively in figures 8.10 b and c where the paxillin fluorescence before and after the cell detachment is shown. The steps in the force curve associated with the detachment are marked in figure 8.10 d. Due to the internal rupture of focal contacts, the measured detachment forces are values characterising the strength of the adhesion plaque rather than the direct cell-substrate interaction.

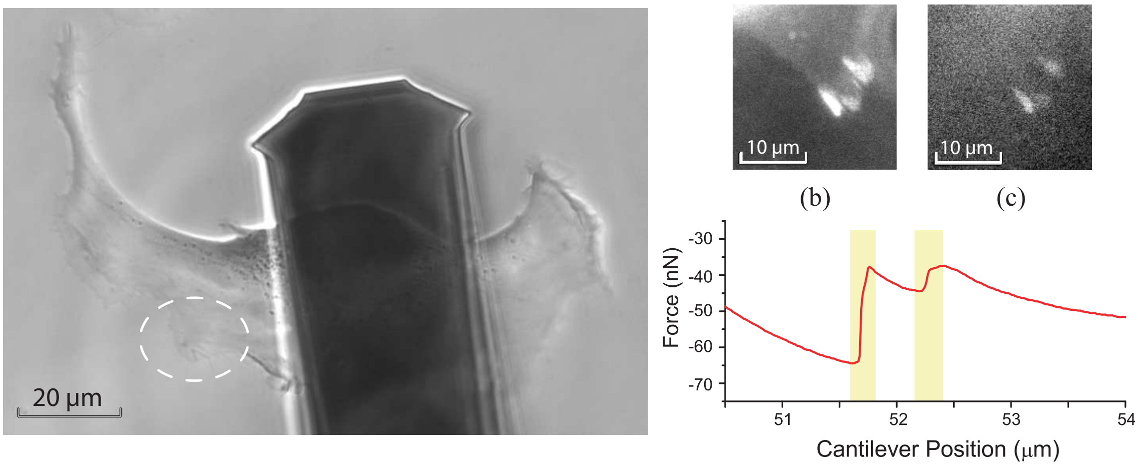

(a) (d)

Figure 8.10: Detachment of an adherent cell from a surface. (a) Bright-field image of a spread cell on a nanopattern with d=(50 ± 11) nm. Fluorescence of the focal contact protein paxillin before (b) and (c) after detachment of the encircled region in (a). A comparison of (b) and (c) shows that the focal contacts remain partly on the substrate although the cell body is detached. (d) Excerpt of a force curve corresponding to the rupture of the focal contacts in (b). The force steps corresponding to the focal contact rupture are marked.

When a cell has several distinct attachment sites, each step in the force curve can be attributed to the rupture of one or several focal contacts, as shown for the force-extension

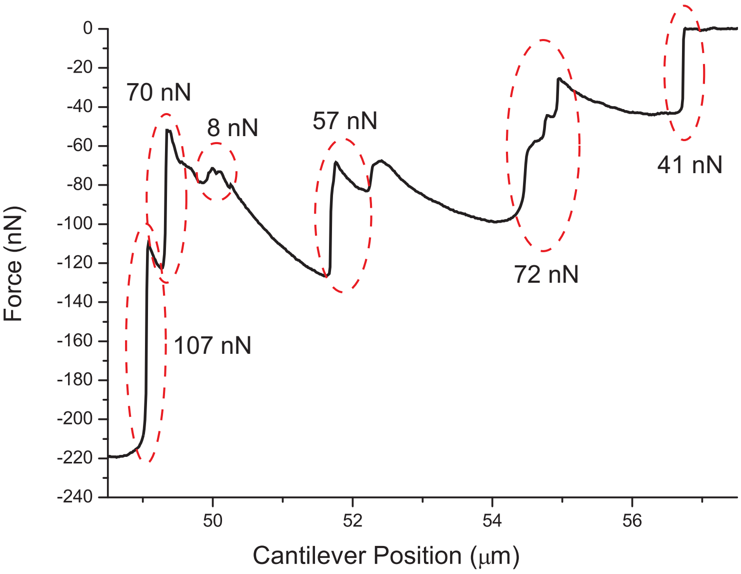

(a)

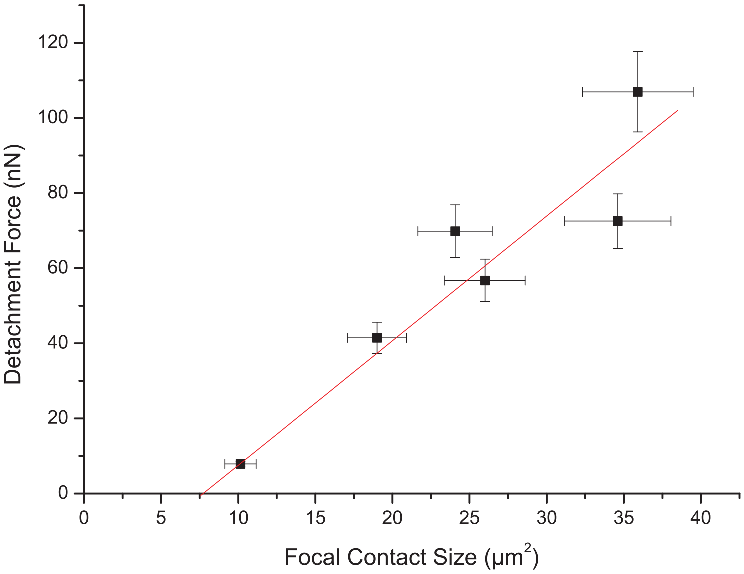

(b)

Figure 8.11: (a) Force-extension curve showing a series of focal contact ruptures for a cell detached from a nanopattern, where the distance of integrin binding sites was (50 ± 11) nm. The forces are plotted as negative values, since the cantilever is bent in the -z direction during retraction. (b) Linear relation between detachment force F and focal contact size A. The data were fitted by the function $F(A) = -25.7\,nN + 3.3\frac{nN}{\mu m^2}A$.

curve in figure 8.11 a. Due to the precise optical information on the size of the detached area, it was possible to relate the measured rupture forces to the size of the detached focal contacts. The result of this analysis is shown in figure 8.11 b. The graph reveals a linear relation between rupture force and focal contact size, for this particular cell with a slope of about 3.3 kPa. This value lies within the stress regime that is reported for cells exerting forces to their surroundings through focal contacts (Balaban et al., 2001; Tan et al., 2003). This was an important finding, since the stress exerted by cells themselves should not exceed the stress necessary for focal contact detachment. Of course, a linear dependence of detachment forces on focal contact area can only be expected if the loading rates applied to the single contacts are approximately equal. The loading rates can roughly be controlled externally by the cantilever speed, but the elastic elements of a cell internally regulate the effective loading rate lasting at a focal contact. A further discussion of how loading rates affect focal contact rupture forces follows in section 8.4.

A second aspect observed in figure 8.11 b is an offset of the linear force relation from the origin. Such a force offset was also observed in a previous study by Balaban et al. (2001) and might result from a critical adhesion cluster size, which is required for the formation of mature focal contacts. Future experiments employing microstructured substrates to restrict the focal contact area could help to further understand this observation.

Riveline et al. (2001) showed that cells increase their focal contact size as a response to shear stress. Theories relating force induced stress distributions to changes in focal contact formation can predict this focal contact growth (Besser and Safran, 2006; Nicolas and Safran, 2004), but do not predict a lateral focal contact growth for forces applied normally to the substrate[4]. In agreement with this prediction, we never observed a focal contact growth while stretching a cell normal to the surface. An internal strengthening of focal contacts as a response to force application cannot be excluded for our experiments. If this should lead to an enormous increase in cell-substrate binding strength which exceeds the cohesion strength of the focal contact plaque, a breakage of the focal contact plaque is a logical consequence. A rupture of the actin stress fibres instead of the focal contact patch is implausible, since parts of the paxillin are removed upon focal contact rupture.

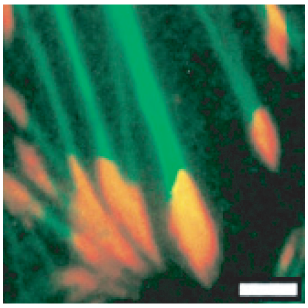

Figure 8.12: Staining image showing that the cytoskeletal actin (green) and the focal contact protein vinculin (red) do not fully coincide (orange). Rather, the actin is restricted to the central area of the focal contact (image taken from Zaidel-Bar et al. (2004)). The scalebar corresponds to 1.7 µm.

The rupture of focal contacts and thus the release of focal contact proteins as a response to force application is a well-known phenomenon in cell biology. For example, migrating

---

[4] Personal information from A. Nicolas, Centre National de la Recherche Scientifique, Nice.

cells leave behind integrins at the side opposite to their migration direction (Palecek et al., 1998). In the cell detachment experiments described in this thesis, the amount of paxillin remaining on the substrate varied a lot from one focal contact to the other, but in the majority of the analysed 23 focal contacts only 30 to 40 % of the fluorescent paxillin was removed. This value is similar to the extent of integrin release reported by Palecek et al. (1998) for migrating cells. As shown by Zaidel-Bar (2004), the binding area of actin filaments does not fully cover the whole focal contact area (see figure 8.12). When the upper part of the focal contact plaque is detached from its base by a force transmitted through actin fibres, it is reasonable that large portions of paxillin remain on the substrate, because the largest amount of stress is only exerted at the central part of the patch.

8.4 Comparison with Theory

In single molecule biophysics, the dependence of binding strength on loading rate r is of substantial interest, because this analysis allows a reconstruction of the potential landscape for the molecular interaction from dynamic force spectroscopy data. For adhesion clusters, such as focal contacts, the situation is much more complicated.

The basic idea of the following analysis was to relate the experimental data on the rupture force of adhesion clusters to a theoretical model that describes the forces needed to break focal contacts as a function of loading rate. The most critical point of the analysis was to find the loading rate applied to focal contacts. By combining the elastic response of a cell prior to distinct rupture steps (in nN/m) with the constant cantilever retraction speed (in µm/sec), the loading rates on single focal contacts could be determined. However, this analysis included some tricky aspects caused by the irregular cell geometry, which leads to an anisotropic force distribution inside cells. Therefore it was first necessary to determine the distribution of the loading rate over the cell-substrate contacts. This was performed by distributing the loading rate over all focal contacts pulled on, assuming that the amount of carried load per single contact is proportional to its size. Second, one has to account for "loose" contacts, which are dangling while other bonds in the cell are already tensed. This can for example happen when due to an anisotropic cell geometry not all contacts are loaded at the same time, but instead one after the other. Normally, the force constant decreases with each detachment step, since less material is strained. If instead an increase of the force constant is measured after a detachment, this indicates that prior to the detachment less material was stretched. The final analysis to obtain the loading rates was performed by comparing the elasticity data with the course of detachment and with fluorescence movies, which in most of the cases also gave hints to optically identify loose contacts. In this way we distributed the applied load over the tensed contacts.

The bonds inside a focal contact are suggested to be arranged in a parallel configuration. For such a situation, the rupture behaviour of the adhesion cluster under linear loading ($F(t) = rt$) is theoretically well-described (Erdmann and Schwarz, 2004a). In this model, the average force needed to break the adhesion cluster is given as a function of three parameters: the maximum number of bonds N_t, the rebinding rate k_{on} (in 1/sec) and the loading rate r (in nN/sec). The model predicts two distinct scaling regimes for the dependence of the rupture force on loading rate, which are distinguished by the magnitude of the loading rate. The expressions for the two scaling regimes are

$$F = \begin{cases} F_c = N_t F_0 \mathrm{pln}(k_{on}/(k_0 e)) & : \quad r \ll N_{eq} k_0 F_0 \text{ (slow loading)} \\ N_{eq} F_0 \ln\left(r/(N_{eq} k_0 F_0)\right) & : \quad r \gg N_{eq} k_0 F_0 \text{ (fast loading)} \end{cases} \tag{8.1}$$

where pln(a) denotes the product logarithm, which is defined as the solution x of $xe^x = a$. F_0 is the internal force scale of the molecular bond, $F_0 = k_B T / x_B$ (see section 2.2). Equation 8.1 shows that the rupture force is independent of the loading rate for slow loading. In the regime of fast loading, the rupture force is linearly related to the logarithm of loading rate, $\ln(r)$. In the equation for fast loading, N_{eq} denotes the stationary number of bonds at zero force, $N_{eq} = N_t k_0 / (k_0 + k_{on})$. This is the number of closed bonds when the force application starts. Rebinding is very unlikely to occur in this case and only defines the initial condition, but does not further influence the rupture force. A detailed description of this model is given in Erdmann (2005).

The result of the scaling analysis in (8.1) shows, that in both scaling regimes the rupture force depends on the cluster size, which is in turn assumed to be proportional to the area of the adhesion cluster: $N_t = A/A_0$. Therefore the relations for the rupture force per area read

$$F/A = \begin{cases} (F_0/A_0)\mathrm{pln}(k_{on}/(k_0 e)) & : \quad r \ll N_{eq} k_0 F_0 \text{ (slow loading)} \\ (F_0/A_0)\dfrac{k_0}{k_0 + k_{on}} \ln\left(\dfrac{r/A}{k_0 (F_0/A_0) \frac{k_0}{k_0 + k_{on}}}\right) & : \quad r \gg N_{eq} k_0 F_0 \text{ (fast loading)} \end{cases}$$

and can be simplified by introducing the parameters a, b and c to

$$F/A = \begin{cases} ac & : \quad \text{(slow loading)} \\ a \ln((r/A)/b) & : \quad \text{(fast loading)} \end{cases} \tag{8.2}$$

This shows that the rupture force per area, F/A, is only a function of r/A. The experimental results of F/A for focal contact ruptures on 28 nm and 51 nm nanopatterned substrates are plotted as a function of r/A in figure 8.13. In both graphs, the two scaling regimes can be identified and were fitted with (8.2). The analysis suggests that the rupture forces are independent of loading rate for the regime of slow loading (dashed line). On the other hand, the loading rate strongly affects rupture forces for fast loading (line).

From the data approximation the results for the parameters a, b and c on the two nanopatterns are:

$$\begin{aligned} a_{28\mathrm{nm}} &= 4.47\,\mathrm{nN/\mu m^2}\,, & a_{51\mathrm{nm}} &= 3.9\mathrm{nN/\mu m^2}\,, \\ b_{28\mathrm{nm}} &= 0.18\,\mathrm{nN/\mu m^2}\,, & b_{51\mathrm{nm}} &= 0.13\,\mathrm{nN/\mu m^2}\,, \\ c_{28\mathrm{nm}} &= 0.65\,, & c_{51\mathrm{nm}} &= 0.31 \end{aligned}$$

Thus also values for the original system parameters can be calculated:

	28 nm	51 nm
F_0/A_0	9.4 nN/µm^2	5.9 nN/µm^2
k_{on}/k_0	1.1	0.53
k_0	0.04	0.03
k_{on}	0.044	0.015

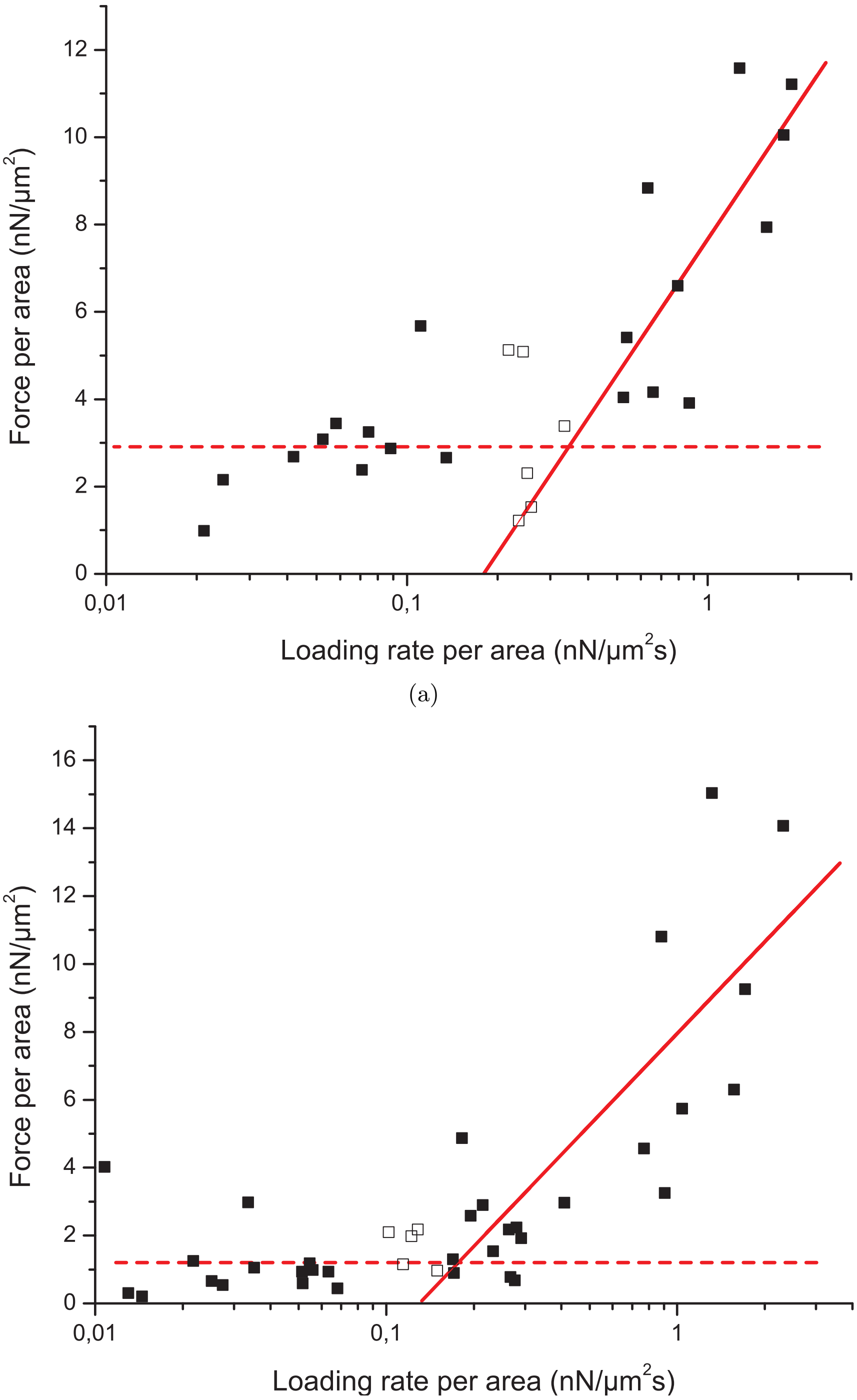

(a)

(b)

Figure 8.13: Dependence of the rupture forces of focal contacts on the loading rate, normalised to the cluster area. The values are shown for (a) 28 and (b) 51 nm integrin binding site spacing. The scaling functions were fitted to the data and the two regimes of slow loading (dashed line) and fast loading (line) can be identified. The empty squares were not taken into account for the fit in order to exclude values that are too close to the transition between the loading rate regimes. The error of a single data point is estimated to be approximately 10 % both in rupture force and loading rate.

The results obtained by this analysis are consistent. The unbinding rate k_0 is of the same order of magnitude for the two substrate types and the force constant per area, F_0/A_0, the ratio of rebinding rate to off-rate k_{on}/k_0 and the rebinding rate k_{on} decrease with increasing integrin binding site spacing. These results are in agreement with the picture that the adhesion cluster is stronger and more densly packed when the distance between integrin binding sites is small[5].

8.5 Unbinding Forces on Microstructured Substrates

Several studies of cell adhesion on microstructured substrates have been performed, in order to investigate effects on cell spreading, cytoskeleton organisation and adhesion strength (Chen et al., 1997; Lehnert et al., 2004; Gallant et al., 2005; Théry et al., 2006). Our decision to use micropatterned substrates was motivated by the need for well-defined cell and particularly cytoskeleton geometries. This was intended to lead to big improvements for determining loading rates, since the force distributions are expected to be more isotropic on such substrates.

The microstructured substrates used in our study consisted of micrometre sized gold circles on a glass slide and were kindly provided by Marcus Abel and prepared according to the procedure given in section 3.4. The passivation of the glass background was performed with PLL-g-PEG followed by a biofunctionalisation of the gold circles with the RGD thiol (see section 3.2 and 3.3.2), leading to homogeneously coated RGD circles on a passivated background. Figure 8.14 a shows cells spread for approximately 4 hours on microstructures with a microcircle diameter of 9 µm and a microcircle edge-to-edge distance of 20 µm.

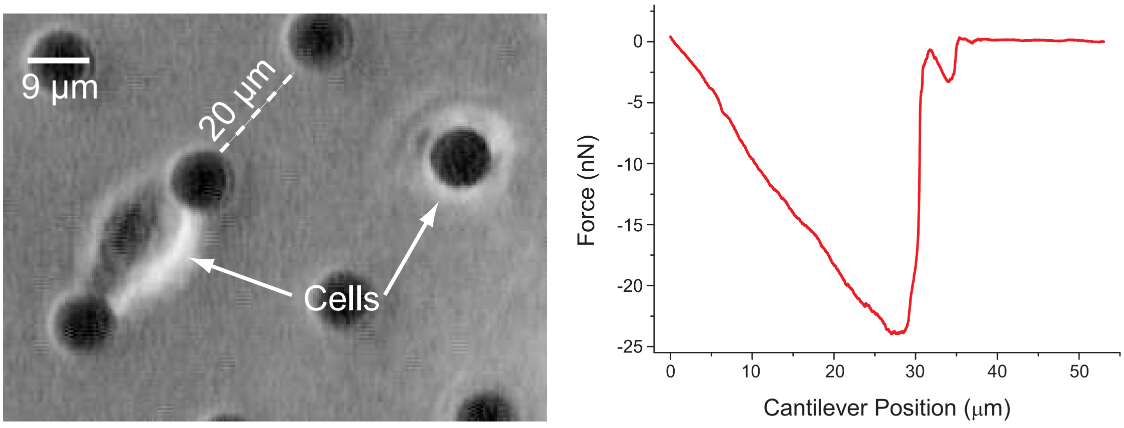

(a) (b)

Figure 8.14: (a) Cells adhering to RGD-functionalised gold microcircles are of an elongated or spherical shape. In this example the adhesion time was 4 hours. (b) Force curve for a cell detachment from a single microcircle.

These microstructure parameters were chosen, since cell culture experiments have shown that cells are either attached to only one microcircle or linearly clamped in between two microcircles after 3-4 hours of adhesion. Such cell geometries would definitely be very

---

[5] This analysis was performed together with Thorsten Erdmann (BIOMS, Heidelberg), who developed the employed theoretical model during his PhD.

convenient, since they could allow a simple analysis of the distribution of loading rates and forces inside the cell.

Figure 8.14 b shows a force curve typical for a cell detachment from a single microcircle. In this example, a single cell was stretched over a distance of about 30 µm, a length almost twice as large as the cell diameter. After this stretching phase the cell left the substrate with a single force step, followed by a second, much smaller step. Since the cell diameter is larger than the microcircle size, we assumed a full occupation of the microcircle by cell adhesion contacts, thus the rupture force was normalised to the microcircle area.

Figure 8.15 a gives the force per detached area for RGD microcircles and compares it with the forces obtained from nanopatterned substrates with (d=50 nm) and without (d=90 nm) focal contact formation. The results show that the detachment forces on the microcircles lies between the values for 50 and 90 nm nanopatterns, although homogeneous RGD substrates support focal contact formation and an adhesion strength being at least comparable to those on a 50 nm nanopattern was expected. This result suggests an incomplete focal contact formation on the microstructures. Results on the cell elasticity support this finding, as shown in figure 8.15 b. The spring constant of cells on microstructures is comparable to that on a 90 nm nanopattern, suggesting that the actin network is equivalently badly organised on the microstructured substrates.

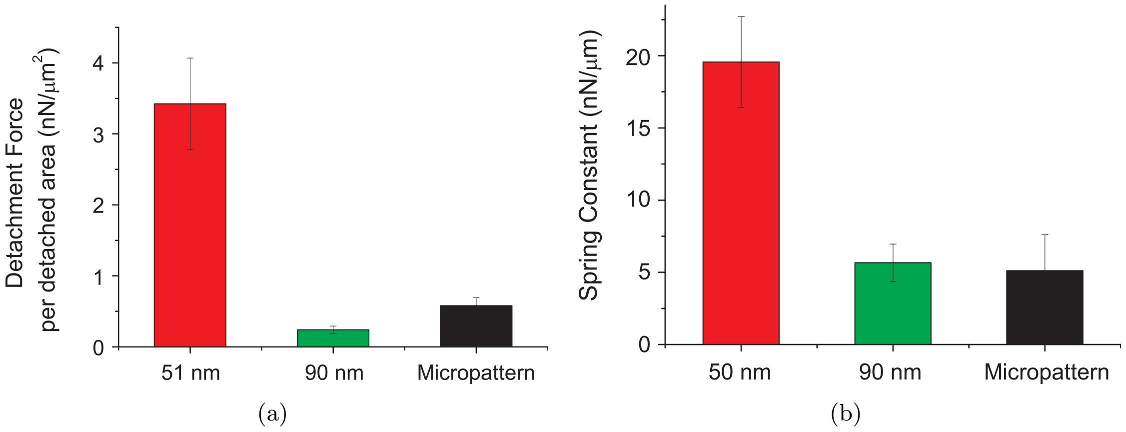

(a) (b)

Figure 8.15: (a) Detachment forces and (b) cell elasticity on microstructures compared to nanopatterned substrates. Error bars refer to the standard error in the mean.

The fluorescence image of YFP labelled paxillin on such microstructures finally proves that no focal contacts are formed, instead, the paxillin is homogeneously distributed over the whole cell body (figure 8.16).

The received data on microstructures agree qualitatively with studies reported in literature. The apoptosis rate of endothelial cells is strongly enhanced if binding sites are situated far apart from each other (Chen et al., 1997). In fibroblasts, a well-organised cytoskeleton is only formed for a centre-to-centre spacing of less than 25 µm of fibronectin micropatterns (Lehnert et al., 2004). This spatial condition is almost fulfilled on our patterns, but since RGD does not promote adhesion as well as fibronectin and a different cell type was used, the microstructure parameters probably have to be adapted to the particular experimental conditions in order to provide substrates which support cell adhesion. So far, the cell shape cannot be controlled without harming adhesion. As soon as appropriate parameters are found, an ideal platform for studying physical adhesion properties

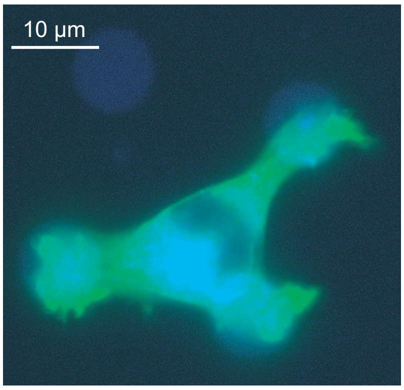

Figure 8.16: YFP Pax fluorescence of REF cells on a microstructure after an adhesion time of 24 hours in DMEM containing 1 % FBS. This image was kindly provided by Ada Cavalcanti-Adam.

is created, since many parameters such as (visco)elasticity, loading rate and adhesion area will then be clearly defined.

8.6 Discussion

With our approach to measuring long-term detachment forces, we showed for the first time that it is possible to quantify long-term adhesion at the single-cell and sub-cellular level. This could have many applications, on the one hand for further studying the adhesion properties of integrins and many other protein systems, on the other hand also for quantifying adhesion properties of implants in pre-clinical studies.

Although the complete cell system is much too complex to understand in detail, the presented results show the striking effect of nanopatterned substrates on cell adhesion and most importantly, the cooperative increase of the local cell detachment forces due to focal contact formation. An additional analysis of adhesion cluster strength provided a further understanding of the mechanical properties of focal contacts. As a first result, a linear relationship between focal contact size and detachment force was found. A loading rate analysis of the rupture forces of focal contacts allowed to relate our data to a model describing the rupture forces as a function of loading rate. With this analysis it was for the first time possible to identify the theoretically predicted scaling regimes.

For future experiments, an approach to controlling the cell geometry is desirable, in order to simplify the data interpretation. Additionally, cells which are carrying fluorescently labelled actin could be employed, for optically giving insight into the distribution of forces in the cytoskeleton. The experimental handling and the data analysis are now well-established so that the experiments presented in this thesis have hopefully paved the way for multiple far-reaching investigations of cell adhesion strength.

Conclusions

The main focus of this work was the investigation of adhesion processes on biofunctionalised nanopatterned substrates.

In an initial study, streptavidin functionalised nanopatterns were used as devices with defined, tunable surface energies. The surface energy of these substrates was obtained by measuring the adhesion-induced deformation of biotinylated elastic probes with a microinterferometric technique. In these experiments, the surface energy could be varied by a factor of 5.3 by employing nanopatterned substrates (see chapter 5).

RICM, the microinterferometric technique set-up in this study, was additionally used for studying cell adhesion processes, which take place in close proximity to the surface. In this way it was possible to observe how cells explore the substrates with microspikes prior to forming tight adhesion zones. The geometry of these microspikes could be derived from the RICM images and it turned out that they point out straight from the cell (section 6.1). Additionally, a two-colour RICM setup was used to receive information on the size of the gap between cell and nanopatterned substrate in the focal contact region. These results indicate a curvature of either the cell membrane or the bottom of the focal contact protein patch, in agreement with results from scanning electron microscopy (section 6.4). A project arising in the course of the investigations was the comparison of cell spreading on nanopatterns with a recently developed mathematical model. For cells spreading on biofunctionalised nanopatterns it turned out that for small integrin binding site spacings three spreading phases can be identified, whereas large integrin binding site spacings destroy the normal course of cell spreading. Instead of the three distinct spreading phases, then repeated protrusion-retraction cycles are observed (section 6.2).

The most important part of this thesis are studies concerning the dependence of cell adhesion strength on the distance of single integrin binding sites (see chapters 7 and 8). By setting up magnetic tweezers and establishing experimental routines for AFM measurements on live cells, it was possible to study the dependence of cell detachment forces on integrin binding site spacing for timescales of a few seconds and several hours. The novel methods developed for studying long-term adhesion forces pave the way to a completely new class of cell experiments with AFM, which can be easily transferred to other cell adhesion systems and could arise to an important tool of future long-term adhesion studies. The studies presented in this thesis provide information on the formation of integrin-mediated adhesion clusters. It could be shown that variations in the distance of integrin binding sites indeed strongly affect cell adhesion strength both for adhesion times of a few seconds and several hours. In short-term adhesion experiments, information on the stability of single-molecule bonds and on viscoelastic cell properties could be gained. Most importantly, these experiments allowed to characterise early events of adhesion cluster formation. There it turned out that the distance of integrin binding sites influences adhesion strength already after a few seconds of cell-substrate contact. The cooperative increase in adhesion strength for substrates with integrin binding site spacings smaller than 70 nm is observed in initial adhesion experiments for cell-substrate contact times of less than five minutes. This phenomenon is ascribed to a restricted adhesion cluster formation for integrin binding site spacings of 70 nm and more, since then a cell-internal linkage of integrins might fail. This idea was successfully introduced into a theoretical model, which is able to describe the course of early adhesion cluster formation and approximates the experimental data. In the long-term adhesion studies, nanopatterned substrates were used to trigger focal contact formation. With the force experiments the local increase of detachment forces upon focal contact formation was revealed and the rupture forces of single focal contacts were measured. These data could be interpreted in the framework of an adhesion cluster theory. Thus, the experiments performed in this thesis contribute to an increased understanding of how variations in integrin binding site spacing affect cell adhesion and in particular the formation and strength of adhesion clusters.

List of Figures

Bibliography

Adams, J. C. (2001). Cell-matrix contact structures. *Cell. Mol. Life Sci.*, 58:371–392.

Akiyama, S. K. and Yamada, K. M. (1985). The interaction of plasma fibronectin with fibroblastic cells in suspension. *J. Biol. Chem.*, 260(7):4492–4500.

Albersdörfer, A. and Sackmann, E. (1999). Swelling behavior and viscoelasticity of ultrathin grafted hyaluronic acid films. *Eur. Phys. J. B*, 10:663–672.

Alberts, B., Bray, D., Johnson, A., Lewis, J., Raff, M., Roberts, K., and Walter, P. (1997). *Essential Cell Biology. An Introduction to the Molecular Biology of the Cell.* Garland Publishing, New York.

Albrecht-Buehler, G. (1976). Filopodia of spreading 3T3 cells: do they have a substrate exploring function? *J. Cell Biol.*, 69:275–286.

Albrecht-Buehler, G. and Goldman, R. D. (1976). Microspike-mediated particle transport towards the cell body during early spreading of 3t3 cells. *Exp. Cell Res.*, 97:329–339.

Arnold, M. (2005). *Molecularly Defined Nanostructured Interfaces as Tools for the Regulation and Measurement of Functional Length Scales in Cell Adhesion Mediating Protein Clusters*. PhD thesis, Universität Heidelberg.

Arnold, M., Cavalcanti-Adam, E. A., Glass, R., Blümmel, J., Eck, W., Kantlehner, M., Kessler, H., and Spatz, J. P. (2004). Activation of integrin function by nanopatterned adhesive interfaces. *ChemPhysChem*, 5:383–388.

Balaban, N., Schwarz, U., Riveline, D., Goichberg, P., Tzur, G., Sabanay, I., Mahalu, D., Safran, S., Bershadsky, A., Addadi, L., and Geiger, B. (2001). Force and focal adhesion assembly: a close relationship studied using elastic micropatterned substrates. *Nature Cell Biology*, 3:466–472.

Ballestrem, C., Hinz, B., Imhof, B. A., and Wehrle-Haler, B. (2001). Marching at the front and dragging behind: differential $\alpha v\beta 3$-integrin turnover regulates focal adhesion behavior. *J. Cell Biol.*, 155(7):1319–1332.

Bausch, A. R., Möller, W., and Sackmann, E. (1999). Measurement of local viscoelasticity and forces in living cells by magnetic tweezers. *Biophys. J.*, 76:573–579.

Bausch, A. R., Ziemann, F., Boulbitch, A. A., Jacobson, K., and Sackmann, E. (1998). Local measurements of viscoelastic parameters of adherent cell surfaces by magnetic bead microrheometry. *Biophys. J.*, 75:2038–2049.

Bayas, M. V., Leung, A., Evans, E., and Leckband, D. (2006). Lifetime measurements reveal kinetic differences between homophilic cadherin bonds. *Biophys. J.*, 90:1385–1395.

Beckerle, M. C. (2002). *Cell Adhesion.* Oxford University Press.

Bell, G. I. (1978). Models for the specific adhesion of cells to cells. *Science*, 278:618–627.

Beningo, K. A., Dembo, M., and Y.-L., W. (2004). Responses of fibroblasts to anchorage of dorsal extracellular matrix receptors. *Proc. Natl. Acad. Sci. USA*, 101(52):18024–18029.

Benoit, M. (2000). *Kraftspektroskopie an lebenden Zellen.* PhD thesis, Universität München.

Benoit, M. (2002). Cell adhesion measured by force spectroscopy on living cells. *Methods in Cell Biology*, 68:91–114.

Benoit, M., Gabriel, D., Gerisch, G., and Gaub, H. (2000). Discrete interactions in cell adhesion measured by single-molecule force spectroscopy. *Nature Cell Biology*, 2:313–317.

Benoit, M. and Gaub, H. (2002). Measuring cell adhesion forces with the atomic force microscope at the molecular level. *Cells Tissues Organs*, 172:174–189.

Besser, A. and Safran, S. A. (2006). Force-induced adsorption and anisotropic growth of focal adhesions. *Biophys. J.*, 90:3469–3484.

Binnig, G., Quate, C. F., and Gerber, C. (1986). Atomic force microscopy. *Phys. Rev. Lett.*, 56(9):930–933.

Binnig, G., Rohrer, H., Gerber, C., and Weibel, E. (1982). Surface studies by scanning tunneling microscopy. *Phys. Rev. Lett.*, 49(1):57–61.

Blau, H. and Baltimore, D. (1991). Differentiation requires continuous regulation. *J. Cell Biol.*, 112:781–783.

Blümmel, J. (2005). *Entwicklung biofunktionalisierter Nanostrukturen an Grenzflächen zur Untersuchung der Kinetik des molekularen Motorproteins Eg5.* PhD thesis, Universität Heidelberg.

Boal, D. (2002). *Mechanics of the Cell.* Cambridge University Press.

Boulbitch, A., Guttenberg, Z., and Sackmann, E. (2001). Kinetics of membrane adhesion mediated by ligand-receptor interaction studied with a biomimetic system. *Biophys. J.*, 81:2743–2751.

Brown, K. R. and Natan, M. J. (1998). Hydroxylamine seeding of colloidal au nanoparticles in solution and on surfaces. *Langmuir*, 14:726–728.

Calderwood, D. A. (2004). Talin controls integrin activation. *Biochemical Society Transactions*, 32(3):434–437.

Cavalcanti-Adam, E. A., Volberg, T., Micoulet, A., Kessler, H., Geiger, B., and Spatz, J. P. (2006). Cell spreading and focal adhesion dynamics are affected by surface spacing of integrin ligands. *Biophys. J.*, submitted.

Chamaraux, F., Fache, S., Bruckert, F., and Fourcade, B. (2005). Kinetics of cell spreading. *Phys. Rev. Lett.*, 94:158102.

Chen, C., Mrksich, M., Huang, S., Whitesides, G., and Ingber, D. (1997). Geometric control of cell life and death. *Science*, 276:1425–1428.

Choquet, D., P., F. D., and Sheetz, M. P. (1997). Extracellular matrix rigidity causes strengthening of integrin-cytoskeleton linkages. *Cell*, 88:39–48.

Chu, L., Tempelman, L. A., Miller, C., and Hammer, D. A. (1994). Centrifugation assay of IgE-mediated cell-adhesion to antigen-coated gels. *AICHE J.*, 40:692–703.

Chu, Y.-S., Thomas, W., Eder, O., Pincet, F., Perez, E., Thiery, J., and Dufour, S. (2004). Force measurements in E-cadherin-mediated cell doublets reveal rapid adhesion strengthened by actin cytoskeleton remodeling through Rac and Cdc42. *J. Cell Biol.*, 167:1183–1194.

Cleveland, J., Manne, S., Bocek, D., and Hansma, P. (1993). A nondestructive method for determining the spring constant of cantilevers for scanning force microscopy. *Rev. Sci. Instrum.*, 64(2):403–405.

Cluzel, C., Saltel, F., Lussi, J., Paulhe, F., Imhof, B. A., and Wehrle-Haller, B. (2005). The mechanisms and dynamics of $\alpha_v\beta_3$ integrin clustering in living cells. *J. Cell Biol.*, 171(2):383–392.

Cohen, M., Kam, Z., Addadi, L., and Geiger, B. (2006). Dynamic study of the transition from hyaluronan to integrin-mediated adhesion in chondrocytes. *EMBO J.*, 25:302–311.

Cohen, M., Klein, E., Geiger, B., and Addadi, L. (2003). Organization and adhesive properties of the hyaluronan pericellular coat of chondrocytes and epithelial cells. *Biophys. J.*, 85:1996–2005.

Courtney, T. H. (1990). *Mechanical behavior of materials*. McGraw-Hill, Inc.

Critchley, D. (2000). Focal adhesions - the cytoskeletal connection. *Curr. Opin. Cell Biol.*, 12:133–139.

Critchley, D. R. (2004). Cytoskeletal proteins talin and vinculin in integrin-mediated adhesion. *Bioch. Soc. Trans.*, 32(5):831–836.

Cukierman, E., Pankov, R., and Yamada, K. M. (2002). Cell interactions with three-dimensional matrices. *Curr. Opin. Cell Biol*, 14:633–639.

Dahlin, A., Zäch, M., Rindzevicius, T., Käll, M., Sutherland, D., and Höök, F. (2005). Localized surface plasmon resonance sensing of lipid-membrane-mediated biorecognition events. *J. Am. Chem. Soc.*, 127(14):5043–5048.

Desprat, N., Richert, A., Simeon, J., and Asnacios, A. (2005). Creep function of a single living cell. *Biophys. J.*, 88:2224–2233.

Discher, D. E., Janmey, P., and Wang, Y.-L. (2005). Tissue cells feel and respond to the stiffness of their substrate. *Science*, 310:1139–1143.

Döbereiner, H.-G., Dubin-Thaler, B., Giannone, G., Xenias, H. P., and Sheetz, M. P. (2004). Dynamic phase transitions in cell spreading. *Phys. Rev. Lett.*, 93(10):108105.

Domke, J. and Radmacher, M. (1998). Measuring the elastic properties of thin polymer films with the atomic force microscope. *Langmuir*, 14:3320–3325.

Dwir, O., Solomon, A., Mangan, S., Kansas, G. S., Schwarz, U. S., and Alon, R. (2003). Avidity enhancement of L-selectin bonds by flow: shear-promoted rotation of leukocytes turn labile bonds into functional tethers. *J. Cell Biol.*, 163(3):649–659.

Efremova, N. V., Sheth, S. R., and Leckband, D. E. (2001). Protein-induced changes in poly(ethylene glycol) brushes: molecular weight and temperature dependence. *Langmuir*, 17:7628–7636.

Erdmann, T. (2005). *Stochastic dynamics of adhesion clusters under force.* PhD thesis, Universität Potsdam.

Erdmann, T. and Schwarz, U. S. (2004a). Adhesion clusters under shared linear loading: A stochastic analysis. *Europhys. Lett.*, 66(4):603–609.

Erdmann, T. and Schwarz, U. S. (2004b). Stability of adhesion clusters under constant force. *Phys. Rev. Lett.*, 92(10):108102.

Erdmann, T. and Schwarz, U. S. (2006). Bistability of cell-matrix adhesions resulting from nonlinear receptor-ligand dynamics. *Biophys. J.*, 91:L60.

Evans, E. (2001). Probing the relation between force-lifetime and chemistry in single molecule bonds. *Annu. Rev. Biophys. Biomol. Struct.*, 30:105–128.

Evans, E. and Ritchie, K. (1997). Dynamic strength of molecular adhesion bonds. *Biophys. J.*, 72:1541–1555.

Fabry, B., Maksym, G. N., Butler, J. P., Glogauer, M., Navajas, D., and Fredberg, J. J. (2001). Scaling the microrheology of living cells. *Phys. Rev. Lett.*, 87(14):148102.

Feneberg, W., Aepfelbacher, M., and Sackmann, E. (2004). Microviscoelasticity of the apical cell surface of human umbilical vein endothelial cells (HUVEC) within confluent monolayers. *Biophys. J.*, 87:1338–1350.

Fernández, P., Pullarkat, P. A., and Ott, A. (2006). A master relation defines the nonlinear viscoelasticity of single fibroblasts. *Biophys. J.*, 90:3796–3805.

Florin, E.-L., Moy, V. T., and Gaub, H. E. (1994). Adhesion forces between individual ligand-receptor pairs. *Science*, 264:415–417.

Forero, M., Thomas, W. E., Bland, C., Nilsson, L. M., Sokurenko, E. V., and Vogel, V. (2004). A catch-bond based nanoadhesive sensitive to shear stress. *Nano Lett.*, 4(9):1593–1597.

Fung, Y. C. (1981). *Biomechanics; Mechanical Properties of Living Tissues.* Springer, Heidelberg.

Gallant, N. D., Michael, K. E., and Garcia, A. J. (2005). Cell adhesion strengthening: Contributions of adhesive area, integrin binding, and focal adhesion assembly. *Mol. Biol. Cell*, 16:4329–4340.

Garcia, A. J. and Boettiger, D. (1999). Integrin-fibronectin interactions at the cell-material interface: initial integrin binding and signaling. *Biomaterials*, 20:2427–2433.

Gingell, D. and Todd, I. (1979). Interference reflection microscopy: a quantitative theory for image interpretation and its application to cell–substratum separation measurements. *Biophys. J.*, 26:507–526.

Glass, R., Möller, M., and Spatz, J. P. (2003). Block copolymer micelle nanolithography. *Nanotechnology*, 14:1153–1160.

Gönnenwein, S. (2003). *Generic and Specifc Cell Adhesion: Investigations of a Model System by Micro-Interferometry.* PhD thesis, Technische Universität München.

Gönnenwein, S., Tanaka, M., Hu, B., Moroder, L., and Sackmann, E. (2003). Functional incorporation of integrins into solid supported membranes on ultrathin films of cellulose: Impact on adhesion. *Biophys. J.*, 85:646–655.

Gosse, C. and Croquette, V. (2002). Magnetic tweezers: Micromanipulation and force measurement at the molecular level. *Biophys. J.*, 82:3314–3329.

Grandbois, M., Beyer, M., Rief, M., Clausen-Schaumann, H., and E., G. H. (1999). How strong is a covalent bond? *Science*, 283:1727–1730.

Green, N. (1990). *Avidin and Streptavidin, Avidin-Biotin Technology, Methods in Enzymology.* Academic Press Inc., San Diego.

Hänggi, P., Talkner, P., and Borkovec, M. (1990). Reaction-rate theory: fifty years after Kramers. *Rev. Mod. Phys.*, 62:251–341.

Haubner, R., Finsinger, D., and Kessler, H. (1997). Stereoisomere Peptid-Bibliotheken und Peptidmimetika zum Design von selektiven Inhibitoren des $\alpha_v\beta_3$-Integrins für eine neuartige Krebstherapie. *Angew. Chem.*, 109:1441–1456.

Hertz, H. (1882). Über die Berührung fester elastischer Körper. *J. Reine Angew. Mathematik*, 92:156–171.

Heuberger, M., Drobek, T., and Spencer, N. D. (2005). Interaction forces and morphology of a protein-resistant poly(ethylene glycol) layer. *Biophys. J.*, 88:495–504.

Höfling, F., Franosch, T., and Frey, E. (2006). Localization transition of the 3D Lorentz model and continuum percolation. *Phys. Rev. Lett.*, 96:165901.

Hu, B., Finsinger, D., Peter, K., Guttenberg, Z., Bärmann, M., Kessler, H., Escherisch, A., Moroder, L., Böhm, J., Baumeister, W., Sui, S., and Sackmann, E. (2000). Intervesicle cross-linking with integrin $\alpha_{IIb}\beta_3$ and cyclic-RGD-lipopeptide. *Biochemistry*, 39(40):12284–12294.

Huang, N. P., Vörös, J., De Paul, S. M., Textor, M., and Spencer, N. D. (2002). Biotin-derivatized poly(L-lysine)-g-poly(ethylene glycol): A novel polymeric interface for bioaffinity sensing. *Langmuir*, 18:220–230.

Hutter, J. L. and Bechhofer, J. (1994). Calibration of atomic-force microscope tips. *Rev. Sci. Instrum.*, 64:1868–1873.

Hynes, R. O. (1999). Cell adhesion: old and new questions. *Trends Cell Biol.*, 9(12):M33–M37.

Hynes, R. O. (2002). Integrins: bidirectional, allosteric signaling machines. *Cell*, 110:673–687.

Iwanaga, Y., Braun, D., and Fromherz, P. (2001). No correlation of focal contacts and close adhesion by comparing GFP-vinculin and fluorescence interference in DiI. *Eur. Biophys. J.*, 30:17–26.

Jakubick, V. C. (2005). Zelladhäsion auf Nanoabstandsgradienten innerhalb Goldpartikel-strukturierter Oberflächen. Master's thesis, Universität Heidelberg.

Jiang, G., Giannone, G., Critchley, D. R., Fukumoto, E., and Sheetz, M. P. (2003). Two-piconewton slip bond between fibronectin and the cytoskeleton depends on talin. *Nature*, 424:334–337.

Johnson, E., Berk, D., Jain, R., and Deen, W. (1995). Diffusion and partitioning of proteins in charged agarose gels. *Biophys. J.*, 68:1561–1568.

Johnson, K. (1985). *Contact Mechanics.* Cambridge University Press, Cambridge.

Johnson, K., Kendall, K., and Roberts, A. (1971). Surface energy and the contact of elastic solids. *Proc. R. Soc. Lond. A.*, 324:301–313.

Johnson, K. L. and Greenwood, J. A. (1997). An adhesion map for the contact of elastic spheres. *J. Colloid Interface Sci.*, 192:326–333.

Kantlehner, M., Schaffner, P., Finsinger, D., Meyer, J., Jonczyk, A., Diefenbach, B., Nies, B., Hölzemann, G., Goodman, S. L., and Kessler, H. (2000). Surface coating with cyclic RGD peptides stimulates osteoblast adhesion and proliferation as well as bone formation. *ChemBioChem*, 1:107–114.

Kassing, R., Käsmeier, R., and Rangelow, I. W. (2000). Lithographie der nächsten Generation. *Physikal. Blätt.*, 56(2):31–36.

Katz, B. Z., Zamir, E., Bershadsky, A., Kam, Z., Yamada, K. M., and Geiger, B. (2000). Physical state of the extracellular matrix regulates the structure and molecular composition of cell-matrix adhesions. *Mol. Biol. Cell*, 11:1047–1060.

Koo, L., Irvine, D., A.M., M., Lauffenburger, D., and Griffith, L. (2002). Co-regulation of cell adhesion by nanoscale RGD organization and mechanical stimulus. *J. Cell Sci.*, 115:1423.

Kramers, H. A. (1940). Brownian motion in a field of force. *Physica*, 7:284–304.

Landau, L. (1991). *Theoretische Physik: Elastizitätstheorie.* Harri Deutsch, Frankfurt am Main.

Laurent, T. (1967). Determination of the structure of agarose gels by gel chromatography. *Biochim. Biophys. Acta*, 136:199–205.

Lehnert, D., Wehrle-Haller, B., David, C., Weiland, U., Ballestrem, C., Imhof, B. A., and Bastmeyer, M. (2004). Cell behaviour on micropatterned substrata: limits of extracellular matrix geometry for spreading and adhesion. *J. Cell Sci.*, 117:41–52.

Li, F., Redick, S. D., Erickson, H. P., and Moy, V. T. (2003a). Force measurements of the $\alpha_5\beta_1$ integrin–fibronectin interaction. *Biophys. J.*, 84:1252–1262.

Li, R., Mitra, N., Gratkowski, H., Vilaire, G., Litvinov, R., Nagasami, C., Weisel, J. W., Lear, J. D., DeGrado, W. F., and Bennett, J. S. (2003b). Activation of integrin αIIβ3 by modulation of transmembrane helix associations. *Science*, 300:795–798.

Lodish, H., Berk, A., Zipursky, S. L., Matsudaira, P., Baltimore, D., and Darnell, J. E. (1999). *Molecular Cell Biology.* W. H. Freeman and Company, New York.

Lussi, J. W., Falconnet, D., Hubbell, J. A., Textor, M., and Csucsd, G. (2006). Pattern stability under cell culture conditions – a comparative study of patterning methods based on PLL-g-PEG background passivation. *Biomaterials*, 27:2534–2541.

Maheshwari, G., Brown, G., Lauffenburger, D., Wells, A., and Griffith, L. (2000). Cell adhesion and motility depend on nanoscale RGD clustering. *J. Cell Sci.*, 113:1677–1686.

Massia, S. P. and Hubbell, J. A. (1991). An RGD spacing of 440 nm is sufficient for integrin $\alpha_v\beta_3$-mediated fibroblast spreading and 140 nm for focal contact and stress fiber formation. *J. Cell Biol.*, 114(5):1089–1100.

Matthews, B. D., Overby, D. R., Alenghat, F. J., Karavitis, J., Numaguchi, Y., Allen, P. G., and Ingber, D. E. (2004). Mechanical properties of individual focal adhesions probed with a magnetic microneedle. *Biochem. Biophys. Res. Comm.*, 313:758–764.

Merkel, R., Nassoy, P., Leung, A., Ritchie, K., and Evans, E. (1999). Energy landscapes of receptor ligand bonds explored with dynamic force spectroscopy. *Nature*, 397:50–53.

Metzger, R., Xu, T., and Peterson, I. (2001). Electrical rectification by a monolayer of hexadecylquinolinium tricyanoquinodimethanide measured between macroscopic gold electrodes. *J. Phys. Chem. B*, 105:7280–7290.

Micoulet, A. (2004). *Uniaxial Mechanical Assays on Adherent Living Single Cells: Animal Embryonic Fibroblasts and Human Pancreas Cancer Cells.* PhD thesis, Universität Heidelberg.

Miyamoto, S., Akiyama, S., and Yamada, K. M. (1995). Synergistic roles for receptor occupancy and aggregation in integrin transmembrane function. *Science*, 267:883–885.

Moy, V., Jiao, Y., Hillman, T., Lehmann, H., and Sano, T. (1999). Adhesion energy of receptor-mediated interaction measured by elastic deformation. *Biophys. J.*, 76:1632–1638.

Nguyen-Duong, M., Koch, K., and Merkel, R. (2003). Surface anchoring reduces the lifetime of single specific bonds. *Europhys. Lett.*, 61(6):845–851.

Nicolas, A. and Safran, S. A. (2004). Elastic deformations of grafted layers with surface stress. *Phys. Rev. E*, 69:051902.

Palecek, S. P., Huttenlochner, A., Horwitz, A. F., and Lauffenburger, D. A. (1998). Physical and biochemical regulation of integrin release during rear detachment of migrating cells. *J. Cell Sci.*, 111:929–940.

Pasche, S., Textor, M., Meagher, L., Spencer, N. D., and Griesser, H. J. (2005). Relationship between interfacial forces measured by colloid–probe atomic force microscopy and protein resistance of poly(ethylene glycol)-grafted poly(L-lysine) adlayers on niobia surfaces. *Langmuir*, 21:6508–6520.

Pfaff, M., Tangemann, K., Gurrath, M., Müller, G., , Kessler, H., Timpl, R., and Engel, J. (1994). Selective recognition of cyclic RGD peptides of NMR defined conformation by αIIbβ3, αVβ3, and α5β1 integrins. *J. Biol. Chem.*, 269:20223–20238.

Picart, C., Sengupta, K., Schilling, J., Maurstad, G., Ladam, G., Bausch, A. R., and Sackmann, E. (2004). Microinterferometric study of the structure, interfacial potential, and viscoelastic properties of polyelectrolyte multilayer films on a planar substrate. *J. Phys. Chem. B*, 108:7196–7205.

Pierschbacher, M. D. and Ruoslahti, E. (1984). Variants of the cell recognition site of fibronectin that retain attachment-promoting activity. *Proc. Natl. Acad. Sci. USA*, 81:5985–5988.

Ploem, J. (1975). *Reflection Contrast microscopy as a tool for investigation of the attachment of living cells to a glass surface.* Blackwell Scientific Publications, Oxford.

Pompe, T., Renner, L., and Werner, C. (2005). Nanoscale features of fibronectin fibrillogenesis depend on protein-substrate interaction and cytoskeleton structure. *Biophys. J.*, 88:527–534.

Prechtel, K., Bausch, A. R., Marchi-Artzner, V., Kantlehner, M., Kessler, H., and Merkel, R. (2002). Dynamic force spectroscopy to probe adhesion strength of living cells. *Phys. Rev. Lett.*, 89(2):028101.

Puech, P.-H., Taubenberger, A., Ulrich, F., Krieg, M., Müller, D., and Heisenberg, C.-P. (2005). Measuring cell adhesion forces of primary gastrulating cells from zebrafish using atomic force microscopy. *J. Cell Sci.*, 118:4199.

Rädler, J. and Sackmann, E. (1992). On the measurement of weak repulsive and frictional colloidal forces by reflection interference contrast microscopy. *Langmuir*, 8(3):848–853.

Radmacher, M., Tillmann, R. W., Fritz, M., and Gaub, H. E. (1992). From molecules to cells: Imaging soft samples with the atomic force microscope. *Science*, 257:1900–1905.

Reinhart-King, C. A., Dembo, M., and Hammer, D. A. (2005). The dynamics and mechanics of endothelial cell spreading. *Biophys. J.*, 89:676–689.

Rief, M., Gautel, M., Oesterhelt, F., Fernandez, J. M., and Gaub, H. E. (1997). Reversible unfolding of individual titin immunoglobulin domains by AFM. *Science*, 276:1109–1112.

Riveline, D., Zamir, E., Balaban, N. Q., Schwarz, U. S., Ishizaki, T., Narumiya, S., Kam, Z., Geiger, B., and Bershadsky, A. D. (2001). Focal contacts as mechanosensors: Externally applied local mechanical force induces growth of focal contacts by an mDia1-dependent and ROCK-independent mechanism. *J. Cell Biol.*, 153(6):1175–1185.

Ruiz-Taylor, L. A., Martin, T. L., Zaugg, F. G., Witte, K., Indermuhle, P., Nock, S., and Wagner, P. (2001). Monolayers of derivatized poly(L-lysine)-grafted poly(ethylene glycol) on metal oxides as a class of biomolecular interfaces. *Proc. Natl. Acad. Sci. USA*, 98:852–857.

Sackmann, E. and Bruinsma, R. F. (2002). Cell adhesion as wetting transition? *ChemPhysChem*, 3:262–269.

Sawhney, A. S. and Hubbell, J. A. (1992). Poly(ethyleneoxide)-graft-poly(L-lysine) copolymers to enhance the biocompatibility of poly(L-lysine)-alginate microcapsule membranes. *Biomaterials*, 13:863–70.

Schilling, J., Sengupta, K., Gönnenwein, S., Bausch, A. R., and Sackmann, E. (2004). Absolute interfacial distance measurements by dual-wavelength reflection interference contrast microscopy. *Phys. Rev. E*, 69:021901.

Schwarz, U. S. (2006). Stochastic dynamics of biomolecular bonds under force. *(unpublished)*.

Seifert, U. (2002). Dynamic strength of adhesion molecules: Role of rebinding and self-consistent rates. *Europhys. Lett.*, 58(5):792–798.

Selhuber, C., Czerwinski, F., Blümmel, J., and Spatz, J. P. (2006). Tuning surface energies with nanopatterned substrates. *Nano Lett.*, 6(2):267–270.

Shillcock, J. and Seifert, U. (1998). Escape from a metastable well under a time-ramped force. *Phys. Rev. E*, 57(6):7301–7304.

Simson, R., Wallraff, E., Faix, J., Niewöhner, J., Gerisch, G., and Sackmann, E. (1998). Membrane bending modulus and adhesion energy of wild-type and mutant cells of dictyostelium lacking talin or cortexillins. *Biophys. J.*, 74:514–522.

Slizskaia, I. (2005). Biofunktionalisierung von nanostrukturierten Oberflächen für eine kontrollierte Vesikeladhäsion. Master's thesis, Universität Heidelberg.

Smith, A.-S., Lorz, B., Gönnenwein, S., and Sackmann, E. (2006a). Force–controlled equilibria of specific vesicle–substrate adhesion. *Biophys. Lett.*, 90:L52–L54.

Smith, A.-S., Lorz, B., Seifert, U., and Sackmann, E. (2006b). Antagonist–induced deadhesion of specifically adhered vesicles. *Biophys. J.*, 90:1064–1080.

Smith, A.-S. and Seifert, U. (2005). Force-induced de-adhesion of specifically bound vesicles: Strong adhesion in competition with tether extraction. *Langmuir*, 21:11357.

Spatz, J. P., Mößmer, S., Hartmann, C., Möller, M., Herzog, T., Krieger, M., Boyen, H., Ziemann, P., and Kabius, B. (2000). Ordered deposition of inorganic clusters from micellar block copolymer films. *Langmuir*, 16:407–415.

Spatz, J. P., Mößmer, S., and Möller, M. (1996). Mineralization of gold nanoparticles in a block copolymer microemulsion. *Chem. Eur. J.*, 2:1552–1555.

Stenger, D. A., Georger, J. H., Dulcey, C. S., Hickman, J. J., Rudolph, A. S., Nielsen, T. B., McCort, S. M., and Calvert, J. M. (1992). Coplanar molecular assemblies of amino- and perfluorinated alkylsilanes: characterization and geometric definition of mammalian cell adhesion and growth. *J. Am. Chem. Soc.*, 114:8435–8442.

Stewart, P., Chiu, C., Huang, S., Muir, T., Zhao, Y., Chait, B., Mathias, P., and Nemerow, G. (1997). Cryo-EM visualization of an exposed RGD epitope on adenovirus that escapes antibody neutralization. *EMBO J.*, 16:1189–1198.

Strick, T. R., Croquette, C., and Bensimon, D. (2000). Single-molecule analysis of DNA uncoiling by a type II topoisomerase. *Blood*, 404:901–904.

Stupack, D., Li, E., Silletti, S., Kehler, J., Geahlen, R., Hahn, K., Nemerow, G., and Cheresh, D. (1999). Matrix valency regulates integrin-mediated lymphoid adhesion via Syk kinase. *J. Cell Biol.*, 144:777–788.

Suresh, S. (2006). Mechanical response of human red blood cells in health and disease: Some structure-property-function relationships. *J. Mater. Res.*, 8:1871–1877.

Tabor, D. and Winterton, R. (1969). The direct measurement of normal and retarded van der Waals forces. *Proc. R. Soc. Lond. A.*, 312:435–450.

Tan, J. L., Tien, J., Pirone, D. M., Gray, D. S., Bhadriraju, K., and Chen, C. S. (2003). Cells lying on a bed of microneedles: An approach to isolate mechanical force. *Proc. Natl. Acad. Sci. USA*, 100(4):1484–1489.

Théry, M., Pépin, A., Dressaire, E., Chen, Y., and Bornens, M. (2006). Cell distribution of stress fibres in response to the geometry of the adhesive environment. *Cell Mot. Cytosk.*, 63(6):341–355.

Thoumine, O., Kocian, P., Kottelat, A., and Meister, J.-J. (2000). Short-term binding of fibroblasts to fibronectin: optical tweezers experiments and probabilistic analysis. *Eur. Biophys. J.*, 29:398–408.

Thoumine, O., Ott, A., Cardoso, O., and Meister, J.-J. (1999). Microplates: a new tool for manipulation and mechanical perturbation of individual cells. *J. Biochem. Biophys. Meth.*, 39:47–62.

Thoumine, O., Ott, A., and Louvard, D. (1996). Critical centrifugal forces induce adhesion rupture or structural reorganization in cultured cells. *Cell Mot. Cytosk.*, 33:276–287.

Tolic-Nørrelykke, I. M., Munteanu, E.-L., Thon, G., Oddershede, L., and Berg-Sørensen, K. (2004). Anomalous diffusion in living yeast cells. *Phys. Rev. Lett.*, 93:078102.

Touhami, A., Hoffmann, B., Vasella, A., Denis, F. A., and Dufrene, Y. F. (2003). Probing specific lectin-carbohydrate interactions using atomic force microscopy imaging and force measurements. *Langmuir*, 19:1745–1751.

Valberg, P. A. and Albertini, D. F. (1985). Cytoplasmic motions, rheology, and structure probed by a novel magnetic particle method. *J. Cell Biol.*, 101:130–140.

VandeVondele, S., Vörös, J., and Hubbell, J. A. (2003). RGD-grafted poly-L-lysine-graft-(polyethylene glycol) copolymers block non-specific protein adsorption while promoting cell adhesion. *Biotech. Bioeng.*, 82(7):784.

Voet, D. and Voet, J. G. (1995). *Biochemistry.* John Wiley & Sons, Inc.

Vogel, V. and Sheetz, M. (2006). Local force and geometry sensing regulate cell functions. *Nat. Rev. Mol. Cell Biol.*, 7:265–275.

Vörös, J. (2004). The density and refractive index of adsorbing protein layers. *Biophys. J.*, 87:553–561.

Walter, N. (2005). Messung von Zelladhäsionskräften auf nanostrukturierten Oberflächen mit einer Magnetischen Pinzette. Master's thesis, Universität Heidelberg.

Walter, N., Selhuber, C., Blümmel, J., Kessler, H., and Spatz, J. P. (2006). Cellular unbinding forces of initial adhesion processes on nanopatterned surfaces probed with magnetic tweezers. *Nano Lett.*, 6(3):398–402.

Weber, P., Ohlendorf, D., Wendoloski, J., and Salemme, F. (1989). Structural origins of high-affinity biotin binding to streptavidin. *Science*, 243:85–88.

Wehrle-Haller, B. and Imhof, B. A. (2002). The inner lives of focal adhesions. *Trends Cell Biol.*, 12(8):382–389.

Weiss, M., Elsner, M., Kartberg, F., and Nilsson, T. (2004). Anomalous subdiffusion is a measure for cytoplasmic crowding in living cells. *Biophys. J.*, 87:3518–3524.

Wojcikiewicz, E., Zhang, X., and Moy, V. (2004). Force and compliance measurements on living cells using atomic force microscopy (AFM). *Biol. Proced. Online*, 6:1–9.

Wottawah, F., Schinkinger, S., Lincoln, B., Ebert, S., Müller, K., Sauer, F., Travis, K., and Guck, J. (2005). Characterizing single suspended cells by optorheology. *Acta Biomaterialia*, 1:263–271.

Xing, B., Jedsdayanmata, A., and Lam, S. C.-T. (2001). Localization of an integrin binding site to the C terminus of talin. *J. Biol. Chem.*, 276(48):44373–44378.

Xiong, J.-P., Stehle, T., Diefenbach, B., Zhang, R., Dunker, R., Scott, D. L., Joachimiak, A., Goodman, S. L., and Arnaout, M. A. (2001). Crystal structure of the extracellular segment of integrin $\alpha_v\beta_3$. *Science*, 294:339–345.

Young, R., Ward, J., and Scire, F. (1972). The topografiner: An instrument for measuring surface microtopography. *Rev. Sci. Instrum.*, 43(7):999–1011.

Zaidel-Bar, R., Ballestrem, C., Kam, Z., and Geiger, B. (2003). Early molecular events in the assembly of matrix adhesions at the leading edge of migrating cells. *J. Cell Sci.*, 116:4605–4613.

Zaidel-Bar, R., Cohen, M., Addadi, L., and Geiger, B. (2004). Hierarchical assembly of cell-matrix adhesion complexes. *Biochem. Soc. Trans.*, 32:416–420.

Zamir, E. and Geiger, B. (2001a). Components of cell-matrix adhesions. *J. Cell Sci.*, 114:3577–3579.

Zamir, E. and Geiger, B. (2001b). Molecular complexity and dynamics of cell-matrix adhesions. *J. Cell Sci.*, 114:3583–3590.

Zamir, E., Katz, M., Posen, Y., Erez, N., Yamada, K. M., Katz, B. Z., Lin, S., Bershadsky, Kam, Z., and Geiger, B. (2000). Dynamics and segregation of cell-matrix adhesions in cultured fibroblasts. *Nat. Cell Biol.*, 2:191–196.

Zimmerman, E., Geiger, B., and Addadi, L. (2002). Initial stages of cell-matrix adhesion can be mediated and modulated by cell-surface hyaluronan. *Biophys. J.*, 82:1848–1857.

Acknowledgements

When I think back to the first stages of this work, I remember the words of a friend, an astronomer: *"Twenty years ago people called me crazy that I want to study the forces between galaxies. I now call you crazy that you want to measure forces between cells!"* This was some months after I had started my PhD work, and in the beginning everything really looked like he was right. In the meantime a lot has changed, we succeeded in measuring even more than originally planned and this would not have been possible without many helping hands.

First, I want to thank Joachim Spatz for the possibility to work on this interesting and really fascinating project, for the opportunity to realise my own ideas and for the support I got during the last years. I am grateful to Prof. Horner, for agreeing to be a referee of this theses and for the nice discussions we had during the last years, where he was always asking the right questions. I also thank Ulrich Schwarz for the many new inputs he gave to my work. His ideas not only significantly directed the ways some projects took, I definitely learnt a lot from him.

For not only supporting me financially, but also personally, I thank the Boehringer Ingelheim Fonds (B.I.F.) and their staff, who have built up a stimulating and encouraging atmosphere among the scholarship holders.

For teaching me the first steps in biophysics I want to thank Erich Sackmann and especially Stefanie Gönnenwein. Stefanie introduced me to RICM and magnetic tweezers, and the weeks I spent at the E22 were the perfect start of my PhD time. Equally I want to thank Ana Smith for our discussions on adhesion from the thermodynamical perspective.

Furthermore I want to thank Martin Benoit for the possibility to share our experiences on force measurements, Horst Kessler and his group for providing the c(-RGDfK-) peptide and Janos Vörös for his advice in surface chemistry.

For spending a lot of time with introducing me into his adhesion cluster theory and relating the experimental data to his model, I thank Thorsten Erdmann.

In the Spatz group, there are some people I want to point out because I closely worked together with them during the past years. First of all, I thank my two diploma students, Nadine Walter and Irina Slizskaia for the great time we spent together. I also thank my HiWis and project students, Fabian Czerwinski, Christian Hökel, Nora Rieber and Mirjam Geibel for their contributions to my work. A big thanks goes to Jennifer Curtis and Ralf Richter for great discussions and their experienced support for writing publications! Finally I also want to thank Ilia Louban, who will continue the force experiments and I think the project is in good hands. Nevertheless, I would like to thank our technicians in

Stuttgart and Heidelberg and our secretary Frau Schönig for all their support that made life easier.

In particular I want to thank those people, who helped with proof-reading my thesis or parts of it, Ingmar, Nadine, Iain, Ralf, Patrick, Ada, Thorsten, Daniel, Heike and Krysia.

In the same way I thank the other people from the Spatz group for the past years!

However, I also have to thank some people from my non-academic life.

Thank you, Dominikus, Dani, Babs, Juliet and Ronny for the great time we spent together during our years in Heidelberg.

Above all I would like to thank my family for supporting me whenever possible.

Last but not least, I thank Ingmar for his never ending patience and support and for sharing life with me.

Appendix

Abbreviations

AFM	Atomic Force Microscopy
conA	Concanavalin A
DMEM	Dulbecco's Modified Eagle's Medium; cell medium
ECM	Extracellular Matrix
FBS	Fetal bovine serum; contains growth factors
FN	Fibronectin; protein in the ECM where integrins bind to
JKR model	Johnson Kendall Roberts model
Pax	Paxillin, focal contact component
PBS	phosphate buffered saline; in this thesis 1xPBS (Gibco, Germany) is used
PEG	Polyethyleneglycol
PLL	Poly-L-lysine
PLL-g-PEG	PLL-graft-PEG; for passivating surfaces, see section 3.2.2
REF 52 WT	Rat embryonic fibroblasts, wild type
REF YFP Pax	REF 52 WT cells with YFP labelled paxillin
RGD	R=arginine (arg), G=glycine (gly), D=asparagine (asp), Integrin binding sequence in fibronectin
RICM	Reflection Interference Contrast Microscopy
SEM	Scanning Electron Microscope
TIRF	Total Internal Reflection Fluorescence Microscopy
YFP	Yellow fluorescent protein

Symbols

d	Distance of integrin binding site distance on nanopatterned substrates
k	Force constant of a cantilever
K	Bulk modulus, i.e. $4E/(3(1-\sigma^2))$
E	Young's modulus
σ	Poisson ratio
r	Loading rate, i.e. temporal increase of bond loading: $r := \partial F/\partial t$
k_{on}	Rebinding rate
k_0	Dissociation rate of a bond at zero force
F_0	$F_0 = k_B T/x_B$, internal force scale of a bond

Materials and Methods

Homogeneously Functionalised Substrates

Fibronectin-coated glass slides

Fibronectin (F1141, Sigma, Germany) was covalently bound to glass slides following the protocol given by Katz et al. (2000). Clean and oxygen plasma activated surfaces (10 min, 0.4 mbar O_2, 150 W; Te-Pla 100-E, Germany) are incubated in a 50 μg/mol solution of poly-L-lysine (Sigma, Germany) in PBS (Gibco, Germany) for 20 min. Afterwards they are washed with MilliQ-water and a 1% aqueous solution of glutaraldehyde is added for 15 min. The samples are once more washed with MilliQ-water and incubated in a 10 μg/ml solution of fibronectin (Sigma, Germany) in 1xPBS for at least 30 minutes. Prior to usage in cell culture the samples were washed several times with sterile PBS.

c(-RGDfK-) coated substrates

The thiolated c(-RGDfK-) peptide was covalently bound to gold coated glass surfaces. The gold coating consisted of a 5 nm thick layer of titanium and a 50 nm thick layer of gold on top. To bind the c(-RGDfK-) thiols, the substrates were cleaned with an oxygen plasma treatment (10 min, 0.4 mbar O_2, 150 W; Te-Pla 100-E, Germany) and then immersed into a 25 μmol aqueous solution of the c(-RGDfK-) peptide for at least 4 hours. Prior to usage, they were washed with MilliQ-water.

Preparation of Nanopatterns

Gold Nanopatterns

Nanopatterned substrates are prepared according to the protocol published in Arnold et al. (2004). The preparation of the nanopatterned substrates comprises the following steps: First, the micelle solution is prepared by dissolving the diblock-copolymer (Polymer Source, Montreal, Canada) into toluene (Merck, Germany) and the gold salt (Tetrachlorogold(III)acid trihydrate; Aldrich, Germany) is added in the concentrations given in table A.1. Then, piranha solution (H_2O_2:H_2SO_4=1:3; 30-60 min) cleaned glass slides are dipped into the micelle solution at a speed of 12 mm/min. By varying this dipping speed the projected distance of the micelles on the glass slides can be varied (Jakubick, 2005). The polymer shell of the micelles is removed with a hydrogen plasma treatment (45 min, 0.4 mbar, 150 W; Te-Pla 100-E, Germany) and during this treatment the gold salt is reduced to elemental gold, leaving nanometre sized gold dots on the surface.

PS-b-P2VP polymer	Polymer concentration	n($HAuCl_4$)/2VP	Gold dot distance
PS(245)-b-P2VP(223)	5 mg/ml	0.2	28 ± 7
PS(501)-b-P2VP(323)	5 mg/ml	0.5	50 ± 11
PS(989)-b-P2VP(385)	5 mg/ml	0.2	103 ± 15
PS(2076)-b-P2VP(571)	2 mg/ml	0.2	90 ± 15
PS(1780)-b-P2VP(523)	2 mg/ml	0.2	100 ± 10

Table A.1: Polymers and concentrations used for the preparation of micellar solutions. The loading parameter for adding the gold ions into the micellar core is n($HAuCl_4$)/2VP and describes the number of $HAuCl_4$ molecules per 2VP unit of the block copolymer. Possible variations in the gold dot distance between several lots can arise from variations in polymer concentration as a result of toluene evaporation. Therefore the gold dot distance of each lot was determined with SEM.

Passivation Strategies

Passivation with mPEG2000-Urea. The area between the gold particles is covalently passivated with a thin layer of mPEG2000-urea by immersing the hydrogen plasma activated, nanopatterned glass surfaces (5 min, 0.4 mbar H_2, 150 W; Te-Pla 100-E, Germany) in a 1 mmol solution of the linear polyethylene glycol, mPEG2000-urea, (CH_3-(O-CH_2-CH_2)$_{43}$-NH-CO-NH-CH_2-CH_2-CH_2-Si(OEt)$_3$) in dry toluene (p.A. from Merck, Germany) with 0.05% triethylamine (Sigma, Germany) at 80°C under nitrogen atmosphere for at least 16 hours. To remove non-covalently bound PEG molecules, the substrates are rinsed extensively with ethyl acetate and methanol (all p.a. from Aldrich, Germany) before they are blown dry.

Passivation with PLL-g-PEG. Nanopatterned glass substrates are activated with oxygen plasma (10 min, 0.4 mbar O_2, 150 W; Te-Pla 100-E, Germany) before being immersed into an aqueous solution of PLL20[kDa]-g[3.5]-PEG2[kDa] (SurfaceSolutions, Switzerland) for 40 minutes. The solution contains 0.1 mg/ml PLL-g-PEG in a HEPES buffer (2.383 g HEPES in 1 liter of H_2O and 0.688 ml of 6M NaOH; the pH was adjusted to 7.4). After the incubation the samples are rinsed with water and blown dry.

Gold Dot Functionalisation

c(-RGDfK-) functionalisation. The gold dots are biofunctionalised after passivation by an incubation with a 25 μmol aqueous solution of the c(-RGDfK-) thiol(= c[RGDfK(Ahx-Mpa)]) for 4 hours. Subsequently, the samples are rinsed with MilliQ-water and shaken for 24 hours to remove the non-covalently bound c(-RGDfK-) thiols.

Streptavidin functionalisation. The mPEG2000-urea passivated substrates are incubated in a 1 mg/ml solution of mercaptoundecanonic acid (Sigma-Aldrich) in ethanol p.a.(Riedel-de-Häen, Germany) at room temperature overnight. The carboxy group of the mercaptoundecanoic acid is activated by incubating the substrates first into an aqueous solution of 0.2 M N-(3- dimethyl amino propyl)-3-ethyl carbodiimide hydrochloride (EDC; Aldrich, Germany) and 0.05 M N-hydroxysuccinimide (NHS; Fluka, Germany) for 5-7 minutes. The final coupling of the streptavidin (from streptomyces avidinii; S4762, Sigma, Germany) is performed by wetting the substrates with a 10μg/ml solution of the protein in 1xPBS for 4 hours. Non-covalently bound streptavidin is removed by shaking the samples overnight in PBS.

Cantilever Functionalisation

Cantilever functionalisation for initial adhesion experiments

AFM cantilevers for initial adhesion experiments were delivered from Veeco (NP-020, MLCT-AU). The procedure to functionalise the functionalise cantilevers with concanavalin A (conA) follows the method presented in Wojcikiewicz et al. (2004). Firstly, the cantilevers are soaked in acetone for 5 minutes before they are activated with an oxygen plasma (1 min, 0.4 mbar O_2, 150 W; Te-Pla 100-E, Germany). Secondly, they are incubated in biotin-BSA (0.5 mg/ml in 0.1 M sodium bicarbonate, pH 8.6; Sigma, Germany) overnight at 37°C in a parafilm wrapped petri dish. To remove unbound protein, the cantilevers are washed extensively with PBS. Biotin-BSA functionalised cantilevers can be stored in PBS at 4°C for up to a week. For further functionalisation, the cantilevers are incubated into a droplet of streptavidin (0.5 mg/ml in 1xPBS; S4762, Sigma, Germany) for 10 minutes at room temperature. Prior to the last preparation step, the cantilevers are washed with PBS. Then they are incubated in biotin-conA (0.2 mg/ml in 1xPBS, Sigma, Germany) for 10 minutes at room temperature. At last, the conA functionalised cantilevers are once more washed with PBS.

Cantilever functionalisation for long-term adhesion experiments

Tipless cantilevers for long-term adhesion experiments are delivered from Mikromasch, Estonia (NSC12). The cantilevers are cleaned with a piranha solution (H_2O_2:H_2SO_4=1:3) for 5 min and activated with oxygen plasma (1 min, 0.4 mbar O_2, 150 W; Te-Pla 100-E, Germany). Subsequently they are incubated in a solution containing 94% acidic methanol (1 mM acetic acid in methanol), 5% MilliQ-water and 1% (3-aminopropyl)-triethoxysilane at room temperature for 30 minutes (Stenger et al., 1992). They are extensively rinsed with methanol and dried at 60°C for 20 minutes before they are incubated in an 1% aqueous solution of glutaraldehyde. After this step the cantilevers are extensively rinsed in water before they are immersed into a PBS solution of 10 μg/ml fibronectin (Sigma, Germany) for at least 30 minutes.

Cell Culture

All steps including work in the cell culture are performed in a sterile hood and involve sterile materials. In this stuy, rat embryonic fibroblasts (REF 52 WT; REF 52 YFP PAX) are cultured in DMEM (Invitrogen, Germany) supplemented with 10% FBS and 2% L-Glutamine. The medium is exchanged every second day. When the cells have reached confluence, they are detached from the cell culture dish. For this, they are washed twice with 5 ml sterile PBS and then incubated in 3-4 ml trypsin-EDTA for 4-5 minutes. Upon cell detachment, 5 ml DMEM is added. The mixture is then centrifugated for 3-5 minutes at 1000 rpm. Afterwards the supernatant of this solution is removed and the pellet is resuspended in the medium and cells are either used to provide new culture flasks or to perform experiments.

Ich erkläre hiermit, dass ich die vorgelegte Dissertation selbst verfasst und mich keiner anderen als der von mir ausdrücklich bezeichneten Quellen und Hilfen bedient habe.

Heidelberg, den 13. Oktober 2006

. . . .

Christine Selhuber